UNIVERSIDAD DE MÁLAGA
ESCUELA TÉCNICA SUPERIOR DE INGENIERÍA DE TELECOMUNICACIÓN
PROGRAMA DE DOCTORADO EN INGENIERÍA DE TELECOMUNICACIÓN

TESIS POR COMPENDIO DE PUBLICACIONES

ADVANCED PERIODIC TOPOLOGIES FOR NEXT-GENERATION SILICON PHOTONICS

AUTOR

Carlos Pérez Armenta

DIRECTORES

J. Gonzalo Wangüemert Pérez

Alejandro Ortega Moñux

15 de diciembre de 2024

AUTOR: Carlos Pérez Armenta

https://orcid.org/0000-0003-1093-5056

EDITA: Publicaciones y Divulgación Científica. Universidad de Málaga

DECLARACIÓN DE AUTORÍA Y ORIGINALIDAD DE LA TESIS PRESENTADA PARA OBTENER EL TÍTULO DE DOCTOR

D./Dña CARLOS PÉREZ ARMENTA
Estudiante del programa de doctorado EN INGENIERÍA DE TELECOMUNICACIÓN de la Universidad de Málaga, autor/a de la tesis, presentada para la obtención del título de doctor por la Universidad de Málaga, titulada: ADVANCED PERIODIC TOPOLOGIES FOR NEXT-GENERATION SILICON PHOTONICS

Realizada bajo la tutorización de J. GONZALO WANGÜEMERT PÉREZ y dirección de J. GONZALO WANGÜEMERT PÉREZ Y ALEJANDRO ORTEGA MOÑUX (si tuviera varios directores deberá hacer constar el nombre de todos)

DECLARO QUE:

La tesis presentada es una obra original que no infringe los derechos de propiedad intelectual ni los derechos de propiedad industrial u otros, conforme al ordenamiento jurídico vigente (Real Decreto Legislativo 1/1996, de 12 de abril, por el que se aprueba el texto refundido de la Ley de Propiedad Intelectual, regularizando, aclarando y armonizando las disposiciones legales vigentes sobre la materia), modificado por la Ley 2/2019, de 1 de marzo.

Igualmente asumo, ante la Universidad de Málaga y ante cualquier otra instancia, la responsabilidad que pudiera derivarse en caso de plagio de contenidos en la tesis presentada, conforme al ordenamiento jurídico vigente.

En Málaga, a 25 de OCTUBRE de 2024

Fdo.: CARLOS PÉREZ ARMENTA Doctorando/a	Fdo.: J. GONZALO WANGÜEMERT PÉREZ Tutor/a
Fdo.: J. GONZALO WANGÜEMERT PÉREZ Y ALEJANDRO ORTEGA MOÑUX Director/es de tesis	

Edificio Pabellón de Gobierno. Campus El Ejido. 29071
Tel.: 952 13 10 28 / 952 13 14 61 / 952 13 71 10
E-mail: doctorado@uma.es

Yo, **J. Gonzalo Wangüemert Pérez**, con DNI , tutor y director de la tesis titulada "*Advanced Periodic Topologies for Next-Generation Silicon Photonics",* realizada por el estudiante del programa de doctorado en Ingeniería de Telecomunicación **Carlos Pérez Armenta**, con DNI , autorizo la lectura de dicha tesis doctoral.

De igual forma, confirmo que las publicaciones que avalan esta tesis, las cuales se pueden consultar en el capítulo 2 de esta memoria, no han sido utilizadas en tesis anteriores.

Fdo. J. Gonzalo Wangüemert Pérez
Director y tutor de tesis

Yo, **Alejandro Ortega Moñux**, con DNI , director de la tesis titulada "*Advanced Periodic Topologies for Next-Generation Silicon Photonics",* realizada por el estudiante del programa de doctorado en Ingeniería de Telecomunicación **Carlos Pérez Armenta**, con DNI , autorizo la lectura de dicha tesis doctoral.

De igual forma, confirmo que las publicaciones que avalan esta tesis, las cuales se pueden consultar en el capítulo 2 de esta memoria, no han sido utilizadas en tesis anteriores.

Fdo. Alejandro Ortega Moñux
Director de tesis

Edificio Pabellón de Gobierno. Campus El Ejido. 29071
Tel.: 952 13 10 28 / 952 13 14 61 / 952 13 71 10
E-mail: doctorado@uma.es

Acknowledgements

It has been seven years since I first joined University of Málaga's Photonics & RF Research Lab back in 2017, during my last year of undergraduate studies. After defending my BSc Thesis supervised by Prof. Gonzalo Wangüemert, I continued to contribute to some research tasks under his guidance while pursuing my MSc studies, eventually defending my MSc thesis in 2020. After these wonderful 3 years, I had no hesitation in continuing with my PhD studies in integrated photonics in the group. This journey has not only provided me invaluable academic training but has also been a period of significant personal growth. These pages are meant to thank all the people who have been part of it.

By the end of the second year of my PhD, I had the opportunity to do a research visit in Ottawa at the Advanced Electronics and Photonics Research Centre of the National Research Council of Canada. I want to thank Dr. Pavel Cheben and Dr. Jens Schmid for their supervision during those four months and their advice in the work endorsing this thesis. On a more personal note, I specially thank Dr. Pavel Cheben for his hospitality and making me feel like at home.

Apart from all the theoretical knowledge, since I became a PhD student I have received training in experimental characterization of photonic integrated circuits. Many thanks to Prof. Pepe Oliva for his patience and training in optical measurements and also to Shurui Wang and Martin Vachon, who taught me and assisted me during the characterization of the tunable Bragg filters.

I would like to express my gratitude to Prof. Winnie Ye, Prof. Iñigo Molina, Dr. Pavel Cheben and Dr. Jens Schmid for letting me be part of the research collaboration that resulted in the demonstration of the tunable Bragg filters carried out in this thesis. Special thanks to Kevan MacKay for his early work and layout generation, and to my colleage and friend Dr. Abdelfettah Hadij El Houati for leading the design tasks which I had the pleasure to assist.

In the last year, Prof. Robert Halir offered me to delve into a new research line for the group: photonic inverse design. I had to learn about optimization, put my programming skills to test, integrate our simulation scripts in a supercomputer and teach others to do

so. I am very thankful to him for the opportunity and his extremely efficient mentoring. In addition, I want to express my gratitude to another colleage and friend, Alejandro Sánchez Sánchez, for characterizing the designs resulting from our work in this project. We also acknowlege and thank the resources, technical experience and assitance provided by the centre of Supercomputing and Bioinnovation (SCBI) of the University of Málaga.

I also want to thank to all the professors, colleagues and students from the research group for their support, company and because I have learned from every one of them to some degree. Special mention to Alejandro Fernández for his help with the establishment of code maintaining systems, simulation scripts and our layout package; José Manuel Luque, who I have it clear that have been a model and mentor during my PhD; Prof. Iñigo Molina, as a head of the group and for his guidance in my teaching assistance duties along with Prof. Javier Mata. Lastly, this thesis could not have been possible without my supervisors Profs. Gonzalo Wangüemert and Alejandro Ortega for whom my words cannot express enough gratitude. I am very thankful to them for their invaluable academic and life lessons they have shared with me.

By the end of my PhD, I have been given the tremendous opportunity to join AG-Photonics, one of the spin-off companies born from the research group. I would like to extend my thanks to the founder team for considering me for being part of the company and giving me the chance of growing professionally in this new stage.

Por último y no menos importante, estas palabras de agradecimiento van dirigidas a mis amigos por su apoyo y compañía durante todos estos años y a mi familia: a mis padres, Carlos y Mª Gracia, mi hermano Víctor y Luna. Sin ellos nada de esto sería posible.

Funding

This Thesis has been made possible thanks to the support and funding from the following programs, projects, and institutions:

- **Beca de Formación de Profesorado Universitario (FPU)**

  Ministerio de Ciencia, Innovación y Universidades

  Grant no.: FPU19/02408

- **Convocatoria de Proyectos de I+D+i (Generación de conocimiento y retos de investigación))**

  Ministerio de Economía y Competitividad

  Title: Materiales y dispositivos fotónicos sublongitud de onda para aplicaciones del mundo real (SAMARA)

  Grant no.: PID2019-106747RB-I00

- **Proyectos de investigación orientados a los retos de la sociedad andaluza**

  Junta de Andalucía (Fondos FEDER)

  Title: Filtros Ópticos Integrados para Comunicaciones y Sensado

  Grant no.: P18-RT-1453

- **Proyectos de investigación orientados a los retos de la sociedad andaluza**

  Junta de Andalucía (Fondos FEDER)

  Title: Fotónica del silicio para medioambiente y salud (FLAMES)

  Grant no.: P18-RT-793

- **Proyectos I+D+I en el marco del Programa Operativo FEDER 2014-2020**

  Junta de Andalucía (Fondos FEDER)

  Title: Fotónica integrada para escaneo de haces ópticos en aplicaciones LIDAR

  Grant no.: UMA20-FDERJA-158

Compendium of publications

During his PhD studies, the candidate has been the first author of four publications in JCR-indexed journals with a combined ANECA score exceeding 1. Additionally, he has participated in seven peer-reviewed conferences of national and international scope as first author. As per the doctoral studies regulations at the University of Málaga, it is proposed that these publications support the submission of this Thesis as a compendium of publications.

Publications endorsing the thesis and quality metrics

1. C. Pérez-Armenta, A. Ortega-Moñux, J. Čtyroký, P. Cheben, J. H. Schmid, R. Halir, Í. Molina-Fernández, and J. G. Wangüemert-Pérez, "Narrowband bragg filters based on subwavelength grating waveguides for silicon photonic sensing," *Opt. Express*, vol. 28, no. 25, pp. 37 971–37 985, Dec. 2020. DOI: 10.1364/OE.404364.
    - Journal Impact Factor (JIF) (JCR 2020): 3.894
    - Rank by JIF in the Optics category (JCR 2020): 20/99 (Q1)
    - Peer-reviewed article
    - Current citations (Google Scholar): 26
2. C. Pérez-Armenta, A. Ortega-Moñux, J. M. Luque-González, R. Halir, P. J. Reyes-Iglesias, J. Schmid, P. Cheben, Í. Molina-Fernández, and J. G. Wangüemert-Pérez, "Polarization-independent multimode interference coupler with anisotropy-engineered bricked metamaterial," *Photon. Res.*, vol. 10, no. 4, A57–A65, Apr. 2022. DOI: 10.1364/PRJ.446932.
    - Journal Impact Factor (JIF) (JCR 2022): 7.6
    - Rank by JIF in the Optics category (JCR 2022): 11/100 (Q1)
    - Peer-reviewed article
    - Current citations (Google Scholar): 16
3. C. Pérez-Armenta, A. Ortega-Moñux, J. M. Luque-González, R. Halir, J. Schmid, P.

Cheben, I. Molina-Fernández, and J. G. Wangüemert-Pérez, "Polarization insensitive metamaterial engineered multimode interference coupler in a 220 nm silicon-on-insulator platform," *Optics & Laser Technology*, vol. 164, p. 109 493, Apr. 2023. DOI: 10.1016/j.optlastec.2023.109493.

- Journal Impact Factor (JIF) (JCR 2023): 4.6
- Rank by JIF in the Optics category (JCR 2023): 21/119 (Q1)
- Peer-reviewed article
- Current citations (Google Scholar): 6

4. C. Pérez-Armenta, K. K. MacKay, A. Hadij-ElHouati, A. Ortega-Moñux, I. Molina-Fernández, J. G. Wangüemert-Pérez, J. H. Schmid, P. Cheben, and W. N. Ye, "Thermally induced sideband generation in silicon-on-insulator cladding modulated bragg notch filters," *Opt. Express*, vol. 31, no. 13, pp. 22 225–22 232, Jun. 2023. DOI: 10.1364/OE.488108.

- Journal Impact Factor (JIF) (JCR 2023): 3.2
- Rank by JIF in the Optics category (JCR 2023): 36/119 (Q2)
- Peer-reviewed article
- Current citations (Google Scholar): 2

CONTENTS

List of Figures

List of Tables

Acronyms

BOX Buried oxide

CMA-ES Covariance Matrix Adaptation Evolution Strategy

CMT Coupled Mode Theory

DUV Deep Ultra-Violet

EBL Electron Beam Lithography

FOM Figure of Merit

FSR Free Spectral Range

GA Genetic Algorithm

iLoD intrinsic LoD

IPh Integrated Photonics

LoD Limit of Detection

MMI Multimode Interference

MZI Mach-Zehnder Interferometer

PSO Particle Swarm Optimization

RIU Refractive Index Unit

SiPh Silicon Photonics

SOI Silicon On Insulator

SSC Spot-Size Converter

SWG Subwavelength Grating

TE Transversal Electric

TM Transversal Magnetic

WDM Wavelength Division Multiplexing

Chapter 1

INTRODUCTION

In 1969, Stewart E. Miller proposed a "miniature form of a laser beam circuitry" [1]. In his work, Miller studied the feasibility of patterning, with the at that time evolving photolitography techniques, light waveguides and components in a common substrate. This seminal work laid the groundwork for Integrated Photonics (IPh).

Five decades later, IPh is now a well-stablished technology field dedicated to the generation, manipulation and detection of light within integrated circuits. IPh finds applications mainly in optical communications [2, 3] and also in other emerging areas such as biosensing [4], quantum processing and quantum communications [5] and LiDAR [6], to name a few. In contrast to discrete systems, IPh offers optical functionalities in compact packaging sizes, exhibiting reduced susceptibility to mechanical instability and lower costs. Currently, various material platforms are used for on-chip integration including lithium niobate [7], glass [8] or III-V semiconductors like gallium arsenide, indium phosphide or indium gallium arsenide [9]; but silicon-based photonics has gained great interest in the last decades in both the academic community and the private sector.

The escalating volume of traffic has intensificated the need of photonic transceivers in telecommunication networks. Concurrently, the rising demand of streaming and cloud services, coupled with the adoption of work from home policies and the ongoing proliferation of artificial intelligence, have boosted the necessity for optical links within data centers. These demands combined with the compatibility with already developed manufacturing processes for CMOS microelectronics have driven continuous growth in the Silicon Photonics (SiPh) market over the past years, as shown in Fig. 1.1 [10]. Evidencing this trend, major semiconductor manufacturers such as GlobalFoundries or TSMC have announced new SiPh solutions in the last year and colaborations with industry leaders like Broadcom, Cisco Systems or NVIDIA [11, 12].

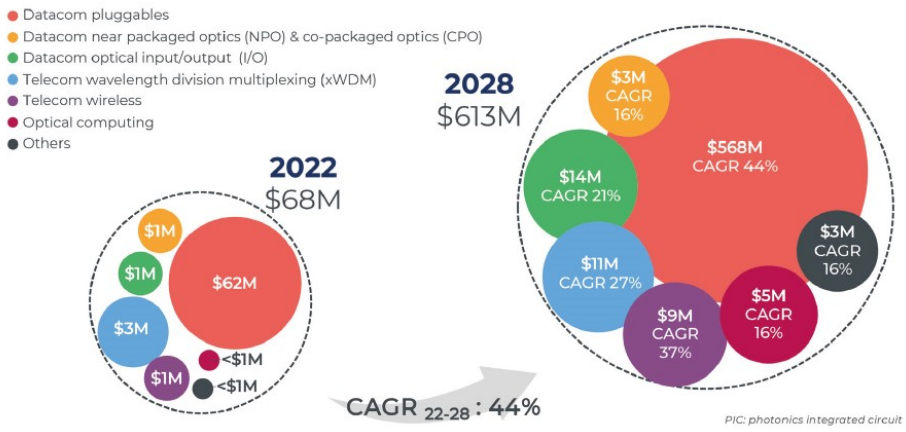

Figure 1.1 Silicon photonic integrated circuit dies revenue growth forecast by application in 2022–2028. The silicon photonic market value is expected to grow at a 44% Compound Annual Growth Rate (CAGR). Source: [10] © Yole Intelligence 2023.

SiPh chips primarily consist of silicon and silicon dioxide, with the potential inclusion of other materials such as silicon nitride or germanium [13]. Several kind of optical components can be integrated in a SiPh chip, from passives devices such as filters, power splitters/combiners or (de)multiplexers to active devices like high speed modulators or broadband photodiodes [14] thanks to semiconductor doping and the integration of metallic interconnection layers. Additionally, electronic-photonic co-integration is possible, enabling the inclusion of the control logic and the optical devices in the same chip [15].

This thesis focuses on the Silicon-on-Insulator (SOI) platform, illustrated in Fig. 1.2. A SOI chip layer structure comprises a Si substrate of hundreds of microns, onto which a $2-3\,\mu$m-thick SiO_2 layer, also known as buried oxide (BOX), is grown, followed by the deposition of a thin (few hundreds of nm) Si layer. Devices are then patterned using techniques such as electron beam lithography (EBL) or deep ultraviolet lithography (DUV) in combination with etching processes like Reactive-ion Etching. Minimum feature sizes are usually of the order of 60 nm in the case of EBL [16] and 100–200 nm in the case of DUV [17]. Optionally, an additional layer of SiO_2 is deposited on top of the chip. Besides its direct compatibility with CMOS fabrication processes, SOI serves as an excelent alternative for telecom and datacom IPh due to the optical transparency of Si and SiO_2 at optical communications wavelengths ($1.26-1.65\,\mu$m).

SOI high refractive index contrast facilitates stronger light confinement, thereby enabling the design of compact devices with low bend radii. Fig. 1.3(a) shows the refractive indices of Si and SiO_2refractive indices as a function of wavelength. For example, for $\lambda = 1550\,$nm, $n_{Si} = 3.476$ and $n_{SiO_2} = 1.444$. Fig. 1.3(b) shows the effective indices of the fundamental Tranverse Electric (TE) and Transverse Magnetic

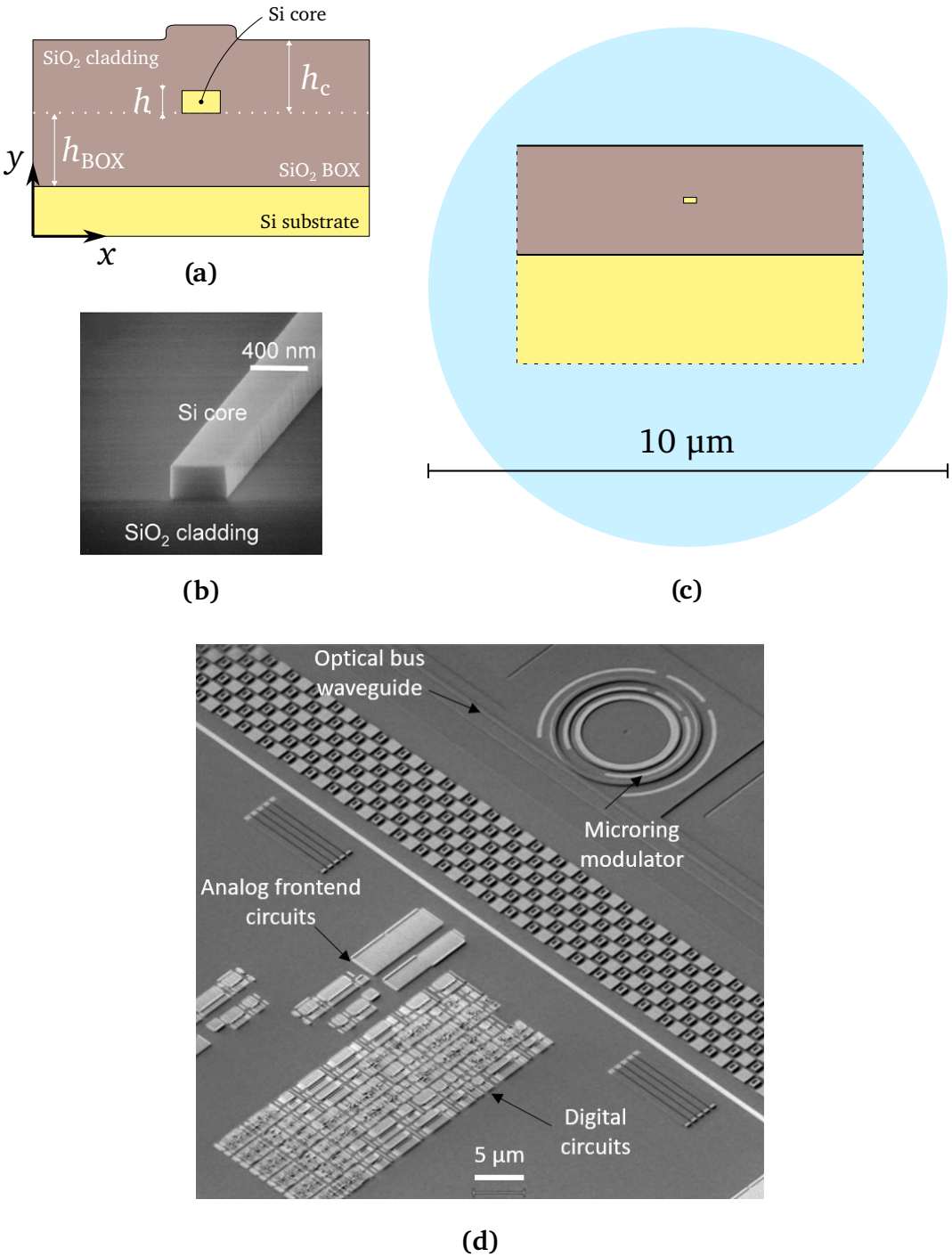

Figure 1.2 The Silicon on Insulator (SOI) platform. (a) Schematic representation of a silicon wire cross-section. Typical dimensions are $h \sim 220-300\,\text{nm}$ and $h_{\text{BOX}}, h_{\text{c}} \sim 2-3\,\mu\text{m}$. (b) Scanning electron microscope (SEM) image of a 400 nm-wide Si wire, reprinted from [18] © 2005 IEEE. (c) Scaled comparison of a Si wire and a typical mode field diameter of a single-mode fiber for near infrared applications. (d) SEM image of co-integrated photonic and electronic circuits. Reprinted from [15] with permission.

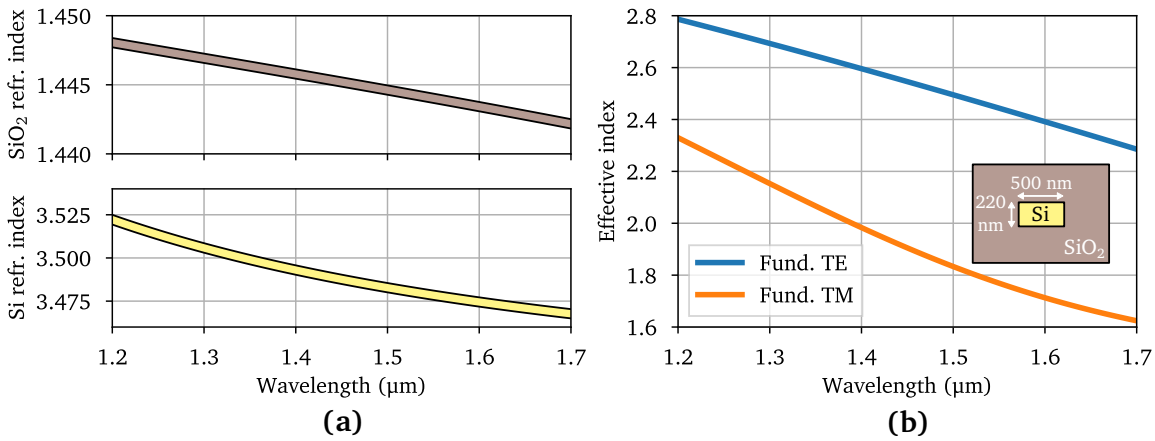

Figure 1.3 (a) Refractive indices of Si and SiO_2 vs the wavelength. (b) Effective indices of the fundamental TE and TM modes of a silicon wire with a 500 nm×220 nm cross-section.

(TM) modes of a commonly used silicon waveguide: a 500 nm-wide and 220 nm-thick silicon wire. In addition, the thermo-optic coefficient of Si ($dn_{Si}/dT \approx 1.9 \cdot 10^{-4}$ RIU/K, where RIU denotes Refractive Index Unit) allows for tunability in SOI waveguides and thus the design of reconfigurable components. Yet, SOI photonic circuits are constrained to these two materials and their refractive indices cannot be easily modified, limiting the design space of the photonic engineer. For example, the performance of some devices like multimode interference couplers rely on the refractive index contrast between the multimode waveguide core and the surrounding medium. Periodic structures thus play a fundamental role in refractive index engineering, enabling capabilities that conventional waveguides cannot provide.

1.1 Periodic structures for SOI integrated photonics

Periodic structures offer a way of expanding the design possibilities of SOI-based photonics. Fig. 1.4(a) shows an example of periodic waveguide, formed by a periodic arrangement of silicon strips, with a period $\Lambda = a + b$ and duty-cycle $DC = a/\Lambda$. Depending on wavelength-period ratio λ/Λ, three operation regimes are distinguished giving a different response in the waveguide effective index: radiation, Bragg and subwavelength. Fig. 1.4(b, c) illustrates these operation zones.

Radiation ($n_{eff} = m(\lambda/\Lambda) + n_s \sin\theta, \quad m \in \mathbb{Z}$)

In this operation mode, light is diffracted or radiated out of the waveguide to the surrounding medium n_s (air or SiO_2in SOI platforms) with an angle θ. Although this operation mode is not exploited in this thesis, it founds applications in fiber-chip surface coupling [21] and optical antennas [22]. By adjusting the geometry of the periodic

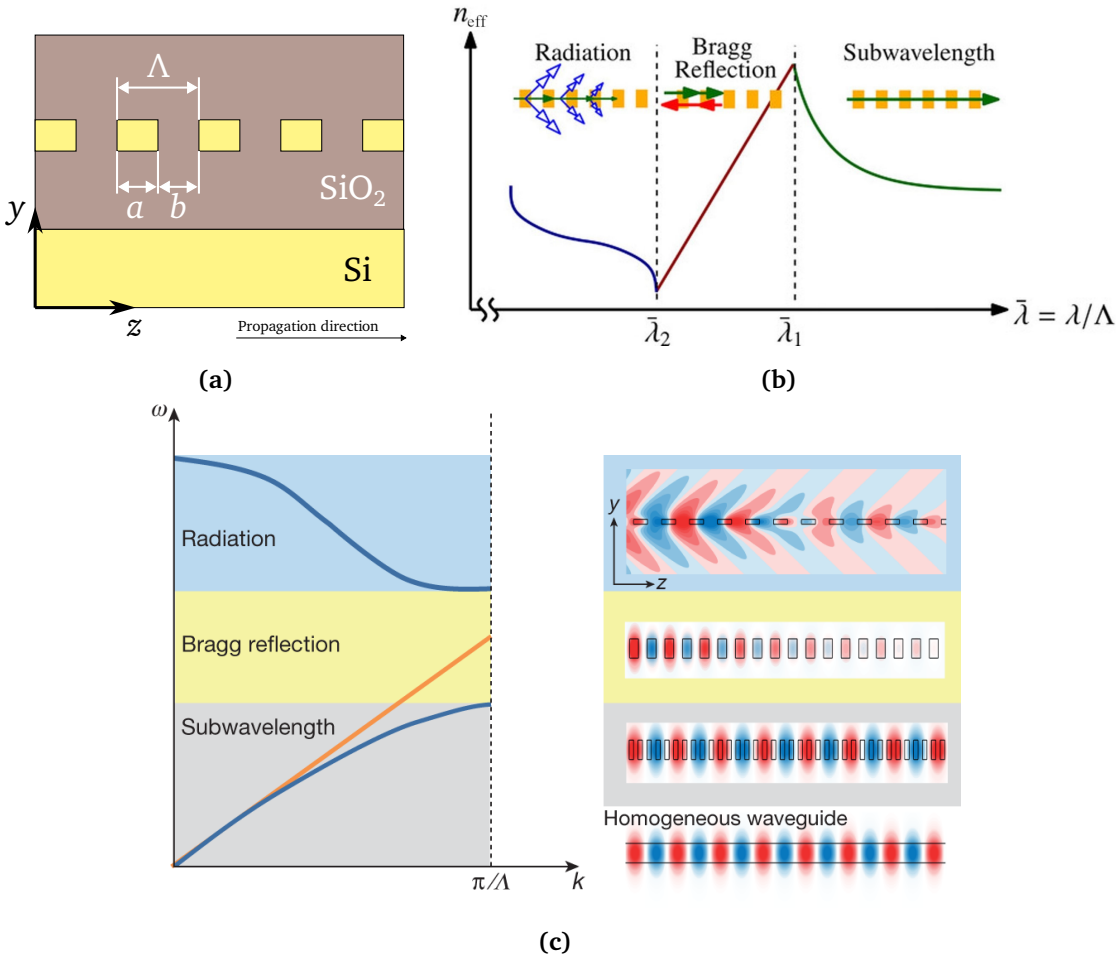

Figure 1.4 (a) Example of periodic waveguide. Depending on the wavelength to period λ/Λ ratio, three operating regimes are distinguished: radiation, Bragg and subwavelength. (b) Effective index dependence with the wavelength-pitch ratio λ/Λ. Reprinted from [19] under the terms of the CC-BY-NC-ND 3.0 license. (c) Dispersion diagram $k(\omega) = \frac{\omega}{c} n_{\text{eff}}(\omega)$ and electromagnetic field of each zone compared to an equivalent homogeneous waveguide. Higher-order Bragg and radiation zones are not shown. Reprinted from [20] with permission.

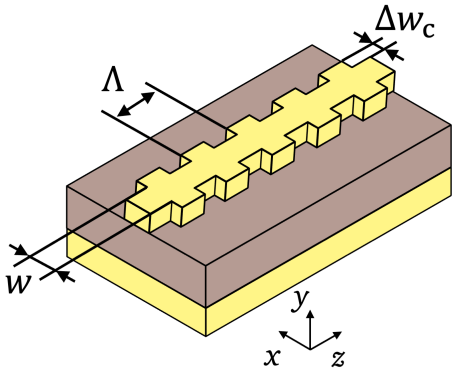

Figure 1.5 Example of corrugated waveguide. In order to reflect the light propagating along the z axis, its period Λ must fulfill the Bragg condition at the desired wavelength range.

waveguide, the radiation angle and pattern can be designed and the coupling efficiency with fibers can be optimized. For decreasing values of λ/Λ higher order radiation bands would appear in Fig. 1.4 [19].

Bragg ($m\lambda/2n_{\text{eff}} = m\lambda_{\text{eff}}/2 = \Lambda, \quad m \in \mathbb{Z}$)

The Bragg condition is met when the period of the structure is equal to a multiple of half the wavelength in the equivalent medium. In this regime, the structure acts as a distributed reflector. This operation zone is also referred as photonic bandgap in the photonic crystals literature. Higher-order Bragg zones ($m > 1$) appear alternately with radiation zones for decreasing values of λ/Λ. Bragg gratings are ubiquitous passive components in optical communications systems. Following the discovery of optical fiber photosensitivity [23], various techniques have been developed for fabricating fiber Bragg gratings [24] finding applications in filtering, amplification, lasers, dispersion compensation, mode conversion and sensing [25].

Integrated Bragg reflectors are normally constructed by periodically modulating the refractive index of an homogeneous waveguide. The strength of this modulation or perturbation categorizes Bragg grating into weak and strong. A small corrugation in waveguide sidewalls as in Fig. 1.5 is an example of weak perturbation. On the other hand, a periodic waveguide composed by core strips like the one represented in Fig. 1.4 is a case of a strong one. The modulation strength has two effects on the filter response. The more intense the modulation is, the greater the bandwith is, and less periods are required to completely reflect all the incident light.

Bragg gratings integrated into SOI platforms remain an area with potential for enhancement. As will be discussed later, the high index contrast of SOI chips difficults the realization of weak Bragg filters. Furthermore, active tunability of SOI Bragg filters has

not been yet thoroughly explored.

Subwavelength ($\lambda/\Lambda < 2n_{\text{eff}}$)

Diffraction effects of the periodic features are suppresed when the period is shorter than half the wavelength in the effective medium. Light propagates through the structure as if it were homogeneous. These metamaterials are commonly referred as Subwavelength Gratings (SWG). The mode effective index and dispersion can be engineered by thoughtfully choosing Λ and DC. Fig. 1.6 illustrates the index and dispersion capabilities of the periodic waveguide defined in Fig. 1.4 (a). SWG metamaterials inherently behave as anisotropic materials and, as shown in Fig. 1.7, its effective permittivity tensor $[\varepsilon_{ij}]$ can be also designed by adjusting the SWG geometry. Some of the contributions of this thesis delve into the planarization and homogeneization of SWG structures for their modelling. More complex tuning of the electromagnetic properties of SWGs can be done by employing alternative SWG waveguide topologies such as the ones depicted in Fig. 1.8, with their respective fundamental TE modes electric field profiles shown in Fig. 1.9.

Subwavelength gratings (SWG) have been proved to be a great solution to gain design flexibility and enhance device performance [19, 20, 32, 33]. Since their first demonstration in silicon waveguides [26, 34], a plethora of SOI-based devices have been succesfully demonstrated including edge [35] and surface [36] grating couplers, ring resonators [37], broadband multimode interference (MMI) splitters [31], mode splitter-converters [38, 39], polarization beam splitters [40], polarization splitter-rotators [41] and phase shifters for programmable circuits [42], among others. Scanning electron microscope (SEM) images of some of cited devices are shown in Fig. 1.10.

Some challenges still persist in the field of subwavelength metamaterials. The analysis of periodic subwavelength metamaterials necessitates the use of 3D Floquet-Bloch mode solvers or full-vectorial 3D FDTD simulators. The computation power needed by these types of simulation can render the design process slow and innefficient. Hence, there is a need for tools to effectively model the electromagnetic properties of SWG metamaterials.

The anisotropic properties of SWGs have been mainly utilized for achieving broadband operation [31, 43, 44]. However, there is room for improvement in the control of SWG anisotropy. For instance, SWG anisotropy engineering has barely been used for tackling the problem of SOI birefringence [45, 46]. Furthermore, fabrication restrictions on minimum feature sizes limits the design space of SWG metamaterials, underscoring the necessity for novel SWG topologies that overcome the manufacturing limitations while still granting anisotropy control.

Lastly, although SWGs have been recently used in inversely designed devices [47], no research efforts have been made in optimizing their geometry or the equivalent metamaterials. SWGs have potential for extending inverse design methodologies by in-

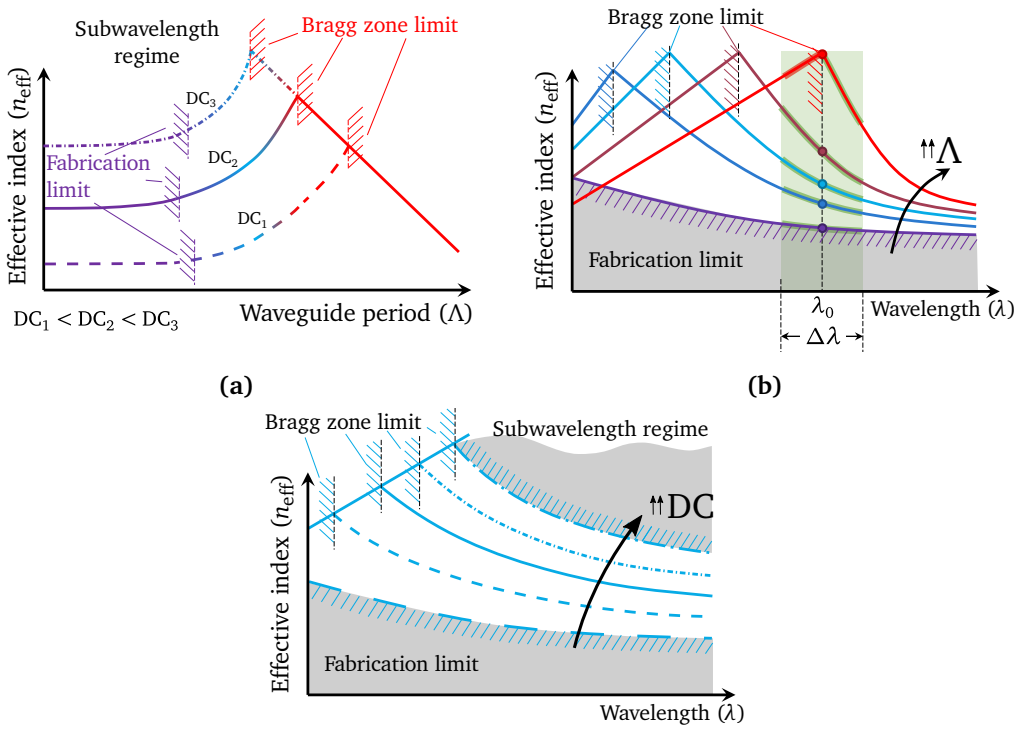

Figure 1.6 Dependence of the mode effective index with an SWG waveguide parameters, keeping fixed (a) wavelength (λ), (b) duty cycle (DC) and (c) period (Λ). The effective index can be designed by choosing a certain period and duty cycle. In addition, Λ can be used to change its slope in a bandwith $\Delta\lambda$ around the operating wavelength λ_0. The subwavelength regime is limited either by the minimum feature size or the first Bragg zone.

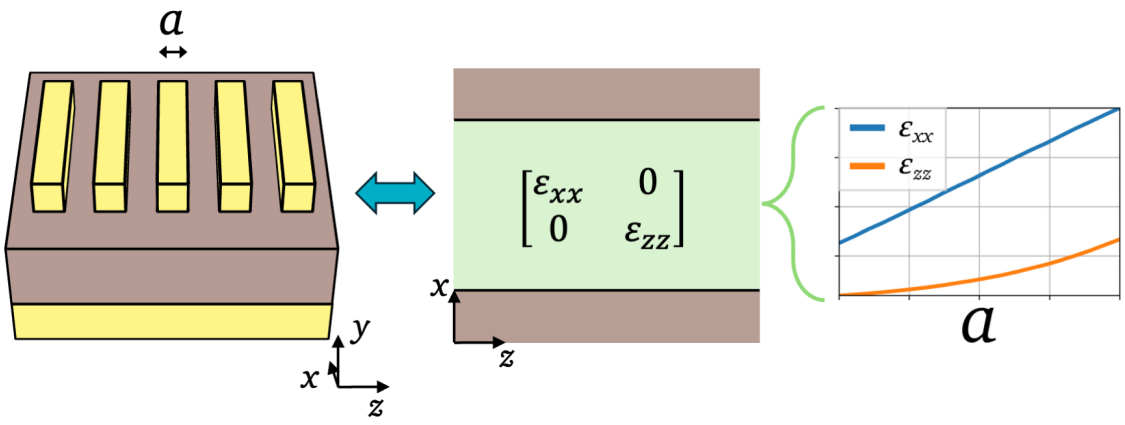

Figure 1.7 Example of anisotropic modelling of an SWG waveguide. The wave propagation properties are approximately equivalent to an homogeneous slab with an anisotropic core whose permittivity tensor components can be modelled by designing the SWG geometry.

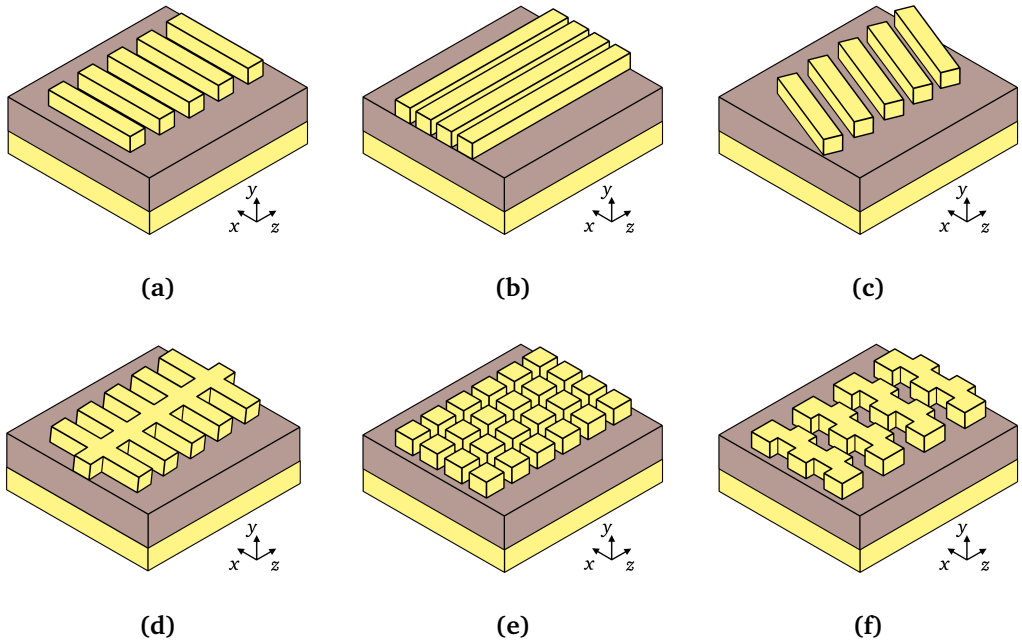

Figure 1.8 Examples of SWG waveguides: (a) lengthwise SWG [26], (b) crosswise or slot SWGs [27], (c) tilted SWG [28], (d) fishbone SWG [29], (e) multibox SWG [30] and (f) bricked SWG [31]. Light propagates in the z direction.

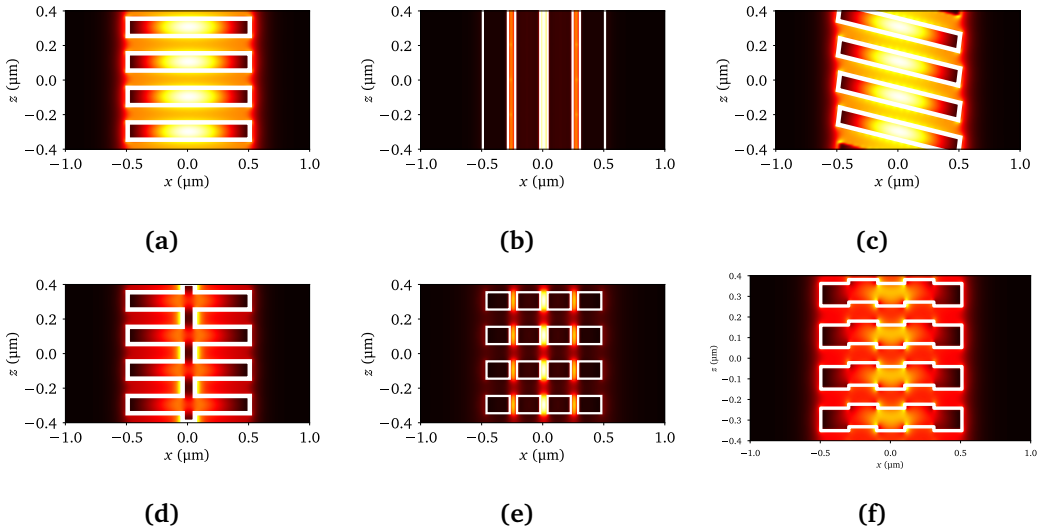

Figure 1.9 In-plane cut of the fundamental TE mode electric field magnitude for various SWG waveguides at the middle of the waveguide core: (a) lengthwise SWG [26], (b) crosswise or slot SWGs [27], (c) tilted SWG [28], (d) fishbone SWG [29], (e) multibox SWG [30] and (f) bricked SWG [31].

corporating the materials as design variables while leveraging the performance-enhancing charateristics of SWGs.

This thesis delves into three specific areas of SiPh: *(i)* anisotropy engineering of SWGs for birefringence control and polarization agnostic design, *(ii)* Bragg filter engineering applied to refractive index sensors and active multiband filters and *(iii)* inverse design of devices composed by SWGs. The following section provides an overview of the current state of each research area and outlines the objectives and contributions of the thesis.

1.2 Contributions of this thesis: challenges, state of the art and objectives

1.2.1 Modelling and engineering SWG anisotropy for birefringence control

The SOI platform is known to exhibit high birefringence [48], especially in the 220 nm-thick SOI platform, widely used by many foundries. This poses challenges, especially in scenarios where received signals have random states of polarization or in polarization division multiplexing applications. Consequently, the development of polarization-independent devices is highly desirable.

Three design approaches are normally used for achieving polarization insensitivity. The first approach involves using square Si wire waveguides [49], which excludes optical components that make use of wide or width varying waveguides. A more general solution is polarization diversity, wherein two devices are included in the chip, each designed either for Tranverse Electric (TE) or for Trasverse Magnetic (TM) polarizations [50]. However, this approach comes with the cost of doubling the required etching area and necessitating the use of polarization management devices that introduce additional loss penalties in the signal path. The third solution entails designing a device that behaves equally for both TE and TM polarizations. Examples of polarization-insensitive silicon photonic components are cascaded bent [51] and mode-evolution directional couplers [52], tapered couplers [53], broadband power splitters [54] and Bragg grating filters [55].

MMIs are fundamental IPh components for implementing devices such as power dividers, Mach Zehnder Interferometers (MZIs) or coherent receivers [56, 57]. Yet, few polarization independent Multimode Interference (MMI) couplers have been reported. Dai and He showed that polarization insensitivity can be achieved by optimizing the width of a SOI MMI [58]. However, the minimum studied silicon layer thickess was 300 nm with an optimum MMI width of 2 μm. Therefore, scaling this approach down to a 220 nm thickness becomes unattainable as the multimode waveguide becomes too

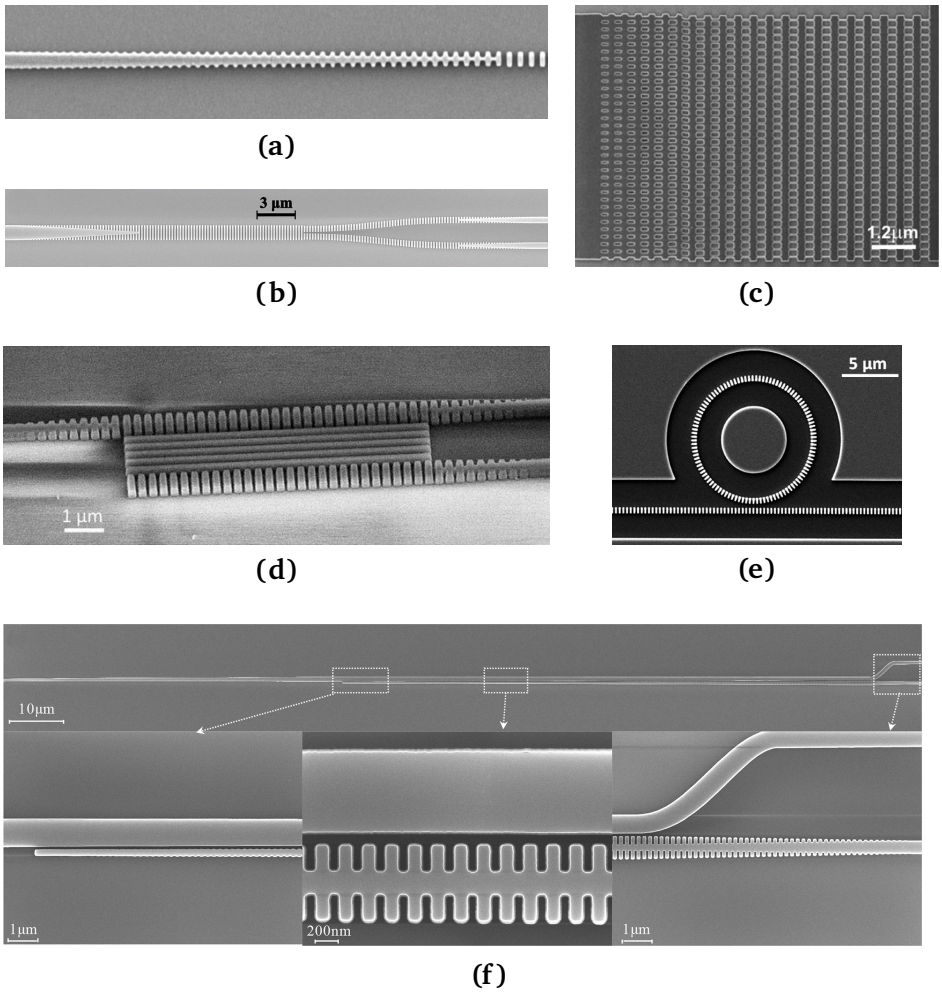

Figure 1.10 Scanning electron microscope images of demonstrated SWG devices. (a) A polarization independent edge coupler. Reprinted with permission from [35] © Optical Society of America. (b) A two-mode Y-junction. Reprinted from [38] under the terms of the CC-BY-NC-ND 4.0 license. (c) An apodized surface grating coupler. Reprinted from [19] under the terms of the CC-BY-NC-ND 3.0 license. (d) A polarization beam splitter. Reprinted from [40] with permission. (e) A high-Q ring resonator. Reprinted with permission from [37] © Optical Society of America. (f) A polarization splitter-rotator. Reprinted with permission from [41] © Optical Society of America.

narrow for multimode imaging. Alternatives to this strategies include using a silicon nitride overlay [17] or SWG waveguides [45].

SWG metamaterials offer a robust solution for mitigating SOI birefringence. SWGs have facilitated polarization independence in various applications, including fiber-to-chip edge couplers [35], directional couplers [59–61] and surface grating couplers [62]. Tilted SWG (Fig. 1.8(c)) have been used to design non-birefringent waveguides [46] as well. Furthermore, the recently proposed bricked-like SWG pattern (Fig. 1.8(f)) shows promise for achieving polarization insensitivity, owing to its demonstrated capabilities in anisotropy engineering [31]. In addition, the bricked SWG topology produces a more delocaliced mode field profile compared to regular SWG waveguides, as can be seen by comparing Figs. 1.9 (a) and (f). As a consequence, bricked SWG Floquet-Bloch modes have lower effective indices, and the start wavelength of the first Bragg zone is displaced to shorter wavelengths. This facilitates designing SWG-based devices at shorter wavelengths such as the O-band (1260–1360 nm).

Two of the contributions of this thesis focus on exploring the capabilities of the bricked SWG topology for designing polarization agnostic devices. In the first one, an existent anisotropic 2D model for SWG metamaterials was extended for efficiently solving the problem of the polarization insensitive MMI. Building upon this model, a detailed design method was proposed and used to design a polarization insensitive MMI coupler for 220 nm-thick SOI platforms and targeting the O-band. As a result, the following journal article has been published:

C. Pérez-Armenta, A. Ortega-Moñux, J. M. Luque-González, R. Halir, P. J. Reyes-Iglesias, J. Schmid, P. Cheben, Í. Molina-Fernández, and J. G. Wangüemert-Pérez, "Polarization-independent multimode interference coupler with anisotropy-engineered bricked metamaterial," *Photon. Res.*, vol. 10, no. 4, A57–A65, Apr. 2022. DOI: 10.1364/PRJ.446932

Furthermore, another polarization independent MMI coupler was designed for the C-band due to limitations in the optical test setup at the research group facilities. Test structures and their mask layouts were designed and submitted for fabrication. After successfully characterizing the device, the following paper has been published:

C. Pérez-Armenta, A. Ortega-Moñux, J. M. Luque-González, R. Halir, J. Schmid, P. Cheben, I. Molina-Fernández, and J. G. Wangüemert-Pérez, "Polarization insensitive metamaterial engineered multimode interference coupler in a 220 nm silicon-on-insulator platform," *Optics & Laser Technology*, vol. 164, p. 109 493, Apr. 2023. DOI: 10.1016/j.optlastec.2023.109493

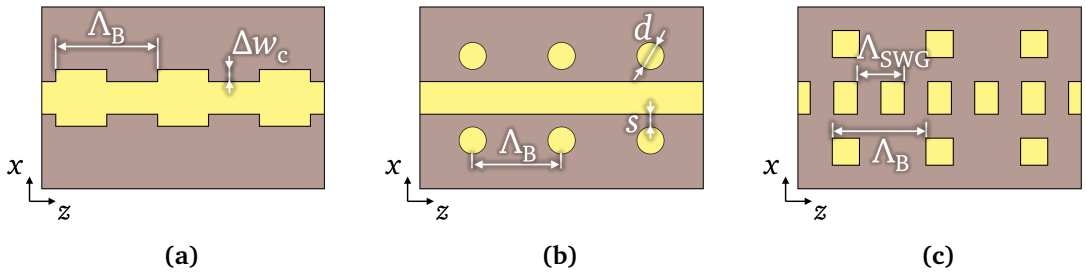

Figure 1.11 Top view of single-etch step weak Bragg gratings topologies: (a) corrugated waveguide [67], (b) cladding modulated waveguide [68] and (c) cladding modulated SWG waveguide [69]. Light propagates in the z direction. Note that in the case (c), the subwavelength period (Λ_{SWG}) is shorter than the Bragg period (Λ_B).

1.2.2 Narrowband Bragg filters for communication and sensing

Efforts to integrate Bragg filters have been made in the last decades. Particularly, various strategies have been investigated in SOI such as early two-mask etching of silicon ridge waveguides [65] or waveguide sidewall corrugations [66]. Patterning schemes using just a single etch step like corrugations, shown in Fig. 1.11(a), are desirable for reducing manufacturing complexity and costs. However, due to the high index contrast of SOI, fabrication of weak Bragg gratings is challenging. Corrugations of 10 nm are necessary to design filter bandgaps of less than 1 nm [67]. Fig 1.12 shows a SEM image of a corrugated waveguide fabricated with DUV lithography. The corrugation size is so small that is reduced and smoothened.

Tan et al. proposed the cladding modulation of strip waveguides with lateral cylinders, as depicted in Fig. 1.11(b), to overcome lithograpic resolution difficulties [68]. By maintainting the size of this lateral features fixed, the Bragg coupling strength can be controlled by the distance between the cylinders and the waveguide core. Yet, bandwidths as narrow as 8 nm were demonstrated due to SOI waveguides high confinement factor.

More recently, the combination of SWG waveguides with the cladding modulation technique was theoretically studied [69] and succesfully demonstrated [70]. The resulting grating is shown in Fig. 1.11(c). The inner SWG waveguide modal field delocalization relaxes the precision requirement in the lateral blocks positioning to achieve the desired perturbation strength. This topology has been modelled, simulated and characterized in the research group in which this thesis has been carried out. In particular, it has been used for developing filters with arbitrary spectral responses [71] in which a target filter response is translated into an apodization profile of the period and the blocks-to-waveguide separation. It has also been used in the radiation regime for developing an optical phased array with low angular divergence and beam steering through wavelength scanning [22].

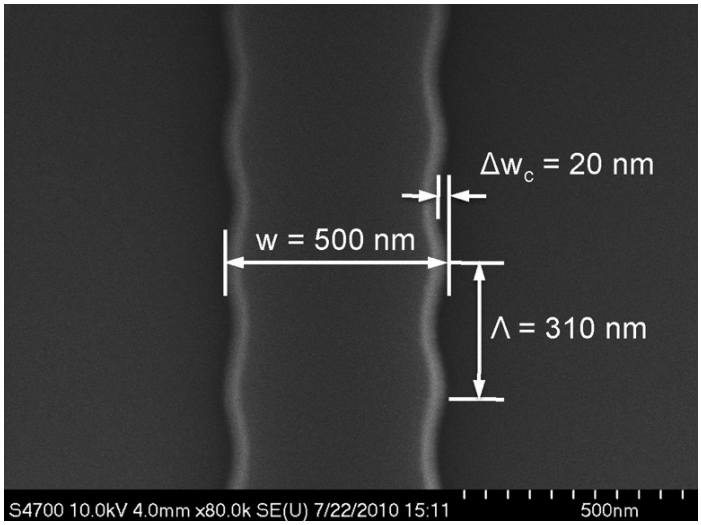

Figure 1.12 SEM image of a fabricated Bragg grating. The designed square corrugation width is 25 nm with 50% duty cycle. The fabricated grating shape is rounded and the amplitude is reduced to ∼20 nm, due to the 193-nm lithography limitations. Reprinted from [67]. © 2011 IEEE.

In another two contributions of this thesis, the cladding modulation technique is applied to (*i*) enhancing refractive index sensors in combination with an SWG waveguide, and (*ii*) developing tunable filters.

Bragg resonant refractive index sensor

An interesting and emerging research field of IPh and SiPh is sensing. SiPh presents a promising alternative for the development of integrated optical sensors, with the potential for significant cost reduction that could pave the way for massive production of point-of-care medical test, food safety controls and environment monitoring systems, ultimately leading to lab-on-a-chip systems [72, 73]. A compelling example of the impact of this technology is the active development of commercial IPh solutions for rapid antigen, antibody [74] and allergy [75] testing.

The operating principle of photonic sensors relies on evanescent field sensing, as depicted in Fig. 1.13. A guided mode propagates through a dielectric waveguide without passivation oxide cladding on it. Instead, a solution with the analyte (the substance being measured) is deposited directly onto the waveguide. The decaying part of the modal field in the analyte region interacts with it. In consequence, every change in the analyte concentration provokes a refractive index change in the cladding (Δn_c) which in turns alters the mode's effective index (Δn_{eff}). A sensing architecture is necessary as a physical transducer to convert the effective index change into a measurable quantity. Resonant and interferometric architectures are commonly employed, where the effective index change induces a resonant wavelength shift ($\Delta\lambda_r$) or a variation in the output power (ΔP_{out}), respectively. From a designer perspective, two figures of merit must be

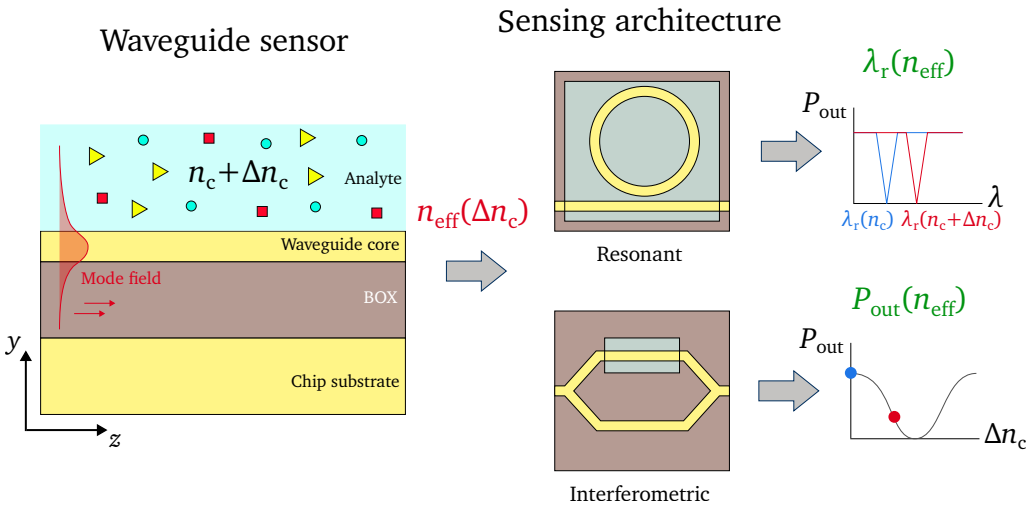

Figure 1.13 Operation principle of evanescent field sensors. The effective index n_{eff} of the mode propagating through the waveguide depends on the cladding refractive index n_c which in turns depends on the analyte concentration. The changes in n_{eff} can be mapped to a shift in the resonance wavelength λ_r with a resonant architecture like a ring resonator or to an output power (P_{out}) change through an interferometric architecture such as a Mach-Zehnder Interferometer (MZI).

optimized: sensitivity, representing the variation rate of the measured quantity with respect to the cladding refractive index ($S = \partial\lambda_r/\partial n_c$ for resonant architectures and $S = \partial P_{out}/\partial n_c$ for interferometric ones), and the limit of detection (LoD), denoting the minimum distinguishable change in the analyte. In the case of resonant sensors the intrinsic LoD (iLoD) is defined. It assumes the 3-dB bandwidth of the resonator as the minimum distinguishable wavelength shift, i.e., iLoD $= \Delta\lambda_{3\,dB}/S$. It is useful for comparing different sensors based solely on their electromagnetic properties, regardless of the read-out system charateristics.

Interferometric SiPh sensors have garnered considerable attention in the last three decades starting with pioneering works by Heidemann et al. on silicon nitride platforms [76, 77]. MZI-based sensors were subsequently explored in SOI platforms using silicon wire waveguides. Bimodal interferometric waveguides have also been proposed for silicon nitride [78]. However, interferometric architectures suffer from phase ambiguity, sensitivity fading and the LoD is dependent on the read-out system noise. More complex architectures using coherent detection and calibration to tackle these issues have been proposed more recently [79, 80].

This part of the thesis work centers on resonant sensors, which have also been extensively explored in SiPh. Early demonstration predominantly used ring resonators, obtaining sensitivities between 70 and 200 nm/RIU [81, 82]. Alternative approaches have improved the device sensitivity up to 300 nm/RIU by employing other waveguides

types like the slot waveguide [83]. In the same way, since their first proposal as sensing waveguides [84], lengthwise SWGs (Fig. 1.8(a)) have been employed to increase the sensitivity in ring resonators over 400 nm/RIU [85–88]. Multibox SWG waveguides as the one showed in Fig. 1.8(e) have also been used to obtain sensitivities up to 599 nm/RIU and iLoDs in the order of $10^{-3} - 10^{-4}$ in ring resonator and phase-shifted Bragg cavities [89, 90]. Bimodal waveguides have also been used, raising the sensitivity to 2270 nm/RIU [91]. Yet, mentioned devices still suffer from ambiguity due to the free spectral range (FSR), i.e., because of the periodicity of the frequency response of the resonators.

In another contribution of this thesis, the cladding modulated Bragg filter topology combined with a SWG waveguide (Fig. 1.11(c)) has been investigated for sensing applications. The objective of this work is to design a resonant sensor with a state-of-the-art performance sensitivity and iLoD. A model based on Coupled Mode Theory including propagation losses has been used for studying the sensor performance and developing a comprehensive design procedure, which can be extended to any Bragg-based resonant sensor. Furthermore, while the aforementioned state-of-the-art sensors have been designed for C-band, the sensor in this contribution targets O-band wavelengths. As will be discussed later, water presents less absorption loss at lower wavelengths which improve the sensor iLoD compared to a C-band sensor. As a result of this work, the following research article has been published:

C. Pérez-Armenta, A. Ortega-Moñux, J. Čtyroký, P. Cheben, J. H. Schmid, R. Halir, Í. Molina-Fernández, and J. G. Wangüemert-Pérez, "Narrowband bragg filters based on subwavelength grating waveguides for silicon photonic sensing," *Opt. Express*, vol. 28, no. 25, pp. 37 971–37 985, Dec. 2020. DOI: 10.1364/OE.404364

Integrated Bragg tunable superstructure

Bragg filters can also be integrated in tunable photonic integrated circuits, which may be desirable in real-time applications. SOI reconfigurable Bragg gratings have been designed leveraging electro-optic effects on PN junctions [93], phase change materials [94] and thermal effects [95]. This thesis focus on the latter approach. Multiple band filtering may be required in wavelength division multiplexing (WDM) systems. One approach involves the concatenation and tuning of various Bragg filters as in [95], although the relationship between the electrical configuration and band relocation is not trivial. Tunable Bragg superstructures have been studied in optical fibers [96], where a weak Bragg grating is modulated with a periodic temperature profile with a period greater than the base Bragg grating. Early explorations in the SOI platform have also been recently made [97].

The objective of this contribution of the thesis is to make a proof of concept of the

Bragg tunable superstructure technique in SOI. To this end, a temperature-tuned multi-notch Bragg filter is designed, fabricated and characterized. This work has been carried out in collaboration with the National Research Council of Canada and the Carleton University (Ottawa, Canada). As a result of these efforts, the following paper has been published:

> **C. Pérez-Armenta**, K. K. MacKay, A. Hadij-ElHouati, A. Ortega-Moñux, I. Molina-Fernández, J. G. Wangüemert-Pérez, J. H. Schmid, P. Cheben, and W. N. Ye, "Thermally induced sideband generation in silicon-on-insulator cladding modulated bragg notch filters," *Opt. Express*, vol. 31, no. 13, pp. 22 225–22 232, Jun. 2023. DOI: 10.1364/OE.488108

1.2.3 Smart photonic inverse design using subwavelength metamaterials

Conventional methodologies for the design of photonic components [99], known as *fordward design* and illustrated in Fig. 1.14(a), rely on known topologies (e.g., MMIs, directional couplers, gratings, etc.) for which analytical models may or may not exist. Ultimately, these devices must undergo evaluation in full-vectorial 3D electromagnetic solvers to assess their performance and subsequently adjust the structural parameters, either by doing parameter sweeps or using optimization algorithms. However, the size of these structures is usually directly related to the wavelength, leading to footprint and bandwidth penalties. In addition, not every circuit function has a known building block or "template" structure available for design.

With the exponential increase of computational power, *inverse design* techniques (Fig. 1.14(b)) have arisen to overcome conventional design limitations [100]. In photonic inverse design methods, device geometries are generated to meet target specifications, such as desired spectral responses or optimum figures of merits (FOMs). The user provides the optimization algorithm with an objective function to optimize, design variables that parametrize a generic photonic structure, and initialization and bounds for these variables. As the objective function is either maximized or minimized, the device behavior approaches the target performance. The process concludes with a synthesized device geometry that satisfies targets established at the begining.

While many approaches and algorithms have been extensively studied, the use of inverse design procedures together with SWG structures remains barely explored [47]. Given the versatility and enhancing properties of SWGs, as evidenced in the bibliography and the publications endorsing this thesis (chapter 2), combining these structures with inverse design algorithms shows promise for advancing silicon photonic systems.

In the last work of this thesis, a novel photonic inverse design method that leverages

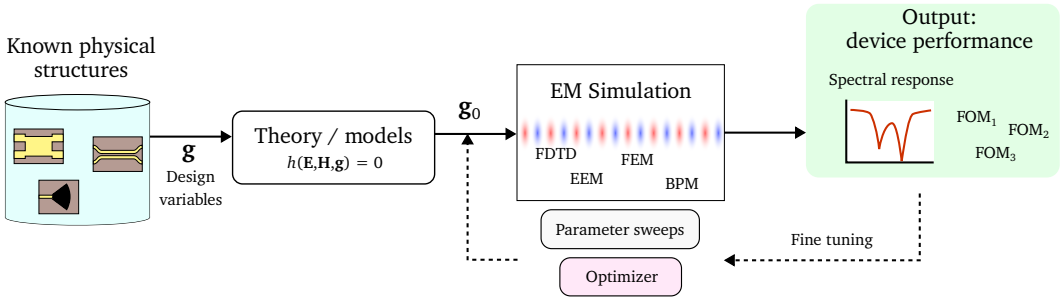

(a) Fordward design

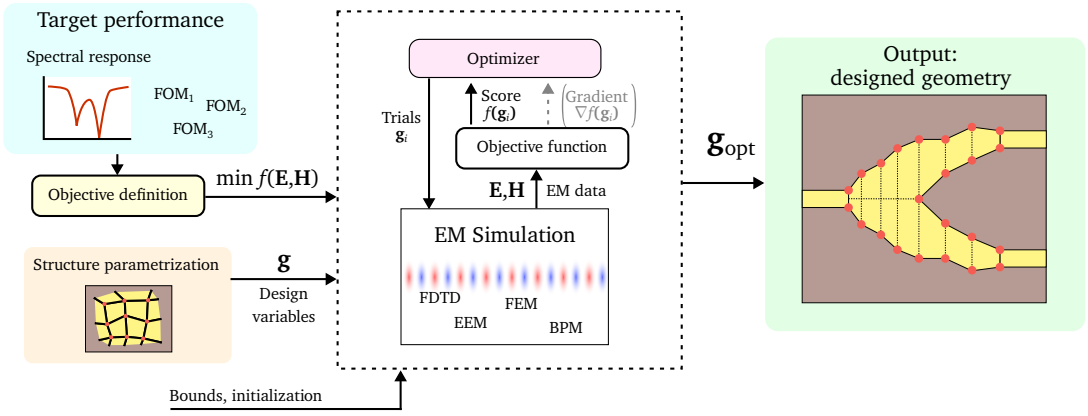

(b) Inverse design

Figure 1.14 Simplified comparison between (a) forward and (b) inverse design methodologies. In forward design, known device topologies are used. The behavior of these devices is typically described by (sometimes approximate) closed expressions which serve to find the geometry parameters $\mathbf{g}_0$. The device is then introduced in an electromagnetic simulation to assess its performance. Normally, adjustments to the geometry are made in simulation to optimize the performance and compensate approximations done in the analytic models. In contrast, inverse design begins with a generic parametrizable geometry, such as a waveguide contour. These design variables along with bounds, initial candidates and one or more objectives are passed to an optimization algorithm. The process concludes when the optimizer converges to an optimal geometry $\mathbf{g}_{\text{opt}}$.

subwavelength structures is proposed and used for designing an ultra-short and broadband spot-size converter. This method makes use of anisotropic modelling to accelerate the optimization process and has been deployed in the supercomputing facilities of the University of Málaga. A more thorough introduction and the details of the work can be found in chapter 3.

1.2.4 Goals summary

The objectives previously presented in this section are summarized below:

1. Demonstrate the bricked SWG metamaterial for polarization independent operation

- 1.1 Extend existent anisotropic effective medium modelling technique to TE and TM polarizations and apply it to the bricked SWG topology [Fig. 1.8(f)].
- 1.2 Design a polarization independent MMI coupler for a 220 nm-thick SOI platform in O-band.
- 1.3 Design a polarization independent MMI coupler for a 220 nm-thick SOI platform in C-band.
- 1.4 Design a test layout and demonstrate the C-band MMI design through experimental characterization.

2. Explore the performance as a sensor of a novel Bragg grating topology

- 2.1 Leverage Coupled Mode Theory for the analysis and design of a lossy Bragg filter.
- 2.2 Develop a design method for Bragg resonant sensors.
- 2.3 Target wavelengths within the O-band to enhance the sensor performance.
- 2.4 Design a state-of-the-art resonant sensor using the developed methodology and the topology of Fig. 1.11(c).

3. Realize a proof of concept of a temperature-controlled Bragg multiband filter

- 3.1 Develop a simulation framework for the Bragg superstructure.
- 3.2 Design tunable Bragg filters and their test layouts.
- 3.3 Experimentally demonstrate the filter tunability and sideband generation.

4. Develop a new inverse design technique using SWG metamaterials

- 4.1 Select optimization algortihms and develop an interface with the electromagnetic simulator Meep.
- 4.2 Leverage 2D effective anisotropic models for efficient optimization.
- 4.3 Deploy the optimization process in University of Malaga's supercomputer.
- 4.4 Design an state-of-the-art spot-size converter to verify the methodology.

1.3 Organization of the thesis

The present thesis have been done in the compendium or collection of articles modality. According to the university's doctorate regulations, the thesis must include a description of the thesis objectives, a state-of-the-art literature review, a description of the results including any relevant aspect not covered in the endorsing papers followed by a compilation of the publications as they were published, the conclusions and the bibliography. These contents, outlined in Fig. 1.15, are organized in the manuscript as follows.

Chapter 1 is the current introduction, including the literature review and objectives of the thesis.

Chapter 2 provides an overview of the publications endorsing this thesis, summarizing the relevant results of the research. It also describes other non-academic contributions made for supporting the research group activity. Finally, the publications are appended.

Chapter 3 contains the work carried out in the thesis regarding inverse design with SWG metamaterials. The modelling techniques, methods developed and deployed infrastructure are detailed. The method developed in this part of the thesis is used to design a very short spot-size converter in SOI.

Chapter 4 draws the conclusions and proposes future research lines.

Appendix A contains CMT-based derivations of the spectral responses of lossy Bragg filters and Bragg superstructures.

Appendix B is the Spanish summary of the Thesis.

Appendix C shows the Curriculum Vitae of the author.

(Sec. 2.1.2) # Polarization insensitive MMI coupler

Modelling, design and simulation

[63] C. Pérez-Armenta et al., *Phot. Res.* **10** (4) A57–A65 (2022)

- First time in 220 nm-thick SOI
- Anisotropic modelling for both polarizations
- Wavelength range: 1.26–1.42 µm
  - Excess loss < 1 dB
  - Imbalance < 1 dB
  - Phase error < 5°

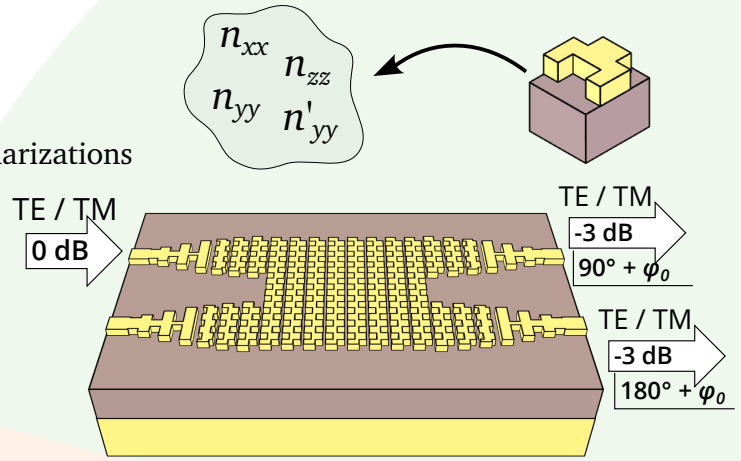

Experimental validation

[64] C. Pérez-Armenta et al., *Opt. & Laser Tech.* **164** 109493 (2023)

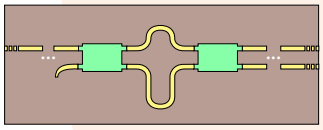

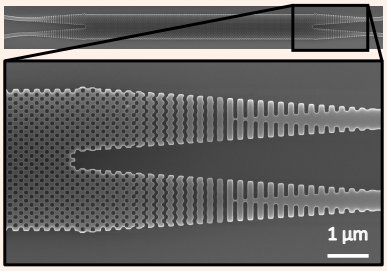

- Wavelength range: 1.49–1.58 µm (measurement setup)
- Footprint: 3.5 µm × 47.25 µm
- Performance:
  - Polarization dependent loss < 1 dB
  - 0.7 dB < Excess loss < 1 dB
  - Imbalance < 1 dB from 1.5 to 1.56 µm
  - Phase error < 5°

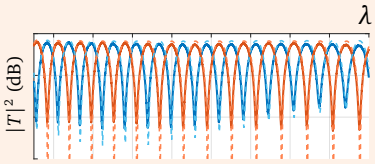

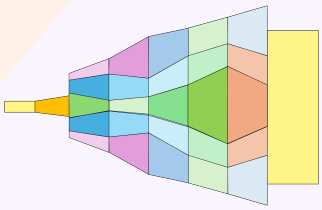

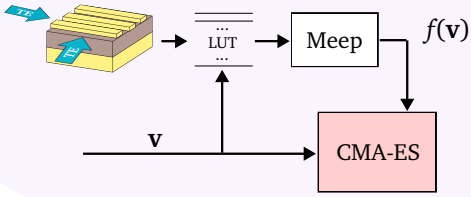

- 2D anisotropic modelling of SWGs
- Optimization using CMA-ES algorithm

Figure 1.15 Overview of the contributions of this thesis.

Narrowband Bragg sensor

(Sec. 2.1.1)

[92] C. Pérez-Armenta et al., *Opt. Expr.* **28** (25) 37971–37985 (2020)

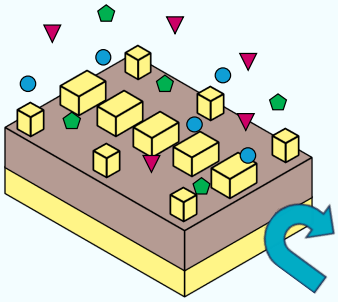

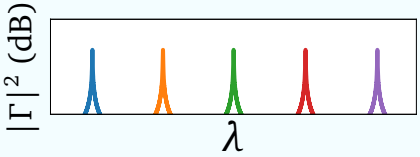

- SWG waveguides: high sensitivity
- Cladding modulation: low iLoD
- CMT model for lossy modes
- O-band for enhanced LoD
- Designed bandgap: ~ 30 pm
- Device sensitivity: **507 nm/RIU**
- intrinsic LoD: $\mathbf{5.1 \cdot 10^{-5}}$ **RIU**

Temperature-controlled Bragg grating superstructure

(Sec. 2.1.3)

[98] C. Pérez-Armenta et al., *Opt. Expr.* **31** (13) 22225–22232 (2023)

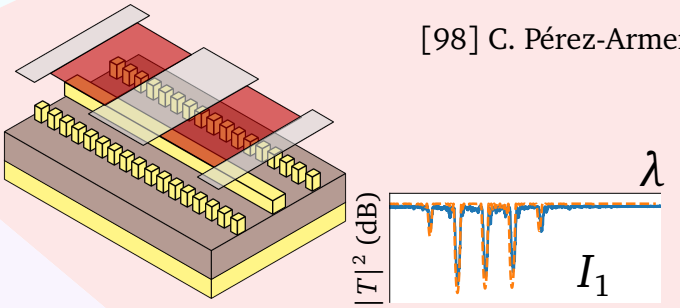

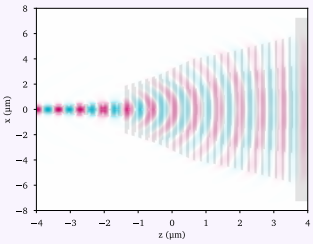

- Cladding modulated Bragg topology
- Designed bandgap: 1 nm
- Designed sideband spacing: 5 nm
- Good simulation-experiment agreement

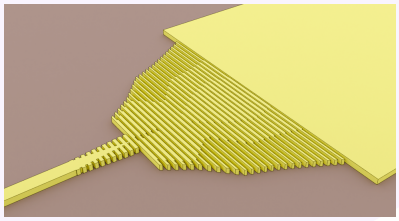

SWG-assisted smart inverse design

(Chapter 3)

- Deployment on University of Málaga's supercomputer
- Designed a 7 μm-long Spot-Size Converter from 500 nm to 12 μm with 0.5 dB insertion losses and >100 nm bandwidth.

Chapter 2

Overview of the thesis publications

This chapter provides a comprehensive summary of the published contributions developed throughout the thesis, showcasing the research of this work as a compilation of peer-reviewed articles. As introduced in the previous chapter, all the work of the thesis is focused on silicon photonic devices, particularly on the silicon on insulator (SOI). The different works of this thesis make use of periodic structures to provide SOI devices with more functionalities or enhance existent ones.

The first publication explores a recently proposed Bragg filter topology as a way of developing resonant refractive index sensors. O-band operation is targeted since the lower absorption losses relax design constraints and enable a 10-fold enhancement of the intrinsic limit of detection. The second and third publications explore for the first time the design and experimental characterization of polarization insensitive MMI couplers in a 220 nm-thick SOI platform. Polarization agnostic behavior is implemented by introducing a bricked-like subwavelength grating pattern in the multimode core of the MMI. Thanks to this structure, birefringence is engineered to equal the self-imaging distance of the MMI for both polarizations. The fourth publication introduces a periodic heating configuration on a cladding modulated Bragg filter to generate sidebands. By increasing the current injected on the system or equivalently the temperature modulation amplitude, the amplitude of the sidebands can be controlled.

Finally, some additional tasks carried out during the thesis to the support of the research activity of the group are also described, followed by the publications endorsing this thesis.

2.1 Overview of the designed devices

2.1.1 Narrowband Bragg refractive index sensor

The first landmark of the thesis was the design of a resonant refractive index sensor with superior performance. The main objective was to enhance two critical figures of merit of the sensor: sensitivity and intrinsic limit of detection (iLoD). That was accomplished by implementing the Bragg filter topology proposed in refs. [69, 70], depicted in Fig. 2.1, and opting for an operational wavelength of 1310 nm. The rationale behind these choices is rooted in the following:

- The demonstrated high sensitivity of the inner SWG waveguide [84].
- The cladding modulation technique which enables easily manufacturable narrowband filters [68] resulting in a low iLoD.
- The diminished light absorption of water in O-band relaxes constraints on the filter bandwidth, thus contributing to the further reduction of the iLoD.

The associated publication to this study delves into the modeling of Bragg filters using Coupled Mode Theory (CMT) including the effect of the fundamental mode propagation loss. Derivation of expression of a lossy Bragg filter reflectance is given in appendix A, sec. A.1. Through a comprehensive analysis of the derived expressions, a trade-off between the bandwidth, losses and signal level is identified, leading to a thorough design method outlined in the paper.

During the design phase it was found that TE polarization exhibits higher sensitivity to changes in the cladding compared to TM polarization. This observation finds support in perturbational theory, since the fundamental TE mode of the SWG waveguide has a more significant field overlap in the cladding region, while the TM mode has a substantial part in the buried oxide (BOX) region. Furthermore, a proper election of the waveguide duty cycle and aspect ratio (w/h, see Fig. 2.1) is crucial for increasing the device sensitivity.

The final design, detailed in Table 2.1, is finally evaluated using CMT. A device sensitivity of 507 nm/RIU and an iLoD of $5.1 \cdot 10^{-5}$ RIU are obtained. Detailed discussions on the modeling and design of the sensor can be found in the publication titled "*Narrowband Bragg filters based on subwavelength grating waveguides for silicon photonic sensing*" [92].

h	h_{BOX}	w	Λ_{SWG}	DC	s	t, u	Λ_{B}	L
340 nm	3 μm	300 nm	215 nm	55 %	950 nm	100 nm	422 nm	23 mm

Table 2.1 Final design of [92]. Geometrical parameters are defined in Fig. 2.1, except L which is the total length of the device. The sensor is designed for the operating wavelength of $\lambda = 1310$ nm and TE polarization.

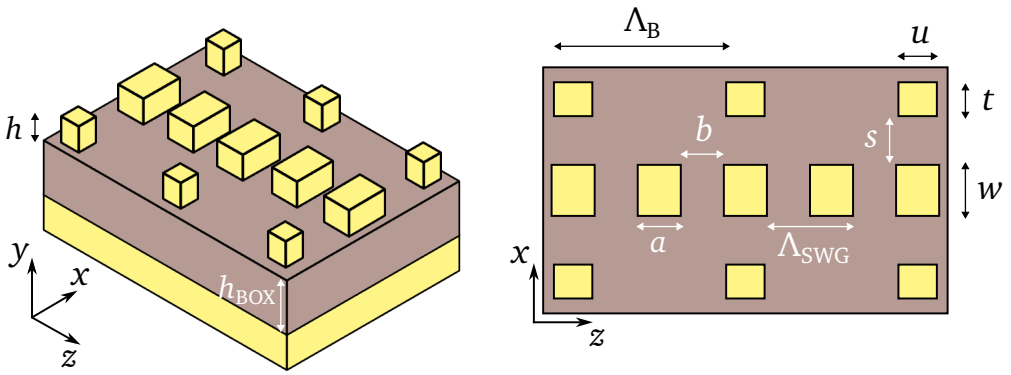

Figure 2.1 Geometry of the Bragg filter used as a sensor in [92]. A narrow bandgap is created in a SWG waveguide of period Λ_{SWG} and duty cycle DC $= a/\Lambda_{SWG}$ by periodically adding lateral blocks of size $t \times u$ and pitch Λ_B.

2.1.2 Polarization insensitive MMI couplers

The second milestone of the thesis was the design and characterization of a polarization independent multimode interference coupler for the 220 nm-thick SOI platform. To do so, the bricked-like periodic metamaterial first proposed in [31] was employed in the multimode waveguide (see Fig. 2.2). The modelling technique presented in [31] showed that the electric permitivitty tensor components affecting TE polarization can be easily tuned by adjusting the geometry of the SWG metamaterial, while the TM component remains nearly unchanged. This suggested that a certain combination of waveguide parameters can equal the device's performance for both polarizations.

In the second publication endorsing this thesis [63], the 2D modelling technique previously used in [43] in an anisotropic MMI designed for the TE polarization is leveraged and extended to TM polarization. A key conclusion of the work derived from this model was that a block shift of approximately half of the longitudinal period is necessary for polarization insensitive operation. In addition, the approximated 2D model provided an initial waveguide design that expedite the design process. This preliminary design was subsequently introduced in a full-vectorial 3D FDTD simulator, serving as an initial guess for optimizing the MMI's figures of merit.

The MMI coupler was designed for O-band aiming to validate the feature size constraints relaxation of the bricked SWG topology. Since the operational wavelength is reduced with respect to the C-band, the Bragg condition in the periodic waveguide becomes more restrictive. The field delocalization effect of the bricked shifting decreases the effective index of the supported modes thus increasing the subwavelength spectrum range. The successful realization of the MMI coupler confirmed this property.

As a result of the design method, a 2×2 MMI coupler with excess loss and imbalance of less than 1 dB and a phase error below 5° in the wavelength range of 1.26–1.42

μm was achieved. The details on the modelling and design of the device are discussed below in the publication "*Polarization-independent multimode interference coupler with anisotropy-engineered bricked metamaterial*" [63].

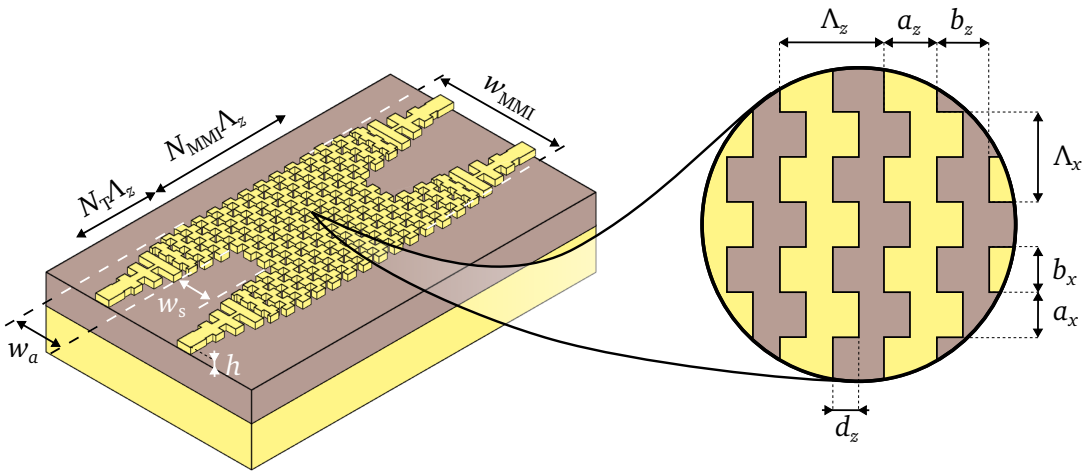

Figure 2.2 Multimode interference coupler geometry implemented in [63, 64]. A brick-like metamaterial pattern is used in the multimode waveguide core. The silicon strips of a regular SWG waveguide of period Λ_z and duty cycle $DC_z = a_z/\Lambda_z$ are periodically split in the transverse direction with period Λ_x and duty cycle $DC_x = a_x/\Lambda_x$. Then, the resulting blocks of size $a_x \times a_z$ are shifted in the propagation direction by a distance d_z.

	λ	h	Λ_z (DC_z)	Λ_x (DC_x)	d_z	w_{MMI}
[63]	1310 nm	220 nm	220 nm (50 %)	200 nm (50 %)	110 nm	2.9 μm
[64]	1550 nm	220 nm	250 nm (60 %)	200 nm (50 %)	120 nm	3.5 μm

	N_{MMI}	w_a	w_s	N_T
[63]	121	1.2 μm	0.8 μm	21
[64]	129	1.6 μm	0.4 μm	15

Table 2.2 Geometrical parameters of the designed polarization independent MMI couplers as defined in Fig. 2.2. One design is centered at O-band [63] and the other at C-band [64].

Due to limitations in the measurement facilities of the group at the time of fabrication, particularly on the tunable laser source's wavelength range, the device had to be redesigned for the C-band. A set of test structures incorporating variations in the geometrical parameters of the coupler nominal design were drawn in a mask, shown in Fig. 2.3. These test structures consisted of unbalanced Mach-Zehnder interferometers where the splitter/combiner elements were two copies of the design. This configuration

allowed for the inference of the wavelength response of the MMIs from the measurement data.

The chip mask was sent to a multiproject wafer run at Applied Nanotools Inc. facilities [16]. The devices were fabricated using electrom beam lithography for the patterning of a 220 nm-thick SOI wafer, with a 2 μm BOX layer and a 2.2 μm SiO_2 cladding layer. Once the sample was received, the device was characterized using the measurement set-up depicted in Fig. 2.4. Light from a tunable laser source is polarized and rotated to the desired polarization state and coupled into the chip using a lensed fiber and broadband SWG edge couplers [35]. On the chip, the light is guided to the device under test and then directed to two output edge couplers. The output light is collimated using a microscope objective, filtered by Glan-Thompson polarizer and intercepted by a germanium photodetector. An iris diaphragm is placed to avoid crosstalk between the outputs of the interferometer. The photodiode power is measured by a digital power meter and sent to a workstation through a data acquisition system. Alternatively, light can be captured with a infrared camera using a mirror on a flip mount postioned after the polarizer.

The performance metrics of the MMI coupler were extracted from the raw interferograms, leading to an excess loss below 1 dB, polarization-dependent loss of less than 0.25 dB and a phase error within ±5° across the wavelength range of 1495 – 1580 nm. The imbalance was in this case more limiting, being the 1 dB bandwith of 60 nm. This is the first demonstrated polarization insensitive MMI coupler in the SOI platform for the silicon thickness of 220 nm. More information on the characterization of the device can be found below in the publication "*Polarization insensitive metamaterial engineered multimode interference coupler in a 220 nm silicon-on-insulator platform*" [64].

2.1.3 Bragg filter sideband generation and tuning

The third significant achievement of the thesis involved the assessment of a tunable multiband filter technique in the SOI platform. This work was carried out in a collaboration project between the Photonics & RF Research Laboratory (University of Málaga), the Silicon Micro/NanoPhotonics Group (Carleton University) and the Advanced Electronics and Photonics Research Centre (National Research Council Canada).

The geometry of the device is shown in Fig. 2.5. For this purpose, a cladding modulated Bragg topology, akin to the one discussed in sec. 2.1.1, was utilized as a base filter. It is based on a published design for TM polarization [71]. Block separation and length were modified to obtain a 1 nm bandgap with 99.99 % reflectivity. Subsequently, a set of heaters was periodically placed along the Bragg filter structure, with a significantly larger period than the Bragg one. This heater arrangement forms a Bragg superstructure, creating a series of replicas of the original Bragg filter reflectance spectrum around the

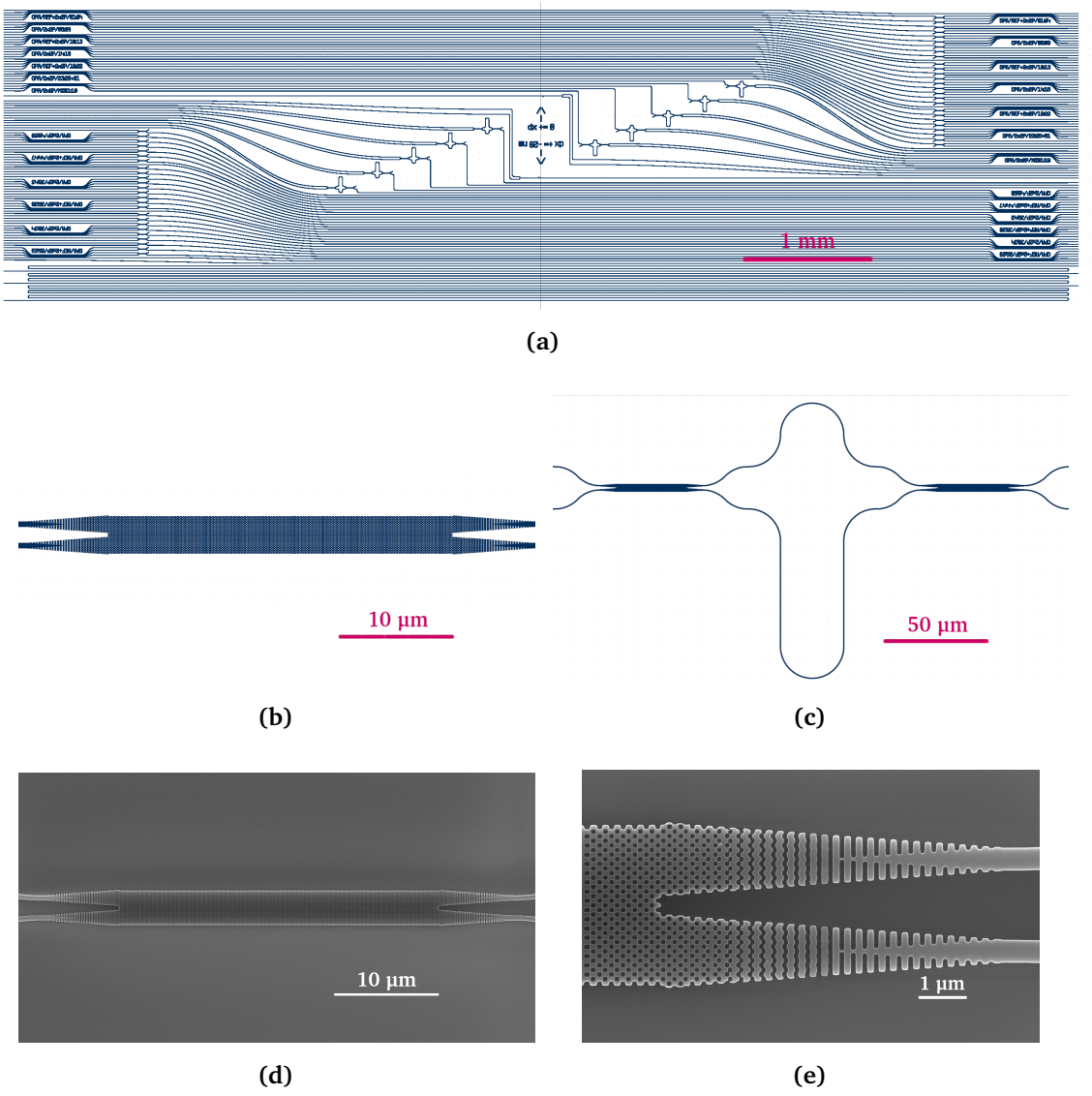

Figure 2.3 (a) Test layout for characterizing the polarization insensitive MMI coupler. Test structures included (b) isolated MMI couplers and (c) Mach Zehnder interferometers. (d,e) SEM images of one of the fabricated MMIs.

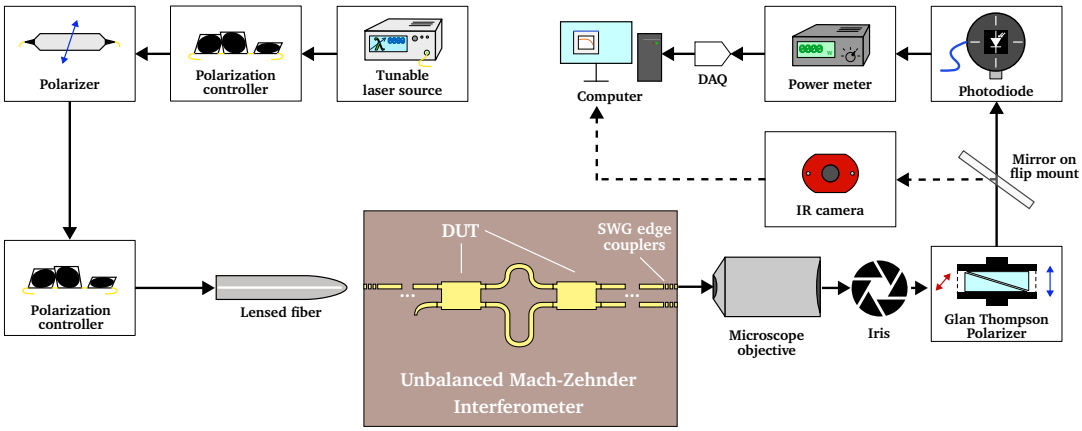

(a)

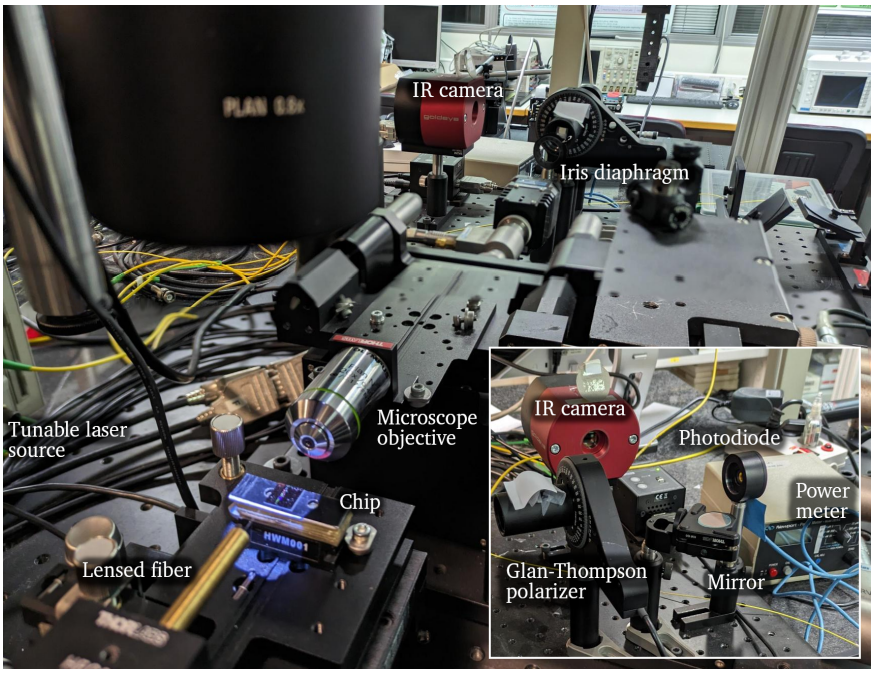

(b)

Figure 2.4 (a) Schematic and (b) picture of the measurement setup employed in the characterization of the polarization insensitive MMI coupler.

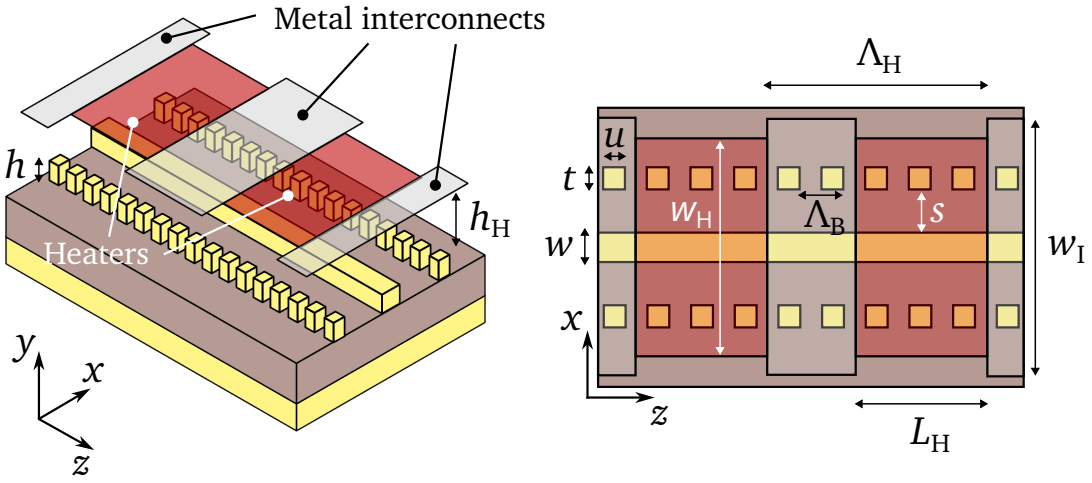

Figure 2.5 Geometry of the tunable filter demonstrated in [98]. It is based on a weak cladding modulated Bragg filter. Oxide cladding is not shown for clarity. Heater strips are placed periodically on top of the Bragg filter with period Λ_H and duty cycle $DC_H = L_H/\Lambda_H$. The filter is designed for the operating wavelength of $\lambda = 1550\,nm$ and TM polarization.

h	w	s	t	u	Λ_B	L
220 nm	400 nm	389 nm	150 nm	150 nm	458 nm	1 mm

h_H	w_H	w_I	Λ_H	DC_H
1.98 µm	4 µm	10 µm	116.4 µm	50 %

Table 2.3 Final design of [98]. Geometrical parameters are defined in Fig. 2.5. L is the total length of the filter.

Bragg resonance wavelength. The spacing and amplitude of the new generated sidebands can be controlled by the heater period and the maximum temperature increment, respectively. The relationship between the temperature profile and the amplitude and separation of the sidebands is derived in Appendix A, sec. A.2. Table 2.3 shows the nominal geometry of the device.

As in the work described in the previous section, a layout with variations of the nominal design (Fig. 2.6) was submitted to the same foundry. The fabrication process was the same plus the deposition of the heater layer (a 200-nm thick titanium-tungsten alloy) and the interconneting metals (a 500-nm thick aluminum layer). Photolithography was employed to pattern the metal layout, followed by the deposition of an additional 300-nm thick SiO_2 layer was deposited for passivation. Upon completion, the sample was received at the National Research Council of Canada where the experimental characterization of the chip test structures was conducted during a research visit of the candidate. The measurement setup employed for that purpose is depicted in Fig. 2.7. This setup is

similar to the one used in the previous section plus the addition of a digital voltage source connected to metallic pads in the chip using electrical probes.

Measurements showed excellent agreements compared to simulations performed using the layer adding algorithm [101]. Some corrections had to be added to the model mapping the input current to the temperature profile in order to consider a larger wavelength shift attributed to a lack of dissipation in the chip as well as a silicon layer thickness error that shifted the Bragg wavelength at room temperature. More information about this work can be found below in the publication "*Thermally induced sideband generation in silicon-on-insulator cladding modulated Bragg notch filters*" [98].

2.2 Additional work

Besides the academic contributions of the thesis, supplemental work was carried out to support the research group activities.

2.2.1 Meep and MPB wrapper library

All the electromagnetic simulations conducted in this thesis use the open-source electromagnetic simulators MPB [102, 103] and Meep [104, 105]. Both simulators share the same user interface which consists of a Python programming interface. While it facilitates extensive customization in simulation setup, it has a steep learning curve.

The majority of simulation scripts used in the thesis were rather long and remained the same except for the geometry definition. Thus, to facilitate code maintaining, reusability and debugging, the Python package `photonicsrf-meep` has been developed. This wrapper library for Meep and MPB provides a series of recurring predefined simulation scenarios, simplifying the process to the following steps:

1. Define a set of simulation parameters,
2. Choose the simulation type,
3. Construct the problem geometry, and
4. Run the simulation.

The library will automatically process and save the results while still giving access to low-level Meep features. Furthermore, the library directly enables parameter sweeping. Currently, the following simulation types are included:

- Calculate the band diagram of a structure (MPB)
- Calculate waveguide modes and its effective indices (MPB)
- Calculate waveguide modes and its complex effective indices (Meep)

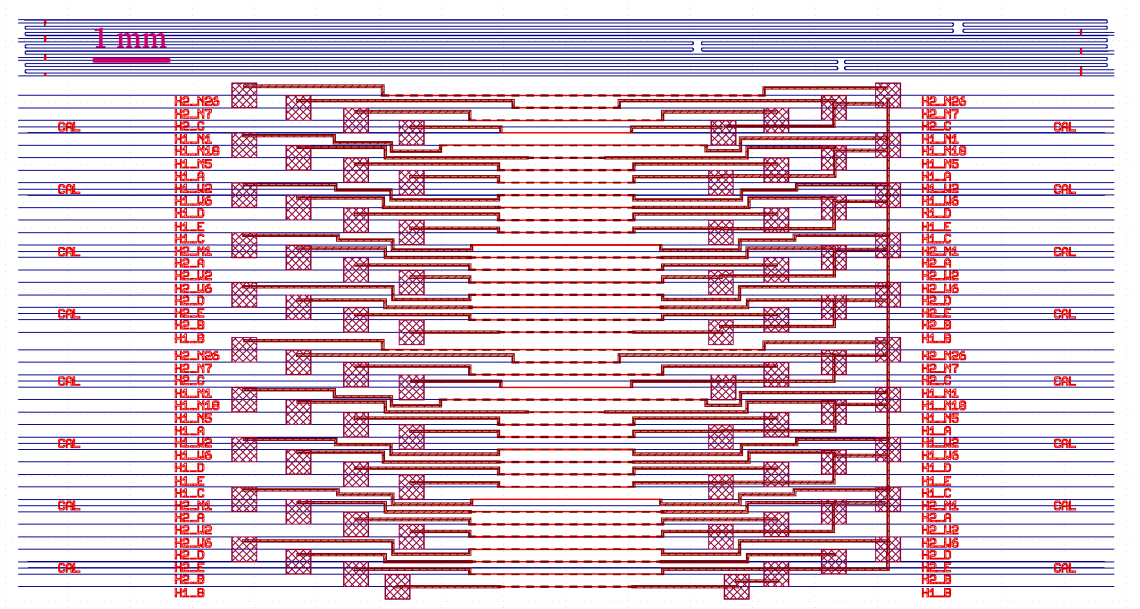

(a)

(b)

(c)

Figure 2.6 (a) Test layout for characterizing the tunable Bragg filter. Closer views of the mask are shown in (b) and (c).

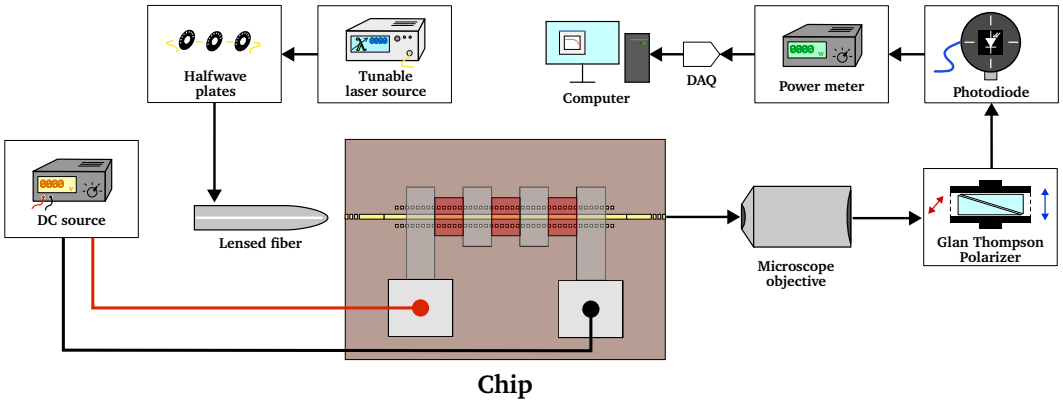

(a) Schematic of the setup

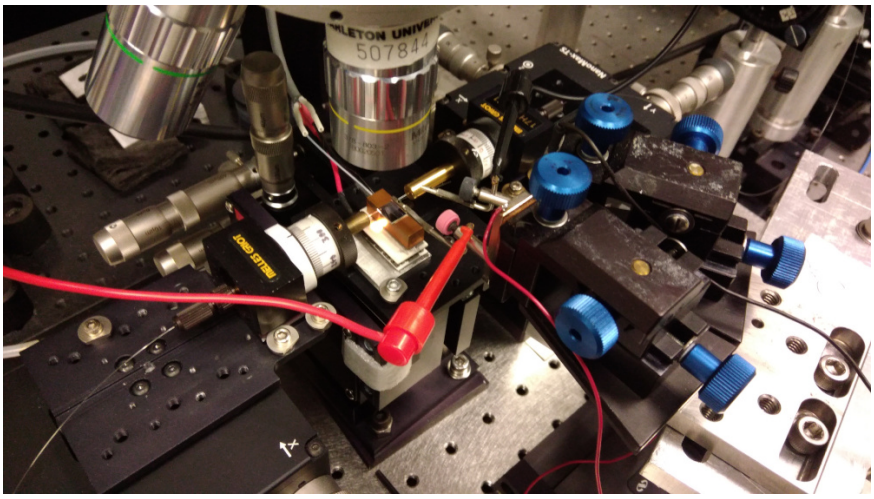

(b) Picture of the chip being characterized.

Figure 2.7 Measurement setup employed in the characterization of the tunable Bragg filter.

- Calculate the S-parameters of a photonic device (Meep)
- Calculate the S-parameters of a photonic device defined as a GDS file (Meep)
- Use the adjoint method for a given objective function in a material grid region (Meep)

This package is also intended to facilitate electromagnetic simulations in Meep/MPB to both novice and experienced users. Already adopted by the group's research staff, the package provides a common place for the research group members to contribute with their simulation scripts, promoting knowledge sharing and script exchange with other colleagues.

2.2.2 Layout library and procedures definition

Mask layout files submitted to foundries were generated using the Python library Nazca Design [106]. As with the previous section, additional efforts were dedicated to gather all reusable code and facilitate beginner users to generate masks. Building upon Nazca Design, the `photonicsrf-layout` package has been developed with the following features:

- Defining a process development kit (PDK) for each foundry used by the group including interconnect defaults, building blocks, layer structure definitions and chip templates.
- A collection of parametric building blocks frequently employed by the group.
- Utility functions for operating with Nazca cells.

Leveraging this package in conjunction with the version control software Git [107], procedures for colaborative mask depelopment have also been defined. A dedicated Git server has been deployed within the group facilities and basic training courses have been taught.

The package and procedures defined are already being used at the group and have successfully made the mask generation process more efficient. As in the previous section, this package also serves as a centralized site to gather reusable code from other masks, such us commonly used parametric devices or helper interconnection routines.

2.3 Publications

The devices presented in this chapter are thoroughly documented in four research publications that endorse this thesis. These publications are presented in chronological sequence below, along the individual contributions of the PhD candidate to each publication [63, 64, 92, 98].

- **Narrowband Bragg filters based on subwavelength grating waveguides for silicon photonic sensing**

  The first publication of this thesis. It encompasses the modelling and design of a lossy Bragg filter as a resonant sensor.

  Contributions of the candidate: design methodology, formal analysis, simulation, visualization, writing (original draft).

- **Polarization-independent multimode interference coupler with anisotropy-engineered bricked metamaterial**

  This publication covers the modelling and design of a polarization insensitive MMI coupler for the O-band, demonstrating in simulation for the first time that its feasibility in a 220-nm thick SOI platform.

  Contributions of the candidate: design methodology, formal analysis, simulation, visualization, writing (original draft).

- **Polarization insensitive metamaterial engineered multimode interference coupler in a 220 nm silicon-on-insulator platform**

  In this work, a polarization insensitive MMI coupler designed for the C-band is experimentally demonstrated for the first time in a 220-nm thick SOI platform.

  Contributions of the candidate: design methodology, formal analysis, simulation, layout design, experimental characterization, visualization, writing (original draft).

- **Thermally induced sideband generation in silicon-on-insulator cladding modulated Bragg notch filters**

  This article comprises the demonstration of a tunable Bragg superstructure in silicon photonics.

  Contributions of the candidate: simulation, experimental characterization, writing (original draft).

Note: *Following the University guidelines, the publications have been replaced in the published version of the thesis by their citation, DOI and abstract to comply with copyright policies of the academic journals. They can be accessed online through the links provided below.*

C. Pérez-Armenta, A. Ortega-Moñux, J. Čtyroký, P. Cheben, J. H. Schmid, R. Halir, Í. Molina-Fernández, and J. G. Wangüemert-Pérez, "Narrowband bragg filters based on subwavelength grating waveguides for silicon photonic sensing," *Opt. Express*, vol. 28, no. 25, pp. 37 971–37 985, Dec. 2020. DOI: 10.1364/OE.404364

Abstract: Subwavelength grating (SWG) waveguides have been shown to provide enhanced light-matter interaction resulting in superior sensitivity in integrated photonics sensors. Narrowband integrated optical filters can be made by combining SWG waveguides with evanescently coupled Bragg gratings. In this paper, we assess the sensing capabilities of this novel filtering component with rigorous electromagnetic simulations. Our design is optimized for an operating wavelength of 1310 nm to benefit from lower water absorption and achieve narrower bandwidths than at the conventional wavelength of 1550 nm. Results show that the sensor achieves a sensitivity of 507 nm/RIU and a quality factor of 4.9×10^4, over a large dynamic range circumventing the free spectral range limit of conventional devices. Furthermore, the intrinsic limit of detection, 5.1×10^{-5} RIU constitutes a 10-fold enhancement compared to state-of-the-art resonant waveguide sensors.

Journal: Optics Express

Published: December 2, 2020

URL: https://doi.org/10.1364/OE.404364

C. Pérez-Armenta, A. Ortega-Moñux, J. M. Luque-González, R. Halir, P. J. Reyes-Iglesias, J. Schmid, P. Cheben, Í. Molina-Fernández, and J. G. Wangüemert-Pérez, "Polarization-independent multimode interference coupler with anisotropy-engineered bricked metamaterial," *Photon. Res.*, vol. 10, no. 4, A57–A65, Apr. 2022. DOI: 10.1364/PRJ.446932

Abstract: Many applications, including optical multiplexing, switching, and detection, call for low-cost and broadband photonic devices with polarization-independent operation. While the silicon-on-insulator platform is well positioned to fulfill most of these requirements, its strong birefringence hinders the development of polarization-agnostic devices. Here we leverage the recently proposed bricked metamaterial topology to design, for the first time, to our knowledge, a polarization-independent 2×2 multimode interference coupler using standard 220 nm silicon thickness. Our device can be fabricated with a single etch step and is optimized for the O-band, covering a wavelength range of 160 nm with excess loss, polarization-dependent loss, and imbalance below 1 dB and phase errors of less than 5°, as demonstrated with full three-dimensional finite-difference time-domain simulations.

Journal: Photonics Research

Published: March 11, 2022

URL: https://doi.org/10.1364/PRJ.446932

C. Pérez-Armenta, A. Ortega-Moñux, J. M. Luque-González, R. Halir, J. Schmid, P. Cheben, I. Molina-Fernández, and J. G. Wangüemert-Pérez, "Polarization insensitive metamaterial engineered multimode interference coupler in a 220 nm silicon-on-insulator platform," *Optics & Laser Technology*, vol. 164, p. 109 493, Apr. 2023. DOI: 10.1016/j.optlastec.2023.109493

Abstract: High-index contrast silicon waveguides exhibit strong birefringence that hinders the development of polarization-insensitive devices, especially for sub-micrometer silicon layer thickness. Here a polarization-independent 2 × 2 multimode interference coupler in a 220 nm silicon-on-insulator platform is designed and experimentally demonstrated for the first time. Leveraging the advanced control of electromagnetic properties provided by a subwavelength grating metamaterial topology, our multimode interference coupler operates for both TE and TM polarization states with measured polarization dependent loss, insertion loss and imbalance all less than 1 dB, and phase errors below 5° in the wavelength range from 1500 nm to 1560 nm. The device has a footprint of only 3.5 μm × 47.25 μm and was fabricated using a single etch-step process with a minimum feature size of 100 nm compatible with immersion deep-UV lithography.

Journal: Optics & Laser Technology

Published: April 25, 2023

URL: https://doi.org/10.1016/j.optlastec.2023.109493

C. Pérez-Armenta, K. K. MacKay, A. Hadij-ElHouati, A. Ortega-Moñux, I. Molina-Fernández, J. G. Wangüemert-Pérez, J. H. Schmid, P. Cheben, and W. N. Ye, "Thermally induced sideband generation in silicon-on-insulator cladding modulated bragg notch filters," *Opt. Express*, vol. 31, no. 13, pp. 22 225–22 232, Jun. 2023. DOI: 10.1364/OE.488108

Abstract: We investigate and experimentally demonstrate a cladding modulated Bragg grating superstructure as a dynamically tunable and reconfigurable multi-wavelength notch filter. A non-uniform heater element was implemented to periodically modulate the effective index of the grating. The Bragg grating bandwidth is controlled by judiciously positioning loading segments away from the waveguide core, resulting in a formation of periodically spaced reflection sidebands. The thermal modulation of a periodically configured heater elements modifies the waveguide effective index, where an applied current controls the number and intensity of the secondary peaks. The device was designed to operate in TM polarization near the central wavelength of 1550 nm and was fabricated on a 220-nm silicon-on-insulator platform, using titanium-tungsten heating elements and aluminum interconnects. We experimentally demonstrate that the Bragg grating self-coupling coefficient can be effectively controlled in a range from 7 mm^{-1} to 110 mm^{-1} by thermal tuning, with a measured bandgap and sideband separation of 1 nm and 3 nm, respectively. The experimental results are in excellent agreement with simulations.

Journal: Optics Express

Published: June 16, 2023

URL: https://doi.org/10.1364/OE.488108

Chapter 3

Inverse design of an ultra-short spot-size converter using SWG metamaterials

In this chapter a novel methodology for photonic inverse design is introduced. This methodology leverages subwavelength metamaterials to design an ultra-short and broadband spot-size converter (SSC) for TE polarization in a 220 nm-thick SOI platform. This work has been developed in the context of the national research project "Smart inverse design for advanced integrated photonics using subwavelength metamaterials" (METAPHOR) funded by the Spanish Ministry of Science and Innovation and will be continued in another doctoral thesis.

3.1 Introduction

Photonic inverse design has gained significant attention in recent years due the increasing availability of high performance computing systems. This has facilitated the automatic design of very compact devices with state-of-the-art capabilities [108]. The user provides the optimization algorithm with an objective function to optimize, design variables that parametrize a generic photonic structure, and initialization and bounds for these variables. As the objective function is either maximized or minimized, the device behavior approaches the target performance. The process finishes with a synthesized device geometry that satisfies targets set at the beginning.

It is crucial to choose an algorithm suited to the specific problem being treated. Gradient-based methods such as the gradient-descent method [109] or the method of

moving asymptotes [110] are appropiated when a good initial solution is known, as the ones given by analytical models. Under certain conditions, these methods guarantee convergence of the optimization process. However, they are susceptible to converging to a local optimum rather than a global one. Additionally, in many photonic design problems the gradient of the objective function is unknown and must be estimated through finite differences. Gradient-based methods scale poorly with the number of variables in such cases. For a black-box problem with N design variables, $N + 1$ simulations are needed to calculate the objective function and estimate its partial derivatives with respect to each variable. Since full-vectorial 3D electromagnetic simulations are time-consuming, optimization time can become prohibitive.

The adjoint method [111] enables gradient calculations using information from only two simulations. Two formulations of the adjoint method are used in photonic design: shape optimization [112], in which waveguide walls are varied and thus is more limited; and topology optimization, where a dielectric region is divided into pixels of continuosly varying permittivity [113]. Although the last case is more versatile, additional processing is required for the structure to be manufacturable. Specifically, the continuosly varying material must be mapped to a binary medium (in the case of SOI, the only mediums available are Si and SiO_2) and features must be smoothened to ensure minimum feature size compliance [114].

On the other hand, global optimization algorithms operate without needing gradient information, relying instead on heuristics or evolutionary techniques where convergence is not assured. While these algorithms may be slower than gradient-based ones, their exploratory nature makes them less prone to get trapped in local optima. Genetic Algorithms (GA) [115] are classical gradient-less algorithms applicable to discrete-defined problems like pixelated metasurfaces [116] as well as to continuous variable problems such as surface grating couplers with complex periodic structures [117]. Particle Swarm Optimization (PSO), under certain conditions and with the proper configuration may outperform GA [108, 118], finding use in the design of polarization beam splitters [119, 120], photonic crystal transitions [121] and power splitters [122], to name a few. It is not clear though how to configure some of these algorithm parameters like particle speed or inertia. The Covariance Matrix Adaptation Evolution Strategy (CMA-ES) [123] emerges as an interesting alternative, requiring less configuration parameters (only the population size) and demonstrating suitability in electromagnetic problems. Devices designed using CMA-ES include efficient grating couplers [124], photonic crystal cavities [125], low-loss S-bends [126] and broadband bent directional couplers [127]. Other global optimization techniques not covered here like ant colony optimization, simulated annealing or surrogate modelling, along with machine learning approaches are explored in the literature [108, 128].

Spot-Size Converters (SSCs) are essential components required to adapt waveguides

with different widths, particularly when connecting interconnection waveguides (typically hundreds of nanometers wide) and devices made of few microns wide-waveguides such as surface grating couplers [19, 21, 117], reflectors [129], splitters [130] and low-loss crossings [131]. In recent years, implementations of very short SSCs have been proposed using both forward and inverse design approaches. Luque-González et al. [132] used modulated SWGs on a 220-nm thick SOI platform to implement a 14 μm-long on-chip graded-index lens adapting 500 nm to 15 μm with measured insertion losses below 1 dB in a bandwith of more than 130 nm. Zhang et al. [133] demonstrated a 11.2 μm-long Luneburg lens creating a SWG metamaterial with a two-step etch process, achieving a measured bandwith of 220 nm with insertion losses around 1 dB. Xu et al. [134] achieved 0.15 dB in a 100 nm bandwidth using a parabolic mirror with a footprint of $20 \times 32\,\mu m^2$.

The aforementioned implementations were designed using a forward approach. In the area of inverse design, Zou et al. [135] demonstrated a variable width transition with a 45 nm bandwidth where insertion losses were below 0.7 dB in a length of 20 μm. More recently, Cheng et al. [136] and Ma et al. [137] employed topology optimization via the adjoint method to design very short transitions (1 to 18 μm in 10 μm and 500 nm to 10 μm in 8 μm, respectively). Notably, [137] used a subwavelength metamaterial as inizialization, subsequently enhanced by topology optimization.

It is noteworthy that many of the state-of-the-art SSCs cited previously leverage SWGs as a solution. Therefore, there is significant interest in exploring the combination of SWGs with inverse design methods. Recently, Guo et al. [47] utilized a shape-varying approach combined with intermediate sections of a previously fixed SWG metamaterial. However, the geometry of the SWG or the equivalent material was not optimized. Thus, there is room for improvement in SWG-based optimization methods.

The goal of the this work is to develop a new inverse design method empowered by SWGs, leveraging the extensive knowhow of the research group in subwavelength engineering. As a test case, a state-of-the-art ultra-short SSC is designed. The optimization framework developed here has been deployed in the supercomputing infrastructure of the University of Málaga. Test structures have been designed and sent to foundry. Its experimental characterization is currently undergoing work in the framework of another doctoral thesis. An introduction to the topic and a the state of the art has been provided in this section. The inverse design problem is presented in sec. 3.2. The proposed methodology is developed in sec. 3.3, along with the models and computational framework developed. Simulation and preliminary experimental results are presented in sec. 3.4 and sec. 3.5, respectively. Finally, conclusions are drawn in sec. 3.6.

3.2 Inverse design problem definition

The goal of the work is to design a broadband integrated SSC with a small footprint. The device must adapt the fundamental TE modes (x-polarized electric field) of a narrow waveguide with width $w_{\text{in}} = 500\,\text{nm}$ and a wide waveguide with width $w_{\text{out}} = 12\,\mu\text{m}$. The structure is built on a SOI platform with a silicon layer thickness of $h = 220\,\text{nm}$.

The parametrized geometry of the spot-size converter is presented in Fig. 3.1(a). This configuration comprises a 5×5 matrix of SWG sections with a fixed period $\Lambda = 200$ nm and a variable duty cycle $\text{DC}_{i,j}$. The in-plane shape of the sections is controlled by the transversal distances $d_{i,j}$ and a fixed section length in the propagation direction L_{s}. An additional transition of fixed length L_{t}, final width w_0 and SWG duty cycle DC_0 is placed between the input waveguide and the metamaterial matrix to reduce mismatching losses. Its duty cycle and final width are also treated as optimization variables. Given that the structure is symmetric with respect to the yz plane, only 3×6 transversal distances and 3×5 metamaterials have to be designed.

An objective or score function must be defined so the optimizer can automatically design the device. The device must adapt the fundamental TE modes of the narrow and wide waveguides across the broadest possible bandwidth. Hence, a simple objective function can be used such us

$$f(\mathbf{g}) = \frac{1}{\lambda_2 - \lambda_1} \int_{\lambda_1}^{\lambda_2} -10 \log_{10} |S_{21}(\lambda, \mathbf{g})|^2 \mathrm{d}\lambda \tag{3.1}$$

where $\mathbf{g} = \left\{w_0, [d_{i,j}], \text{DC}_0, [\text{DC}_{i,j}]\right\}$ is a vector encompassing all the design variables and S_{21} is the S-parameter characterizing the transmission from the fundamental TE mode of the narrow input (port 1) to the fundamental mode of the wide output (port 2). Thus, f represents the insertion losses of the device averaged over the wavelength range between λ_1 and λ_2. The optimization objective is to find a combination of parameters $\mathbf{g}_{\text{opt}}$ that minimizes f

$$\mathbf{g}_{\text{opt}} = \underset{\mathbf{g}}{\text{argmin}}\, f(\mathbf{g}). \tag{3.2}$$

3.3 Methodology and computational framework

In this section the methods and computational techniques employed in this work are detailed. A 2D anisotropic model for SWGs is presented in Sec. 3.3.1. The optimization algorithm used in the inverse design method is reviewed in Sec. 3.3.2. The interface between the optimizer and the supercomputer Picasso is summarized in Sec. 3.3.3. Finally, the inverse design procedure is proposed in Sec. 3.3.4.

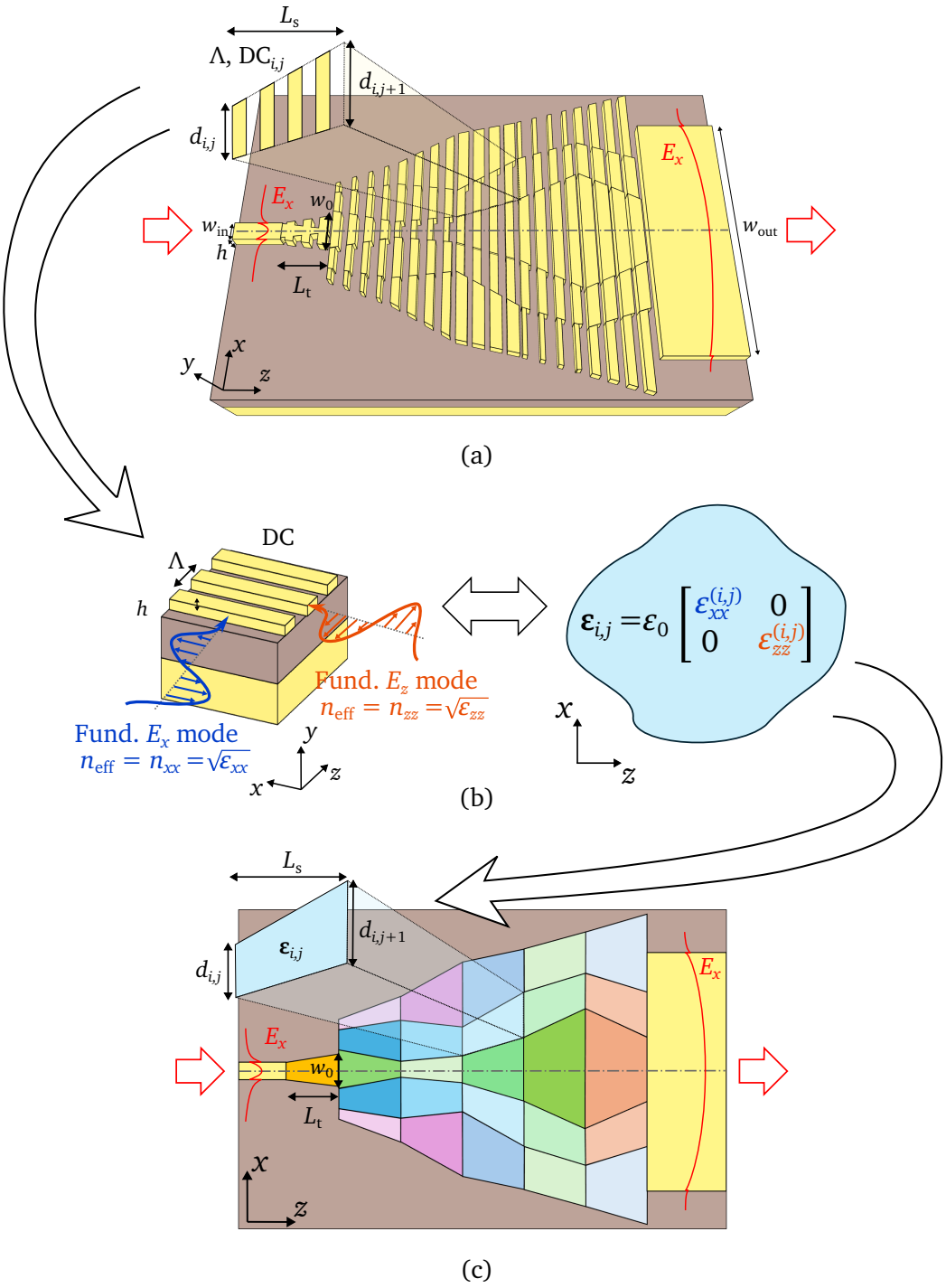

Figure 3.1 (a) Definition of the parametrized geometry of the spot size converter (SSC) using SWG sections. The device must adapt the fundamental TE mode of two waveguides of width w_{in} and w_{out}. (b) Effective anisotropic 2D modelling of SWG metamaterials. (c) The resulting equivalent medium is introduced in its corresponding section in a planarized version of the SSC.

3.3.1 Effective anisotropic 2D medium modelling

In order to accelerate the design of the device using the method described in this chapter, an approximate 2D model has been employed. This technique, similar to the Effective Index Method [138], has been previously applied with success in other works such as the design of an ultra-broadband integrated beam-splitter by Halir et al.[43] and the design of polarization insensitive MMI coupler, which is a contribution of this thesis [63].

Any SWG section (i, j) of the SSC is modelled as an anisotropic 2D medium. The process to obtain the equivalent material is depicted in Fig. 3.1(b). A given SWG is introduced in a Bloch-Floquet mode solver such as MPB [102]. This structure extends indefinitely on the x direction and is periodic in the propagation direction z. Solving for in-plane polarized fundamental modes propagating in the x and z directions at the central operating wavelength give the components of the equivalent permittivity tensor $\varepsilon_{i,j}$. The following steps are followed to calculate them:

1. Set the propagation direction to z.
2. Solve for the fundamental mode with x-polarized electric field. The effective index obtained is $n_{\text{eff}} = n_{xx}$.
3. Set the propagation direction to x.
4. Solve for the fundamental mode with z-polarized electric field. The effective index obtained is $n_{\text{eff}} = n_{zz}$.
5. The equivalent permitivity tensor of the SWG metamaterial (i, j) is

$$\boldsymbol{\varepsilon}_{\text{eff}} = \varepsilon_0 \begin{bmatrix} \varepsilon_{xx}^{(i,j)} & 0 \\ 0 & \varepsilon_{zz}^{(i,j)} \end{bmatrix} = \varepsilon_0 \begin{bmatrix} \left(n_{xx}^{(i,j)}\right)^2 & 0 \\ 0 & \left(n_{zz}^{(i,j)}\right)^2 \end{bmatrix}. \tag{3.3}$$

The propagation of a TE mode in the modelled SWG grating is modelled by propagating an x-polarized wave in the resulting metamaterial. Therefore, the SSC of Fig. 3.1(a) can be converted into the 2D version shown in Fig. 3.1(c). Since the design targets x-polarized light, the equivalent 2D SSC input must be excited with the fundamental TM mode of the input slab waveguide. Note that it is not necessary to calculate the ε_{yy} component as it does not affect the propagation of TM waves in anisotropic slab waveguides [139].

3.3.2 Optimization algorithm: CMA-ES

The optimization algorithm utilized in this work is the Covariance Matrix Adaption Evolution Strategy (CMA-ES). It is an stochastic optimization method for continuous real-valued problems that are non-linear and non-convex [123, 140].

The algorithm runs in a loop for which in each iteration or generation i a population of individuals of size p is generated from a multi-variate normal distribution with mean

$\mathbf{m}^{(i)}$, covariance matrix $\mathbf{C}^{(i)}$ and a adustable step-size $\sigma^{(i)}$. Formally, each candidate in a generation $\mathbf{x}_k^{(i)}$

$$\mathbf{x}_k^{(i)} \sim \mathcal{N}_p(\mathbf{m}^{(i)}, \sigma^{(i)}\mathbf{C}^{(i)}) \qquad k = 1, 2, \ldots, p. \tag{3.4}$$

Each candidate correspond to a certain problem geometry $\mathbf{g}$, which is introduced in the electromagentic solver to evaluate the objective function $f(\mathbf{g})$. After all the candidates have been evaluated, the algorithm calculates $\mathbf{m}^{(i+1)}$, $\mathbf{C}^{(i+1)}$ and $\sigma^{(i+1)}$. Details on how these parameters are updated can be found in [140].

In this work, initialization is done by giving a guess as the first mean vector $\mathbf{m}^0$ and a population size of $p = 10$. Other parameters are set to their defaults as encouraged by [140].

3.3.3 Deployment on supercomputing facilities

The optimization processes and all the electromagnetic simulations required by them have been launched in the University of Malaga's supercomputer Picasso [141]. An additional software layer have been implemented to integrate the optimization algorithm, FDTD simulations powered by Meep [104] and the Slurm queueing system [142] installed in Picasso.

The implemented architecture is outlined in Fig. 3.2. The main script is the starting point of the process and is the one called by the user. It is responsible of initializing the directory structure of the optimization project. Then it submits a job to the queueing system that will run the optimizer.

The optimizer job is run once for every generation of the algorithm. When the optimizer job starts, it checks if it has been lauched before by checking existing status and history files. In the first execution, no data is found in the optimization project directory, so an optimizer instance is created using the Python library Nevergrad [143]. The optimizer is provided with an initial guess given by the user and the score function. Then, the optimizer is asked for a set of candidates of size equal to the population configured in the algorithm. The design variables of each candidate is stored in the project along with the optimizer instance for future use. Afterwards, for each candidate a simulation job is submitted to the system and the optimizer job is re-submitted with the simulation jobs being a dependency. In other words, the optimizer will be launched again after succesfull finalization of all the simulations. The optimizer job ends here but the optimization process continues.

Each simulation job has associated one of the candidates asked to the optimizer. Once started, they load the corresponding stored design variables and launch the simulation in Meep. After finishing the simulation, the S-parameters are calculated and saved in the project. After all the simulations have been finished, the previously self-submitted optimizer is allowed to run.

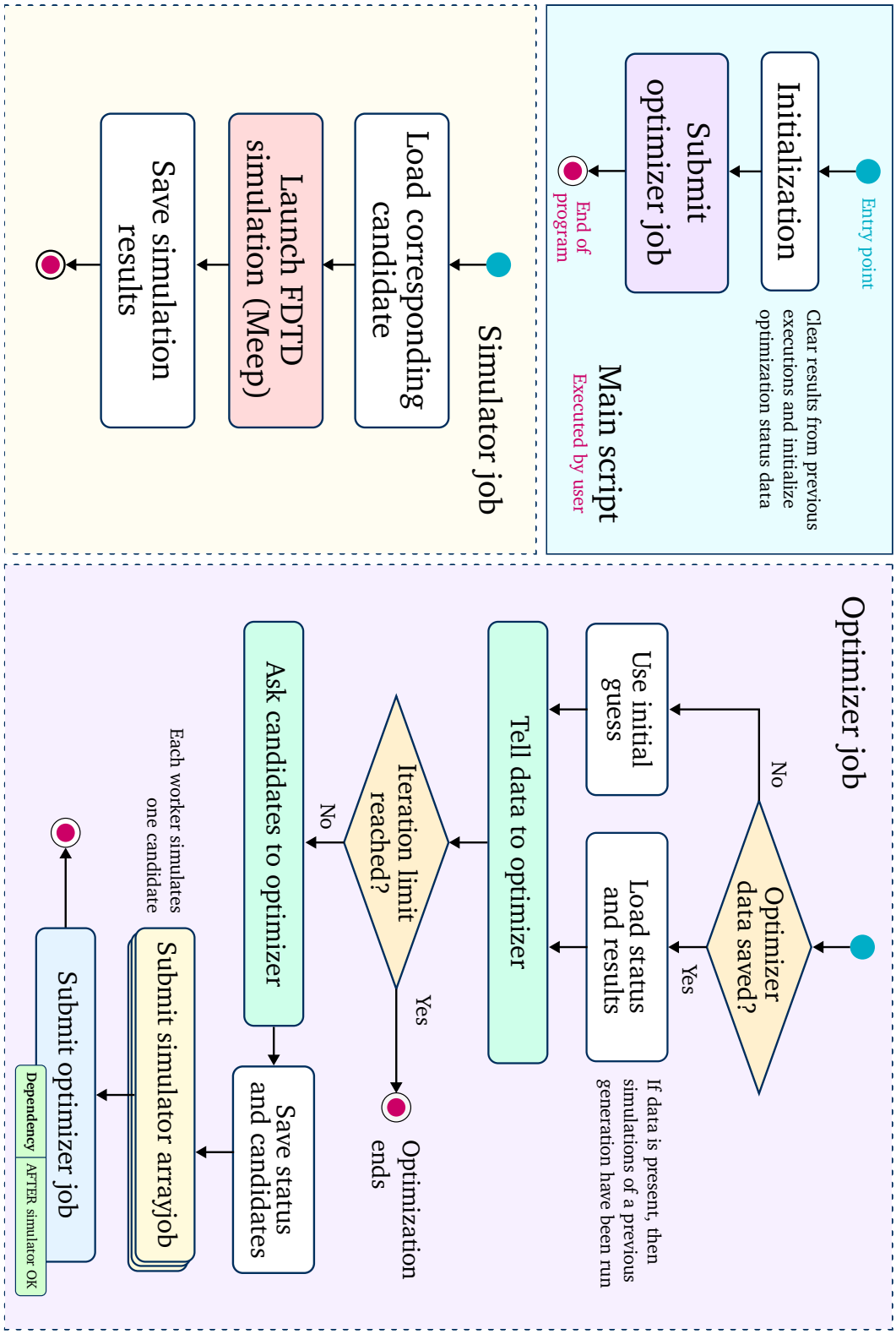

Figure 3.2 Optimizer architecture for Picasso's supercomputer.

Once the queueing system starts the optimizer job, it looks for existing data of optimizer status and simulations results. If data is found, the optimizer is loaded and updated with the results of the candidates. The process is repeated until a maximum number of iterations is reached or the user interrupts the process. After that, the user has access to the best candidate variables for further processing.

The advantages of using this architecture are the following:

- The supercomputer counts with virtually unlimited memory (although shared with other users) which enables simulation parallelization in each generation of the optimization algorithm.
- The open-source simulator Meep is free of restrictions on the number of simulation instances running like in other commercial solvers.
- By saving and loading the optimizer in different executions, computing resources are used more efficiently compared to a single optimizer job running for the whole process and waiting for the simulations to finish by polling.

3.3.4 Inverse design procedure

The inverse design starts with the 2D version of the SSC [Fig. 3.1(c)]. In order to optimize this structure, the set of valid anisotropic materials must be defined. This is done by performing the simulation depicted in Fig. 3.1(b) for fabricable duty cycles with EBL, i.e., for minimum feature sizes greater than 60 nm. For $\Lambda = 200$ nm, manufacturable DCs range from 30 to 70 %. The results are stored in a Look-Up Table (LUT) that maps a given DC to a anisotropic material $\boldsymbol{\varepsilon}(\mathrm{DC})$.

Once the LUT has been created, the process outlined in Fig. 3.3 is followed. The design variables are first initialized by the user. An initial generation is sampled and the generated $\mathrm{DC}_{i,j}$ are converted to anisotropic materials $\boldsymbol{\varepsilon}_{i,j}$. These materials along with the transversal distances and the initial width are passed to the FDTD simulator Meep, from which the S-parameters of the device are obtained. The S_{21} parameter is used to compute the score function for each candidate in the generation. The process is repeated for a maximum number of iterations or when the optimization converges to a minimum of f, corresponding to the best candidate $\mathbf{g}_{\text{best 2D}}$.

The best candidate is used as the initial guess of a new stage. The optimization process is run again, now simulating the actual 3D periodic structure without having to apply the LUT to the DCs. The optimization process concludes with the final design of the SSC. As will be seen in the next section, the preliminary 2D optimization quickly provides a good initial guess for the 3D stage that allows to save computation time.

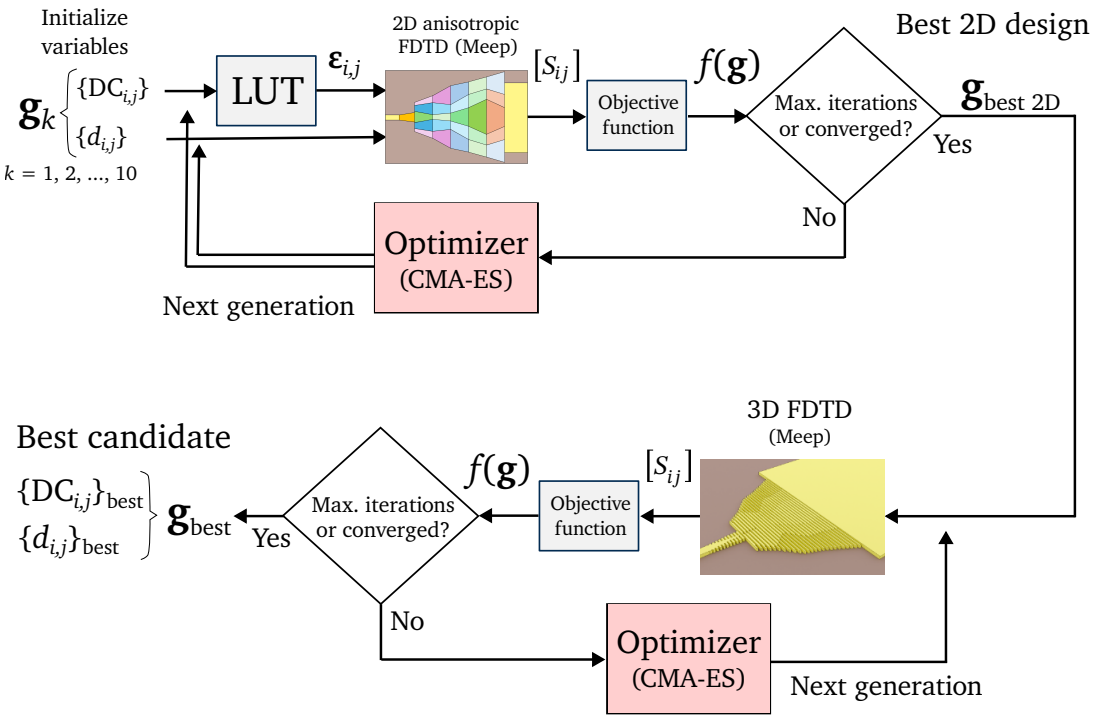

Figure 3.3 Optimization procedure proposed in this work.

3.4 Design and simulation results

The periodic structure pitch was set to $\Lambda = 200$ nm and the section length to $L_s = 1\,\mu$m so 5 periods fit in each section. By using MPB [102] a LUT was generated for $\lambda = 1550$nm and duty cycles ranging 30 to 70 %, which ensures a minimum feature size of 60 nm compatible with EBL. The contents of the LUT are shown in Fig. 3.4. The metamaterial matrix was initialized in a GRIN-like manner, a strategy previously proven effective for on-chip beam collimation [28]. Concretely, $n_{xx}^{(1,j)} = 2.4$, $n_{xx}^{(2,j)} = 2.2$ and $n_{xx}^{(3,j)} = 2.0$ were used, the corresponding DC and n_{zz} can be obtained from Fig. 3.4. The distance variables were set so the structure constitutes a linear taper from $w_{\text{in}} = 500\,\text{nm}$ to $w_{\text{out}} = 12\,\mu$m. The initial transition is initialized to $n_{xx}^{(\text{ini})} = 2.4$ and $w_0 = 500\,\text{nm}$, with a fixed length of $L_t = 2\,\mu$m. The input and output waveguide refractive index is $n = 2.84$, as a result of applying the effective index method to a 220 nm-thick SOI slab at $\lambda = 1550\,\text{nm}$ for TE polarization. The initialized structure is shown in Fig. 3.5.

The optimizer was executed for a maximum of 1000 generations in the 2D stage, achieving averaged insertion losses of less than 0.2 dB. This quantity was obtained evaluating Eq. (3.1) for $\lambda_1 = 1.5\,\mu$m and $\lambda_2 = 1.6\,\mu$m. The best candidate served as initial guess of the 3D stage, which continued for an aditional 100 generations. As shown in Fig. 3.6(a), the best result of the 2D process made the optimizer start from a score of 1 dB. It is worth noting that while the average simulation time was 1.5 min for the 2D simulations, 3D simulations lasted 1.2 h. As demonstrated in Fig. 3.6(b), the two stage

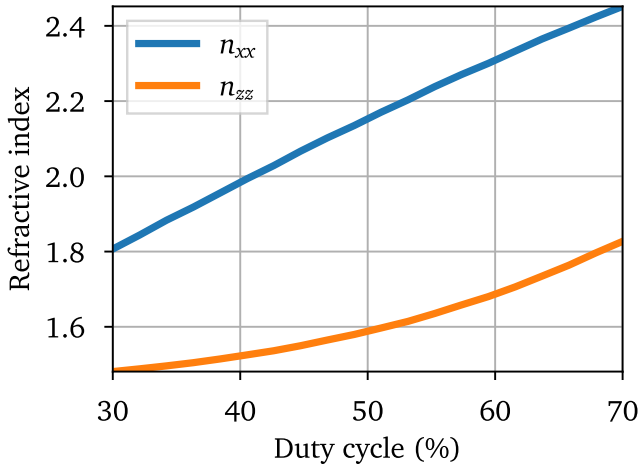

Figure 3.4 Calculated look-up table (LUT) for a SOI SWG waveguide with period $\Lambda = 200\,\text{nm}$ and thickness $h = 220\,\text{nm}$ in refractive index units. The electric permittivity tensor can be obtained by squaring each component. Details on the method to generate the LUT can be found in sec. 3.3.1.

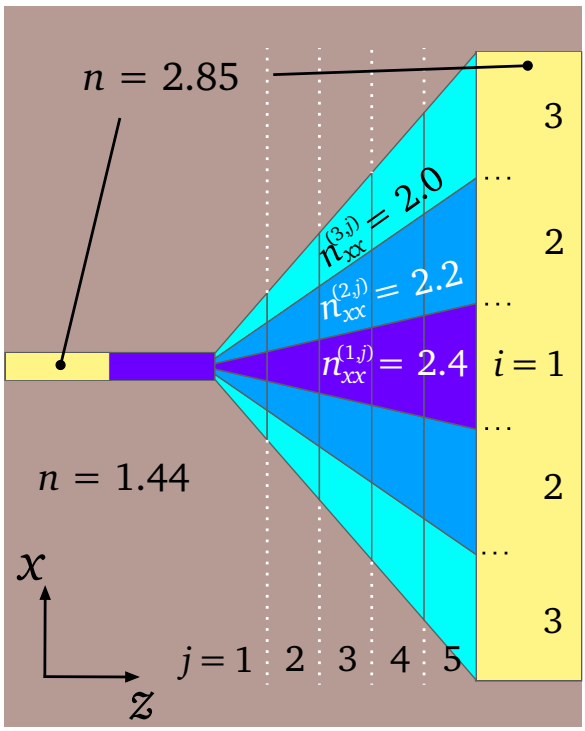

Figure 3.5 Inital guess for the optimization process using the anisotropic 2D model.

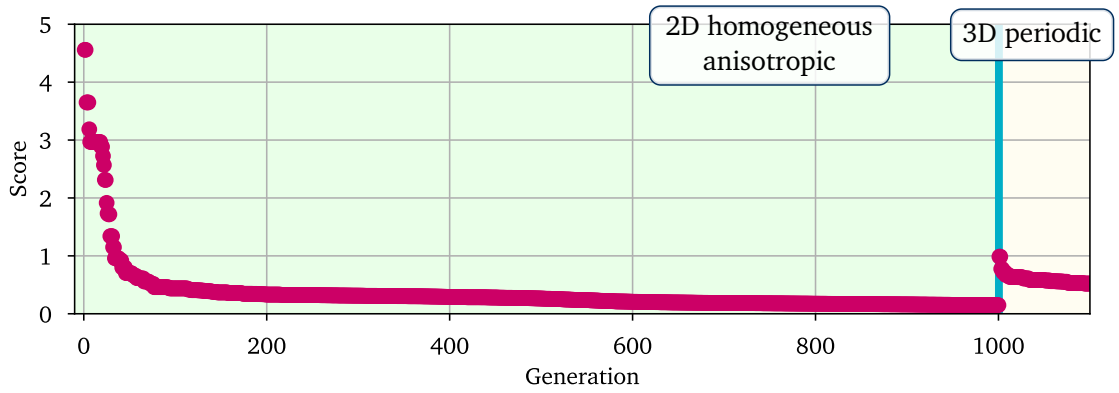

(a)

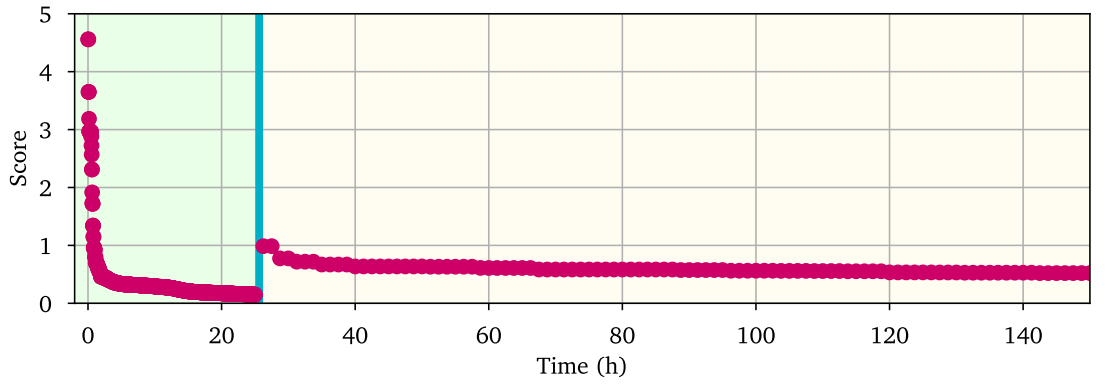

(b)

Figure 3.6 Optimization history. (a) Each point represent the score function $f(\mathrm{v})$ of the best candidate of each generation. The simulation model is switched from a 2D problem with homogeneous anisotropic materials to a 3D one using SWGs on the 1000$^{\text{th}}$ generation. (b) The same history plotted against the time at which generation finished simulating. This visualization highlights the effectiveness of the preliminary 2D optimization in accelerating the design of the SSC.

approach is crucial for accelerating the convergence of the optimization process.

The 3D optimization process converged to an average insertion loss of 0.5 dB. The geometry of the best design is shown in Fig. 3.7. Fig. 3.8(a) shows the x-component of the electric field when the narrow waveguide is excited with a continuous wave source with $\lambda = 1550\,\text{nm}$ injecting the fundamental TE mode. A broadband simulation ranging wavelengths from 1.4 to 1.7 μm was performed to check the performance of the device. As illustrated in Fig. 3.8(b), the device exhibits insertion losses below 0.8 dB in a 300 nm bandwith and a reflectivity below -12 dB. A comparison of the device's performance with other SSCs is presented in Table 3.1, demonstrating state-of-the-art metrics while having the shortest device length.

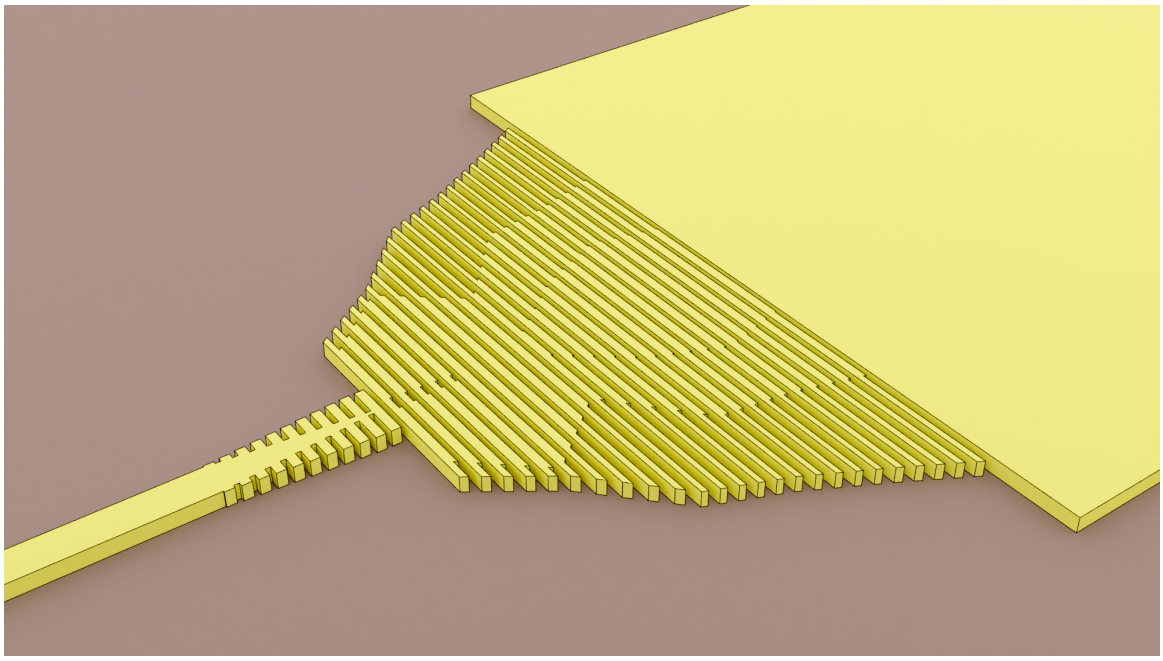

Figure 3.7 Final design of the spot size converter.

	w_{in} (µm)	w_{out} (µm)	L (µm)	IL_{sim} (dB)	BW_{sim} (nm)	IL_{exp} (dB)	BW_{exp} (nm)
[135]	0.5	12	20	< 0.5	> 60	< 0.7	> 45
[132]	0.5	15	14	< 1	> 350	< 1	> 130
[136]	1	18	10	< 1	50	(*)	(*)
[133]	0.5	10	11.2	< 1	740	< 1.5	220
[137]	0.5	10	8	< 1	100	1	100
[134]	0.45	10	32(**)	< 0.2	200	0.15	100
This work	0.5	12	7	< 0.8	300	< 0.75	150

(*) Measurements presented 1 dB ripple.

(**) The total footprint of the beam expansor is 20 µm × 32 µm.

Table 3.1 Comparison of the designed SSC performance with other state-of-the-art devices.

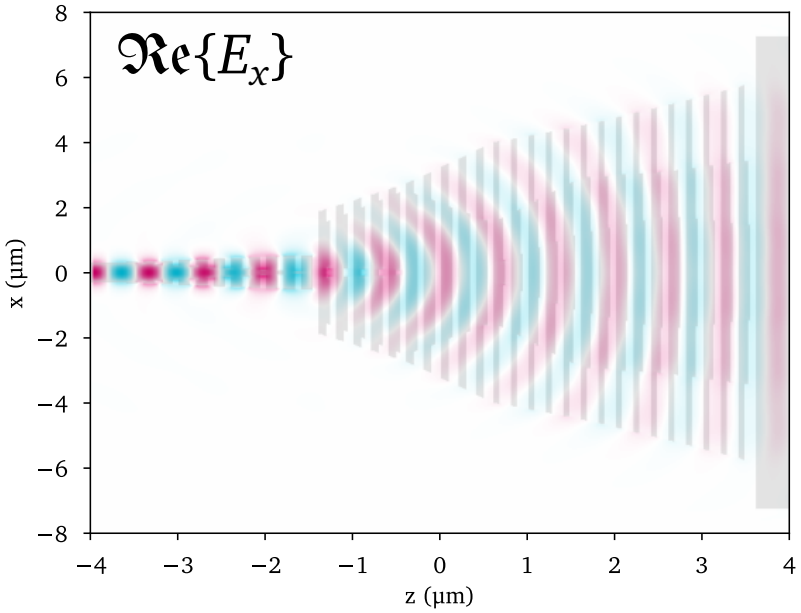

(a)

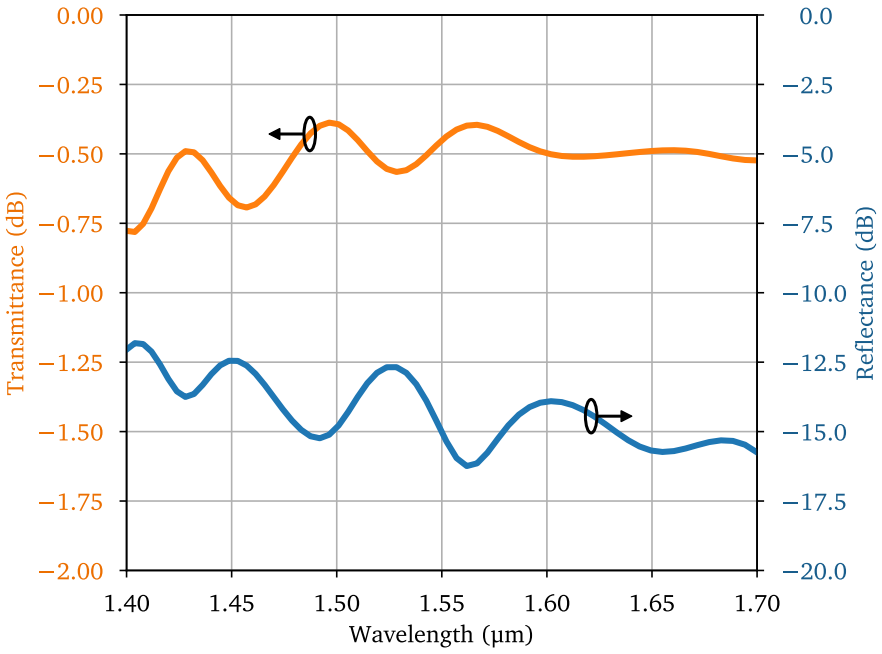

(b)

Figure 3.8 Simulation results of the inversely designed SSC: (a) electric field propagation at $\lambda = 1550\,\text{nm}$ when excitating with the fundamental mode of the narrow waveguide. (b) Transmittance (orange, left axis) and reflectance (blue, right axis) of the device.

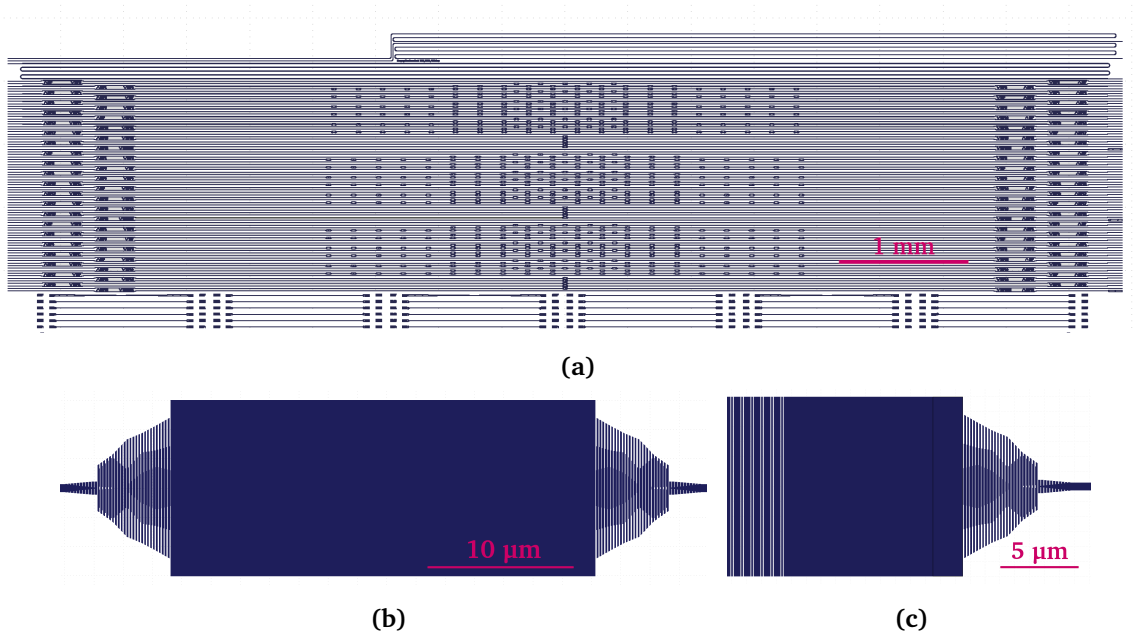

Figure 3.9 Layout submitted to a silicon photonics foundry: (a) full layout, (b) close view of two SSCs in back to back configuration and (c) close view of an SSC connected to a surface grating coupler.

3.5 Experimental characterization: preliminary results

At the moment of writing this thesis, the experimental demonstration of the designed SSC is ongoing work. This section presents some preliminary results of the characterization of the device.

The layout shown in Fig. 3.9(a) was submitted to an external foundry for its manufacturing in a 220-nm thick SOI platform. Two kinds of test structure have been included. One involves cascading of various structures consisting of two SSCs in a back to back configuration [Fig. 3.9(b)]. On the other hand, SSCs connected to 12 µm-wide surface grating couplers have also been included [Fig. 3.9(c)]. Variations of the nominal design to compensate for over-etching and under-etching errors were included. This is controlled by the δ parameter, defined in Fig. 3.10. A positive δ makes each silicon strip larger in the directions contained in the chip plane. In addition, another design optimized for the situation when the oxide cladding does not completely fill the space between SWG silicon strips was included. To obtain this device, the optimization process was relaunched assuming 60 nm air gaps [43].

In the same way as in the experimental work of Chapter 2, the submitted layout has been fabricated on a SOI platform with a 220 nm-thick silicon layer and a 2 µm-thick buried oxide. The devices have been patterned using electron beam lithography and etched via anisotropic inductively coupled plasma reactive ion etching. A 2.2 µm oxide cladding has been deposited using plasma-enhanced chemical vapour deposition. Fig.

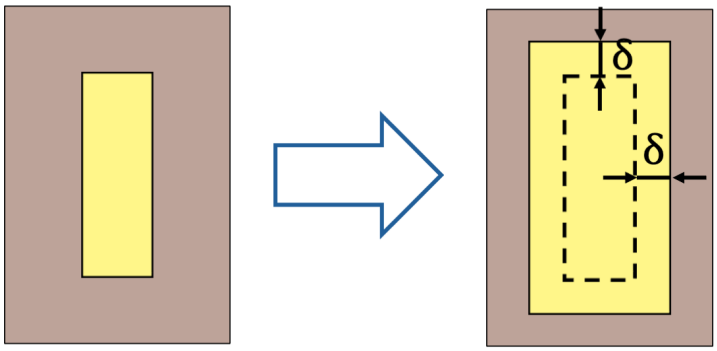

Figure 3.10 Over-etching and under-etching error compensation definition.

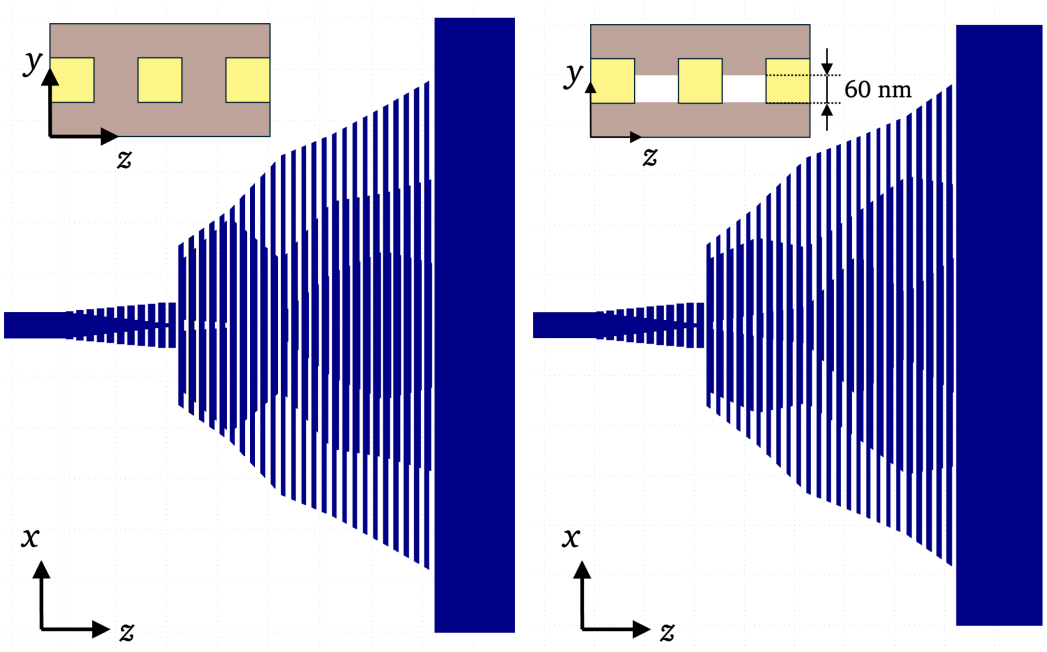

(a) Design 1. **(b)** Design 2.

Figure 3.11 Two designs were tested in the chip each with over-etching and under-etching compensation flavors: (a) it is assumed that the space between SWG strips are completely filled with the $SiO_2$and (b) 60 nm-thick air gaps are present between each silicon strip.

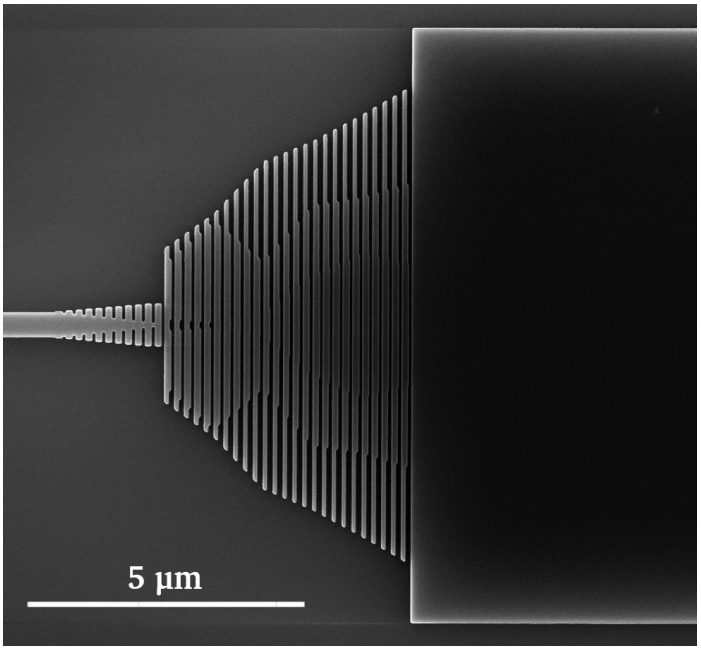

Figure 3.12 SEM image of a fabricated spot-size converter corresponding to the nominal design 1.

3.12 shows an SEM image of the nominal design.

To measure[1] the insertion losses of the device, linearly polarized light from a tunable laser source (TLS) is coupled to the chip using a lensed fiber and broadband polarization independent SWG edge couplers [35]. The polarization state is selected using a fiber polarization controller. On the chip the light is guided to test structures with different number of SSCs connected back to back. Outputs are routed to SWG edge couplers in the other facet of the chip. The light exiting the chip is collimated by a microscope objective, filtered by a Glan-Thompson polarizer and intercepted by a germanium photodetector.

By measuring test structures with different number of concatenated SSCs, their insertion losses can be inferred through the cut-back method in combination with the minimum phase technique [144]. Fig. 3.13 shows the raw power measurement of the best test structures comprising a different number N_{b2b} of concatenated back-to-back SSCs [Fig. 3.9(b)] and different etching errors δ for both designs in Fig. 3.11 along with a reference waveguide.

The designed devices present non-zero reflection coefficients at both ports, thus forming cavities when cascading copies of them. The wide waveguide between back-to-back SSCs is 25 µm-long and the length of the narrow waveguides interconnecting two back-to-back structures is 150 µm. These lengths have been chosen so two interferogram patterns with different periodicities are created and enough periods fit in the measurement range. The minimum phase technique converts the measured transmis-

[1]The author thankfully acknowledges Alejandro Sánchez Sánchez for carrying out the experimental characterization and data post-processing.

sion spectrum to a time-domain signal. By removing the echoes corresponding to the reflections between test devices and transforming it back to the frequency domain, a smooth transmission spectrum is obtained, which ideally corresponds to the $|S_{21}|^{2N_{b2b}}$ parameter of the SSC. Further information on the minimum phase technique can be found on Ref. [144].

For each wavelength of the TLS sweep, a linear regression with N_{b2b} is performed on the filtered transmission. From the slope of the resulting straight line the loss per device can be obtained. The insertion loss of each selected device is shown in Fig. 3.14. The device performance shows good agreement when the air gaps have been considered in the inverse design process. Furthermore, the tolerance of the device to fabrication deviations is considerably better in this situation. It is noteworthy that the automatic nature of the inverse design method eases the inclusion of the air gaps whereas in traditional methodologies would require more designer work time.

3.6 Conclusion

The presented method introduces a new approach for inverse design utilizing SWG structure. This method has been applied in the design of an ultra-short spot-size converter in a 220 nm-thick SOI platform. Leveraging a 2D anisotropic model of SWG metamaterials and supercomputing facilities, fast optimization is enabled. A preliminar experimental characterization reveals that the inclusion of air gaps between SWG strips is relevant for simulation-experiment agreement. Measurement of the remaining structures and for broader wavelength ranges is undergoing work and will be continued in another doctoral thesis. The results showcased herein underscore the potential of SWG-powered inverse design for obtaining high performance devices and open prospects for the development of new photonic design tools.

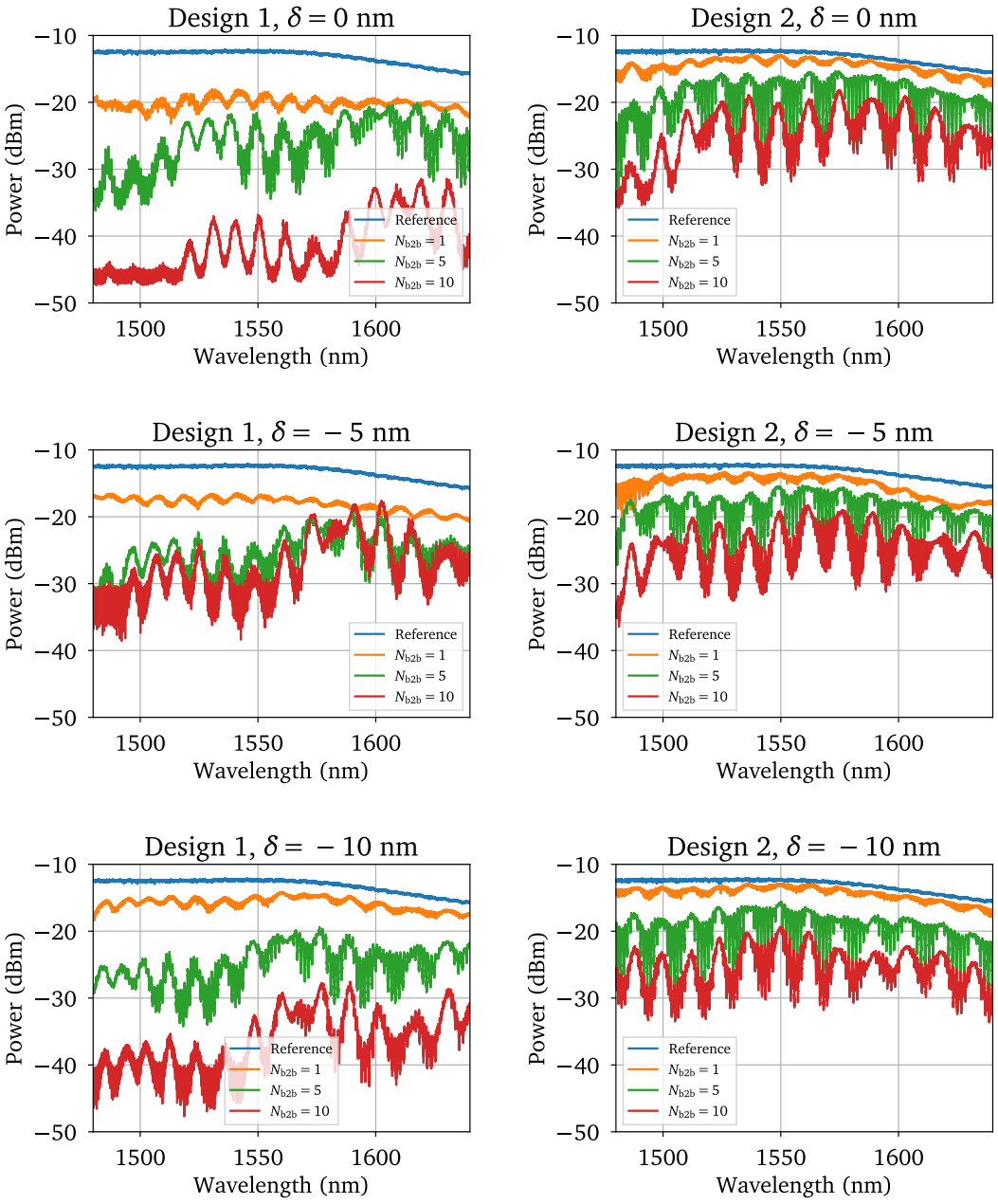

Figure 3.13 Raw power measurements of various test structures. N_{b2b} is the number of back to back structures and δ is the etching error compensation parameter. Design 1 assumes gaps completely filled with TSilica while Design 2 considers air gaps of 60 nm thickness.

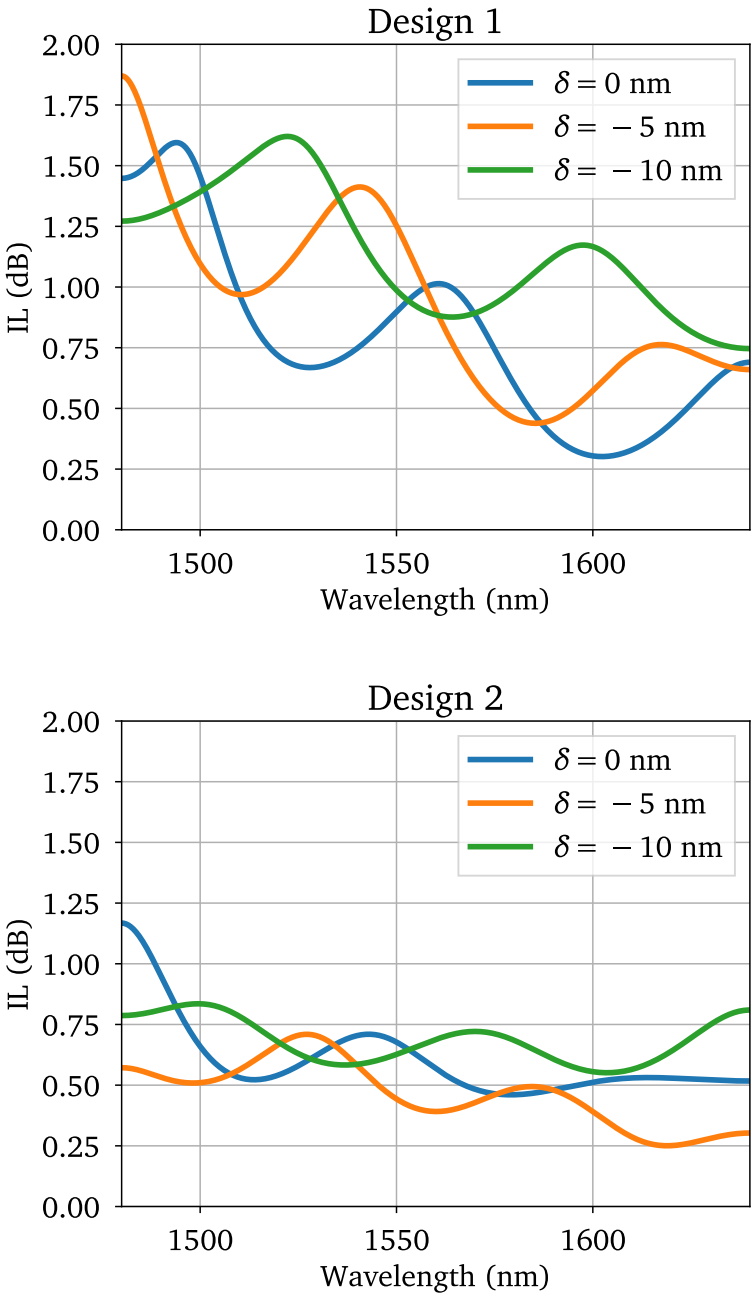

Figure 3.14 Intertion losses of different flavors of designs 1 (no air gaps considered) and 2 (air gaps considered in the design process) obtained from processing the data in Fig. 3.14.

Chapter 4

CONCLUSIONS AND PROSPECTS

This chapter summarizes the main conclusions and achievements of this thesis (sec. 4.1) and discusses ongoing work and future research lines related to the contributions presented (sec. 4.2).

4.1 Conclusions

Designing photonic devices making use of periodic structures has become an essential and powerful tool in silicon photonics and specifically on the SOI platform. Subwavelength gratings enable performance enhancements of photonic devices and also new functionalities without needing more complex fabrication processes that increase manufacturing expenses. In addition, weak Bragg gratings stand as an attractive solution to implement narrowband filters with applications in communications and sensing.

In this thesis, significant advances have been made in both SWG metamaterials and Bragg filtering fields. Enhanced modelling and simulation tools have been introduced. Novel SWG-topologies and design methods have been developed and applied to the following devices: *(i)* polarization insensitive MMI couplers, *(ii)* a Bragg refractive index sensor, *(iii)* a tunable Bragg filter and *(iv)* an ultra-short and ultra-broadband spot-size converter. Rigorous electromagnetic simulations have been conducted for all devices, and most have undergone experimental characterization. The findings from these contributions have been disseminated through publications in high-impact peer-reviewed journals and international conferences.

As a result of the research work carried out in this thesis, the following conclusions have been drawn.

The importance of modelling and the availability of efficient simulation tools

Simulating periodic structures can indeed demand significant computational resources, especially when using 3D full-vectorial FDTD methods. The Coupled Mode Theory model enables semi-analytic calculations of a Bragg filter wavelength response assisted by computing the Bragg key parameters of the filter's period (Bragg strength, refractive index and group index). This results in very fast and rigurous simulations as opposed to algorithms like FDTD whose simulation time would be impractical for long structures like weak Bragg gratings.

The utilization of 2D models in the preliminary design stage of the polarization insensitive MMI couplers (sec. 2.1.2) and the spot-size converter (chapter 3) has been proved to be crucial for quickly reaching an initial guess that reduce the total 3D computation time. In the case of the polarization independent MMI, the 2D model also provides physical insight on the anisotropic multimode imaging. The model facilitates understanding how the geometry affects the MMI behavior and finding candidate parameter combinations for the polarization independent regime. In the inverse design method presented in chapter 3, SWGs have been succesfully modelled as homogeneous anisotropic materials which eases shape definition in the method and is susceptible for being generalized to other SWG structures such as Bricked SWGs and for being used in more complex devices.

Polarization insensitivity can be achieved using advanced SWG topologies

SWGs have been proven in recent years to be an excellent way of controlling the optical properties of integrated optical devices. In this thesis, the novel bricked SWG topology has been investigated to achieve polarization independent behavior. 2×2 MMIs for the 220 nm-thick SOI platform have been designed and experimentally characterized. The methodology developed in these works can be readily generalized to MMIs with a higher number of ports, paving the way for polarization insensitive silicon photonic devices that are unattainable using conventional techniques.

The novel Bragg filter topology enable state-of-the-art resonant sensing

In the published work outlined in sec. 2.1.1, a high-performance refractive index sensor has been designed. The Bragg filter topology used possess high sensitivity provided by the guiding SWG and facilitates enhancement in the limit of detection by reducing the bandwidth without compromising the minimum feature size, as stated in the research hypothesis. Furthermore, the design methodology developed in this work takes into account propagation loss along the filter, setting a lower boundary for the filter bandwidth. It is shown that by reducing the target operational wavelength to 1310 nm instead of 1550 nm, the intrinsic LoD of the device can be improved an order of magnitud (i.e., a 10× reduction).

Tunable Bragg grating superstructures in SOI

As detailed in sec. 2.1.3, a proof of concept of Bragg superstructures has been succesfully carried out. This involves the design and characterization of a temperature-modulated Bragg filter in an SOI platform, demonstrating sideband amplitude tunability. The findings in this work open promising prospects for configurable wavelength division multiplexing and dispersion compensation in silicon photonics.

SWGs provide new possibilities in inverse design

In the work described in chapter 3, a new inverse design technique combining global optimization and subwavelength metamaterials has been developed. SWGs add more degrees of freedom as a continuous set of materials can be synthesized, thus not constricting the algorithm to just adjusting the shape of the device. In addition, inverse designed devices can benefit from the anisotropic properties of SWGs to enhance device performance. This has been the case of the spot size converter designed in this thesis, showing broadband adaptation in a very short distance.

4.2 Future prospects

The results of this thesis lay the groundwork for various potential research lines. Here we present a list of potential directions that can be further investigated.

Design and experimental demonstration of polarization insensitive devices

Besides MMI couplers a wide range of photonic devices could be designed using the bricked SWG or other topologies to avoid polarization dependence. This includes devices such as grating couplers, filters, crossings or more complex splitters.

Experimental demonstration of the Bragg sensor

The experimental characterization of the proposed Bragg sensor is still pending. In a recent work carried out in the University of Málaga's photonic research laboratory, fabricated Bragg filters presented disparity with the target spectrum [145]. A stochastic model was proposed to simulate fabrication errors by including them in a accumulated phase error term in the Bragg filter. Therefore, the sensor tolerance to phase errors should be studied prior to manufacturing.

Tunable filters with arbitrary spectrum

The spectrum of the configurable filter designed in this thesis is relatively simple, consisting only of a set of reflection peaks. Furthermore, the amplitudes of the different

peaks are not freely tunable. By designing a more complex heating layout, advanced photonic filters could be synthesized only by reconfiguring the temperature profile.

Experimental demonstration and generalization of inverse design methodology

The experimental characterization of the spot size converter is currently undergoing work. As of writing this thesis, a test chip has been fabricated and received at the research group facilities. Some preliminary measurements have been shown in sec. 3.5. Furthermore, following the working plan of the METAPHOR research project in which this work is framed, the proposed methodology will be extended to (a) other types of devices, such as polarization splitters and rotators, fiber couplers, and mode multiplexers; and (b) other SWG topologies.

Appendix A

Derivation of expressions for Bragg filters

In this appendix, derivations for some of the expressions used in the research articles in chapter 2 are given. Consider a mode propagating through an homogeneous dielectic waveguide

$$\mathbf{E} = a_m(z)\mathbf{E_0}^{(m)} e^{-j\beta_m z} \tag{A.1}$$

where $\mathbf{E_0}^{(m)}$ is the m-th mode electric field profile normalized for carrying time-averaged unit power, β_m is its propagation constant and $a_m(z)$ is its amplitude. When introducing a periodic perturbation in the refractive index profile of the waveguide, Coupled Mode Theory (CMT) [138] provides a framework for computing the power exchange between waveguide modes through couple mode equations. In general, the power exchange between guided modes traveling in opposite directions (contra-directional coupling) is given by

$$\pm\frac{\mathrm{d}a_l}{\mathrm{d}z} = -j\sum_{\nu}\kappa_{l\nu}(z)\; e^{j(\beta_l-\beta_\nu)z} a_\nu(z) \tag{A.2}$$

where $\kappa_{l\nu}$ is the coupling coefficient measuring the interaction between modes l and ν. It can be calculated through analytic formulae [138] or solving the band structure of the periodic waveguide [92]. Eq. (A.2) set the basis for the derivations that follow.

A Bragg filter is created by making a periodic perturbation in a waveguide. As such, the coupling coefficient will also be periodic and thus can be expanded in Fourier series

$$\kappa(z) = \sum_q \kappa_q e^{-jqK_\mathrm{B}z} \tag{A.3}$$

where $K_\mathrm{B} = 2\pi/\Lambda_\mathrm{B}$ is the grating constant and can be interpreted as the fundamental

spatial frequency of the perturbation. Introducing it in Eq. (A.2) leads to

$$\pm\frac{\mathrm{d}a_l}{\mathrm{d}z} = -j\sum_{\nu}\sum_{q}\kappa_{l\nu q}\, e^{j(\beta_l-\beta_\nu-qK_\mathrm{B})z}a_\nu(z). \tag{A.4}$$

Power exchange becomes significant when the exponent is close to 0,

$$\beta_l-\beta_\nu-qK_\mathrm{B}=0. \tag{A.5}$$

Eq. (A.5) is known as the Bragg condition. Then, assumming that the $q=q'$ component is the one satisfying it, Eq. (A.4) can be approximated as

$$\pm\frac{\mathrm{d}a_l}{\mathrm{d}z} = -j\kappa_{l\nu q'}\, e^{j(\beta_l-\beta_\nu-q'K_\mathrm{B})z}a_\nu(z). \tag{A.6}$$

In the work of this thesis related to Bragg filtering, it is assumed that there is only coupling between forward and backward propagating fundamental modes, with amplitudes $a(z)$ and $b(z)$, and propagation constants β and $-\beta$, respectively. In addition, it is assumed that only the first harmonic $q'=1$ is the relevant one (i.e., the device is operating in the first Bragg zone). The coupling coefficient between then is $\kappa_1\equiv\kappa$. Then, Eqs. (A.6) become

$$\frac{\mathrm{d}a(z)}{\mathrm{d}z} = -j\kappa\, e^{j2\delta z}b(z) \tag{A.7}$$

$$\frac{\mathrm{d}b(z)}{\mathrm{d}z} = j\kappa\, e^{-j2\delta z}a(z) \tag{A.8}$$

where the Bragg detuning parameter $\delta=\beta-K_\mathrm{B}/2$ has been defined.

A.1 Frequency response of a lossy Bragg filter

Assuming that the fundamental mode of the waveguide has a loss coefficient α, Eqs. (A.7) and (A.8) are modified as follows [138]

$$\frac{\mathrm{d}a(z)}{\mathrm{d}z} = -j\kappa\, e^{j2\delta z}b(z)-\alpha a(z) \tag{A.9}$$

$$\frac{\mathrm{d}b(z)}{\mathrm{d}z} = j\kappa\, e^{-j2\delta z}a(z)+\alpha b(z) \tag{A.10}$$

Note that in the absence of perturbations ($\kappa=0$), Eqs. (A.9) and (A.10) become

$$\frac{\mathrm{d}a(z)}{\mathrm{d}z} = -\alpha a(z) \tag{A.11}$$

$$\frac{\mathrm{d}b(z)}{\mathrm{d}z} = +\alpha b(z) \tag{A.12}$$

whose solution is $a(z)=C_1e^{-\alpha z}$ and $b(z)=C_2e^{\alpha z}$ which is indeed the known evolution of modes amplitude with losses.

To solve the differential system of equations, the following variable changes $A(z) = a(z)e^{-j\delta z}$ and $B(z) = b(z)e^{j\delta z}$ are made. Then,

$$\begin{aligned}\frac{\mathrm{d}a(z)}{\mathrm{d}z} &= \frac{\mathrm{d}}{\mathrm{d}z}\left(A(z)\,e^{j\delta z}\right)\\ &= \frac{\mathrm{d}A(z)}{\mathrm{d}z}\,e^{j\delta z} + j\delta A(z)\,e^{j\delta z}\end{aligned} \tag{A.13}$$

$$\frac{\mathrm{d}b(z)}{\mathrm{d}z} = \frac{\mathrm{d}B(z)}{\mathrm{d}z}\,e^{-j\delta z} - j\delta B(z)\,e^{j\delta z}. \tag{A.14}$$

Substituting Eqs. (A.13) and (A.14) into Eqs. (A.9) and (A.10) leads to

$$\frac{\mathrm{d}A(z)}{\mathrm{d}z} = -j\kappa B(z) - (\alpha + j\delta)A(z) \tag{A.15}$$

$$\frac{\mathrm{d}B(z)}{\mathrm{d}z} = j\kappa A(z) + (\alpha + j\delta)B(z). \tag{A.16}$$

The system of ordinary differential equations can be solved by differentiating one of the equations

$$\begin{aligned}\frac{\mathrm{d}^2B(z)}{\mathrm{d}z^2} &= j\kappa\frac{\mathrm{d}A(z)}{\mathrm{d}z} + (\alpha + j\delta)\frac{\mathrm{d}B(z)}{\mathrm{d}z}\\ &= j\kappa\left[-j\kappa B(z) - (\alpha + j\delta)A(z)\right]\\ &\quad + (\alpha + j\delta)\left[j\kappa A(z) + (\alpha + j\delta)B(z)\right]\\ &= \left[\kappa^2 + (\alpha + j\delta)^2\right]B(z).\end{aligned} \tag{A.17}$$

The parameter $\gamma^2 = \kappa^2 + (\alpha + j\delta)^2$ is introduced so the equation takes the form

$$\frac{\mathrm{d}^2B(z)}{\mathrm{d}z} = \gamma^2 B(z) \tag{A.18}$$

whose solution is known

$$B(z) = C_1\sinh\left[\gamma\,(L-z)\right] + C_2\cosh\left[\gamma\,(L-z)\right] \tag{A.19}$$

$$\begin{aligned}A(z) = {} & j\frac{C_1}{\kappa}\left\{(\alpha + j\delta)\sinh\left[\gamma\,(L-z)\right] + \gamma\cosh\left[\gamma\,(L-z)\right]\right\}\\ & + j\frac{C_2}{\kappa}\left\{\gamma\sinh\left[\gamma\,(L-z)\right] + (\alpha + j\delta)\cosh\left[\gamma\,(L-z)\right]\right\}.\end{aligned} \tag{A.20}$$

The constants are found by imposing the boundary conditions $a(0) = A(0) = 1$ and $b(L) = B(L) = 0$. In other words, the device is excited with the fundamental fordward mode at $z = 0$ and no signal is injected backwards at the distance L, which is the length of the grating. The resulting constants are

$$C_1 = \frac{-j\kappa}{(\alpha + j\delta)\sinh(\gamma L) + \gamma\cosh(\gamma L)} \tag{A.21}$$

$$C_2 = 0. \tag{A.22}$$

Defining Γ as the complex amplitude of the reflected mode at the beginning of the filter and T as the transmitted forward mode amplitude, the followign expressions are obtained

$$\Gamma = B(0) = \frac{-j\kappa \sinh(\gamma L)}{(\alpha + j\delta)\sinh(\gamma L) + \gamma \cosh(\gamma L)} = \frac{-j\kappa \tanh(\gamma L)}{\gamma + (\alpha + j\delta)\tanh(\gamma L)} \tag{A.23}$$

$$T = A(L) = \frac{\gamma}{(\alpha + j\delta)\sinh(\gamma L) + \gamma \cosh(\gamma L)}. \tag{A.24}$$

Finally, the reflectance and the transmittance are the result of taking the squared magnitude of Γ and T, respectively.

$$|\Gamma|^2 = \left| \frac{\kappa \tanh(\gamma L)}{\gamma + (\alpha + j\delta)\tanh(\gamma L)} \right|^2 \tag{A.25}$$

$$|T|^2 = \left| \frac{\gamma}{(\alpha + j\delta)\sinh(\gamma L) + \gamma \cosh(\gamma L)} \right|^2 \tag{A.26}$$

Eq. (A.25) corresponds to Eq. (2) in [92].

A.2 Bragg grating superstructure

In this section, CMT is employed to analyze the response of the tunable Bragg filter of sec. 2.1.3. The perturbation created in the periodically heated Bragg grating can be expressed as the product of two periodic perturbations:

$$\kappa(z) = \tilde{\kappa}(z) \cdot \hat{\kappa}(z). \tag{A.27}$$

In Eq. (A.27), $\tilde{\kappa}$ represents the perturbation created by the base Bragg grating with period Λ_B and $\hat{\kappa}$ corresponds to the perturbation added by the heaters, with period Λ_H much greater than Λ_B. This is analogous to an analog amplitude modulation, where lower frequency modulating signal ($\hat{\kappa}$) multiplies a higher frequency carrier ($\tilde{\kappa}$). Since both functions are periodic they can be expanded in Fourier series

$$\kappa(z) = \sum_q \tilde{\kappa}_q e^{-jqK_B z} \sum_p \hat{\kappa}_p e^{-jpK_H z}. \tag{A.28}$$

With this new definition of $\kappa(z)$, Eq. (A.4) is modified as follows

$$\pm \frac{da_l}{dz} = -j \sum_\nu \sum_q \sum_p \tilde{\kappa}_{l\nu q} \hat{\kappa}_{l\nu p} \, e^{j(\beta_l - \beta_\nu - qK_B - pK_H)z} a_\nu(z) \tag{A.29}$$

and the modified Bragg condition

$$\beta_l - \beta_\nu - qK_B - pK_H = 0. \tag{A.30}$$

Again, it is assumed that coupling occurs between fordward and backward fundamental modes ($\beta_l = \beta = -\beta_\nu$) and operation in the first Bragg zone ($q = 1$)

$$2\beta - K_B - pK_H = 0. \tag{A.31}$$

Introducing a low-spatial frequency superstructure provokes the Bragg resonance to be distributed between a discrete set of frequencies or wavelengths.

The wavelength spacing $\Delta\lambda_{\mathrm{H}} = \lambda_{p+1} - \lambda_p$ between these induced resonances can be obtained from Eq. (A.31) evaluated for two adjacent resonances

$$2\beta(\lambda_p) - K_{\mathrm{B}} - pK_{\mathrm{H}} = 0 \tag{A.32}$$

$$2\beta(\lambda_{p+1}) - K_{\mathrm{B}} - (p+1)K_{\mathrm{H}} = 0. \tag{A.33}$$

Substracting these two equations leads to

$$\begin{aligned} 2(\beta(\lambda_p) - \beta(\lambda_{p+1})) - K_{\mathrm{H}} &= 0 \\ \frac{n_{\mathrm{eff}}(\lambda_p)}{\lambda_p} - \frac{n_{\mathrm{eff}}(\lambda_{p+1})}{\lambda_{p+1}} - \frac{1}{2\Lambda_{\mathrm{H}}} &= \end{aligned} \tag{A.34}$$

A first-order approximation of $n_{\mathrm{eff}}(\lambda_{p+1})$ is used

$$\frac{n_{\mathrm{eff}}(\lambda_p)}{\lambda_p} - \frac{n_{\mathrm{eff}}(\lambda_p) + n'_{\mathrm{eff}}(\lambda_p)(\lambda_{p+1} - \lambda_p)}{\lambda_{p+1}} \approx \frac{1}{2\Lambda_{\mathrm{H}}} \tag{A.35}$$

where $n'_{\mathrm{eff}} = \frac{\mathrm{d}n_{\mathrm{eff}}}{\mathrm{d}\lambda}$. Manipulating Eq. (A.35) leads to

$$\begin{aligned} \frac{n_{\mathrm{eff}}(\lambda_p)\lambda_{p+1} - n_{\mathrm{eff}}(\lambda_p)\lambda_p - n'_{\mathrm{eff}}(\lambda_p)\lambda_{p+1}\lambda_p + \lambda_p^2 n_{\mathrm{eff}}(\lambda_p)}{\lambda_p\lambda_{p+1}} &= \frac{1}{2\Lambda_{\mathrm{H}}} \\ \frac{\lambda_{p+1}(n_{\mathrm{eff}}(\lambda_p) - \lambda_p n'_{\mathrm{eff}}(\lambda_p)) - \lambda_p(n_{\mathrm{eff}}(\lambda_p) - \lambda_p n'_{\mathrm{eff}}(\lambda_p))}{\lambda_p\lambda_{p+1}} &= \frac{1}{2\Lambda_{\mathrm{H}}}. \end{aligned} \tag{A.36}$$

By applying the definition of group index ($n_{\mathrm{g}} = n_{\mathrm{eff}} - \lambda n'_{\mathrm{eff}}$) and approximating $\lambda_p\lambda_{p+1} \approx \lambda^2$, Eq. (A.36) is simplified to

$$\frac{(\lambda_{p+1} - \lambda_p)n_{\mathrm{g}}}{\lambda^2} = \frac{1}{2\Lambda_{\mathrm{H}}} \tag{A.37}$$

which after reordering results in Eq. (6) of [98]

$$\Delta\lambda_{\mathrm{H}} = \frac{\lambda^2}{2n_{\mathrm{g}}\Lambda_{\mathrm{H}}}. \tag{A.38}$$

In a more general case, the coupling coefficient is considered to be modulated by a function $\hat{\kappa}(z)$ that is not necessarily periodic,

$$\kappa(z) = \hat{\kappa}(z)\tilde{\kappa}(z) = \hat{\kappa}(z)\sum_q \tilde{\kappa}_q e^{-jqK_{\mathrm{B}}z}. \tag{A.39}$$

Denoting the first harmonic of $\tilde{\kappa}$ as $\tilde{\kappa}_1$, the CMT system of equations is now

$$\frac{\mathrm{d}a(z)}{\mathrm{d}z} = -j\tilde{\kappa}_1\hat{\kappa}(z)e^{+j2\delta z}b(z) \tag{A.40}$$

$$\frac{\mathrm{d}b(z)}{\mathrm{d}z} = +j\tilde{\kappa}_1\hat{\kappa}(z)e^{-j2\delta z}a(z) \tag{A.41}$$

To solve Eqs. (A.40) and (A.41) local reflection coefficient is defined

$$r(z) = \frac{b(z)}{a(z)} \tag{A.42}$$

whose derivative w.r.t. z is

$$\begin{aligned}\frac{\mathrm{d}r(z)}{\mathrm{d}z} &= \frac{\frac{\mathrm{d}a(z)}{\mathrm{d}z}b(z) - a(z)\frac{\mathrm{d}b(z)}{\mathrm{d}z}}{[a(z)]^2} \\ &= \frac{j\tilde{\kappa}_1\hat{\kappa}(z)e^{-j2\delta z}[a(z)]^2 + j\tilde{\kappa}_1\hat{\kappa}(z)e^{j2\delta z}[b(z)]^2}{[a(z)]^2} \\ &= j\tilde{\kappa}_1\hat{\kappa}(z)e^{-j2\delta z}\left(1 + \left[e^{j2\delta z}r(z)\right]^2\right).\end{aligned} \tag{A.43}$$

Let r_1 be

$$r_1(z) = je^{j2\delta z}r(z) \tag{A.44}$$

and its derivative

$$\begin{aligned}\frac{\mathrm{d}r_1(z)}{\mathrm{d}z} &= j^2 2\delta e^{j2\delta z}r(z) + je^{j2\delta z}\frac{\mathrm{d}r(z)}{\mathrm{d}z} \\ &= j2\delta r_1(z) + je^{j2\delta z}j\tilde{\kappa}_1\hat{\kappa}(z)e^{-j2\delta z}\left(1 - [r_1(z)]^2\right) \\ &= j2\delta r_1(z) - \tilde{\kappa}_1\hat{\kappa}(z)\left(1 - [r_1(z)]^2\right).\end{aligned} \tag{A.45}$$

Eq. (A.45) is a Ricatti ordinary differential equation whose solution is not known. Dividing both sides by $\left(1 - [r_1(z)]^2\right)$ results in

$$\frac{1}{\left(1 - [r_1(z)]^2\right)}\frac{\mathrm{d}r_1(z)}{\mathrm{d}z} = j2\delta\frac{r_1(z)}{1 - [r_1(z)]^2} - \tilde{\kappa}_1\hat{\kappa}(z). \tag{A.46}$$

Given that $|r(z)| < 1$, an approximate soultion can be found by performing the following non-linear approximation

$$\tanh^{-1} f(x) \approx \frac{f(x)}{1 - [f(x)]^2}. \tag{A.47}$$

Then, Eq. (A.47) becomes

$$\frac{1}{1 - [r_1(z)]^2}\frac{\mathrm{d}r_1(z)}{\mathrm{d}z} \approx j2\delta\tanh^{-1}[r_1(z)] - \tilde{\kappa}_1\hat{\kappa}(z). \tag{A.48}$$

Let $r_2(z) = \tanh^{-1}[r_1(z)]$ and $\frac{\mathrm{d}r_2(z)}{\mathrm{d}z} = \frac{1}{1-[r_1(z)]^2}\frac{\mathrm{d}r_1(z)}{\mathrm{d}z}$, then

$$\frac{\mathrm{d}r_2(z)}{\mathrm{d}z} = j2\delta r_2(z) - \tilde{\kappa}_1\hat{\kappa}(z). \tag{A.49}$$

Multiplying both sides of the equation by $e^{-j2\delta z}$ leads to

$$\begin{aligned}\frac{\mathrm{d}r_2(z)}{\mathrm{d}z}e^{-j2\delta z} &= j2\delta r_2(z)e^{-j2\delta z} - \tilde{\kappa}_1\hat{\kappa}(z)e^{-j2\delta z} \\ \frac{\mathrm{d}r_2(z)}{\mathrm{d}z}e^{-j2\delta z} - j2\delta r_2(z)e^{-j2\delta z} &= -\tilde{\kappa}_1\hat{\kappa}(z)e^{-j2\delta z} \\ \frac{\mathrm{d}}{\mathrm{d}z}\left(e^{-j2\delta z}r_2(z)\right) &= -\tilde{\kappa}_1\hat{\kappa}(z)e^{-j2\delta z}.\end{aligned} \tag{A.50}$$

The perturbation is zero outside of the filter, i.e. $\hat{\kappa} \neq 0$, $0 \leq z \leq L$. Thus, Eq. (A.50) is solved integrating in that range

$$r_2(z) = -e^{j2\delta z} \int_0^z \tilde{\kappa}_1 \hat{\kappa}(z') e^{-j2\delta z'} \, \mathrm{d}z' + C e^{j2\delta z}. \tag{A.51}$$

The constant C is found applying the boundary condition $r_2(L) = 0$ (equivalent to $b(L) = 0$ as seen in the previous section)

$$\begin{aligned} C e^{j2\delta L} &= e^{j2\delta L} \int_0^L \tilde{\kappa}_1 \hat{\kappa}(z') e^{-j2\delta z'} \, \mathrm{d}z' \\ C &= \int_0^L \tilde{\kappa}_1 \hat{\kappa}(z') e^{-j2\delta z'} \, \mathrm{d}z'. \end{aligned} \tag{A.52}$$

And the reflection coefficient at the begining of the filter $\Gamma = r(0) = j e^{-j2\delta 0} r_1(0) = j \tanh[r_2(0)]$ is thus given by

$$\Gamma \approx j \tanh\left[- \int_0^L \tilde{\kappa}_1 \hat{\kappa}(z) e^{-j2\delta z} \, \mathrm{d}z \right]. \tag{A.53}$$

The result of Eq. (A.53) establish an approximated relationship between the spectral response of the filter and the Fourier Transform of the perturbation. It holds valid for low values of $|\Gamma|$ or when $\delta = 0$. For example, let $\hat{\kappa}$ be

$$\hat{\kappa}(z) = \begin{cases} 1, & 0 < z \leq L \\ 0, & \text{otherwise} \end{cases} \tag{A.54}$$

i.e., a regular Bragg filter. Using Eq. (A.53), the approximated reflectance is

$$|\Gamma|^2 \approx \tanh^2\left[\tilde{\kappa}_1 L e^{-j\delta L} \mathrm{sinc}\left(\frac{\delta L}{\pi} \right) \right] \tag{A.55}$$

which for $\delta = 0$ is

$$|\Gamma|^2 = \tanh^2(\tilde{\kappa}_1 L). \tag{A.56}$$

Now let $\hat{\kappa}$ be a periodic function expanded in Fourier series,

$$\hat{\kappa}(z) = \sum_p c_p e^{jpK_\mathrm{H} z}. \tag{A.57}$$

Then, using the shift property of the Fourier Transform, the approximated reflectance is

$$|\Gamma|^2 \approx \tanh^2\left[\tilde{\kappa}_1 L \sum_p c_p \mathrm{sinc}\left(\frac{(\delta - pK_\mathrm{H}/2) L}{\pi} \right) e^{-j(\delta - pK_\mathrm{H}/2)L} \right] \tag{A.58}$$

Appendix B

Resumen en español

B.1 Introducción

El creciente volumen de tráfico de información ha intensificado la necesidad de transceptores ópticos en las redes de telecomunicaciones. Paralelamente, la creciente demanda de servicios de streaming y en la nube, junto con la adopción de políticas de trabajo desde casa y la continua proliferación de la inteligencia artificial, han incrementado la necesidad de enlaces ópticos en los grandes centros de datos.

En los últimos años, la óptica integrada se ha consolidado como campo tecnológico, dedicado a la generación, manipulación y detección de la luz en circuitos integrados [1]. Aunque su principal campo de aplicación es el de las comunicaciones ópticas [2, 3], también se ha adoptado en otras áreas emergentes como el biosensado [4], comunicaciones cuánticas y procesado cuántico de la información [5] y los LiDAR [6], entre otras. A diferencia de los sistemas compuestos de componentes ópticos discretos, la óptica integrada consigue agrupar diversas funcionalidades ópticas en chips compactos, reduciendo el coste y la susceptibilidad a inestabilidades mecánicas.

De entre los materiales disponibles, esta tesis se centra en la fotónica del silicio, concretamente en la plataforma de silico sobre aislante (SOI, *Silicon On Insulator*) [13]. En la Fig. B.1(a) se muestra la estructura de capas típica de un chip SOI. Sobre un sustrato de silicio se hace crecer una capa de dióxido de silicio de entre 2 y 3 µm. Sobre esta se deposita una delgada capa de silicio sobre la cual se graban las guías fotónicas que conforman los dispositivos. Posteriormente, se deposita otra capa de dióxido de silicio que protege estas guías. En la Fig. B.1(b) se muestra una imagen de microscopio por escaneo de electrones (SEM, *Scanning Electron Microscopy*) de una guía fotónica *silicon wire*.

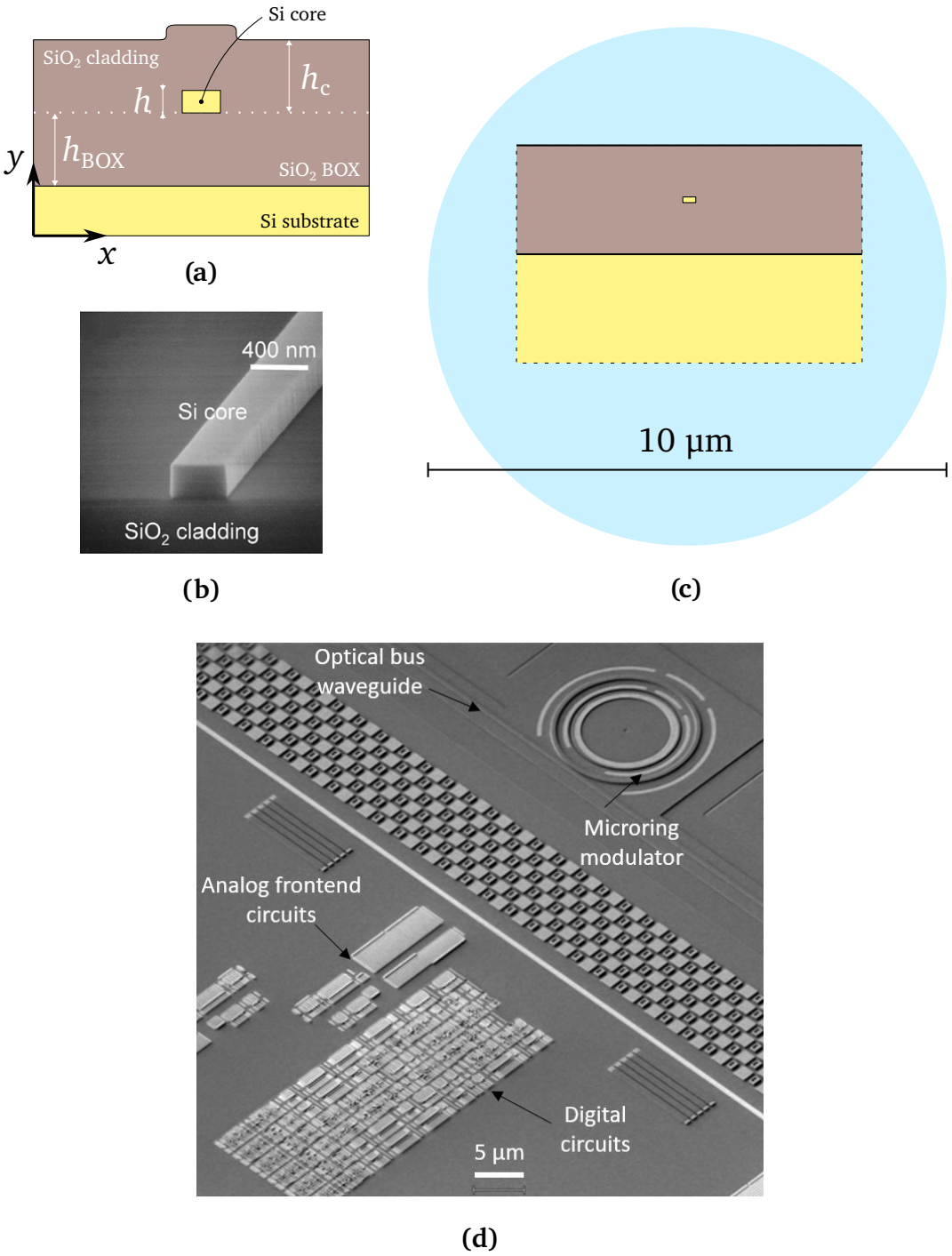

Figura B.1 La plataforma de silicio sobre aislante (SOI). (a) Representación esquemática de la sección transversal de una guía silicon wire. Las dimensiones típicas son $h \sim 220-300$ nm y $h_{BOX}, h_c \sim 2-3$ µm. (b) Imagen de microscopio por escaneo de electrones (SEM) de una guía silicon wire de 400 nm de ancho, obtenida de [18] © 2005 IEEE. (c) Comparación a escala de un silicon wire y el MFD de una fibra óptiica monomodo estandar para el infrarrojo cercano. (d) Imagen SEM de circuitos fotónicos y electrónicos cointegrados [15].

El alto contraste de índice de refracción de esta plataforma hace que los dispositivos fabricados sean muy compactos y los radios de curvatura de las guías, muy pequeños. En la Fig. B.1(c) se compara una guía típica con el diametro de campo modal (MFD, *Mode Field Diameter*) de una fibra óptica monomodo estándar. Además, esta plataforma es compatible con procesos de fabricación existentes para microelectrónica CMOS, permitiendo la fabricación en masa de circuitos fotónicos integrados y su cointegración con circuitos electrónicos como se muestra en la Fig. B.1(d). Sin embargo, los materiales están restringidos al silicio y al dióxido de silicio, y sus índices de refracción no se pueden modificar fácilmente. Las estructuras periódicas son una potencial solución a esta limitación.

Las estructuras periódicas juegan un rol fundamental en la fotónica integrada, otorgando a los dispositivos ópticos integrados de capacidades que las guías convencionales no pueden ofrecer. Las guías fotónicas periódicas poseen tres regímenes de operación en función de la relación entre la longitud de onda y el periodo de la estructura: *(i)* radiación, la luz incidente en la estructura es emitida hacia el exterior del chip, utilizado para el diseño de acopladores fibra-chip [21] y antenas ópticas [22]; *(ii)* Bragg, la guía periódica actúa como un reflector distribuido, útil para filtrado óptico [69, 70]; y *(iii)* sublongitud de onda, donde al ser el periodo más pequeño que la longitud de onda, los efectos difractivos se anulan y la estructura se comporta como un medio homogéneo anisótropo equivalente [19, 20, 32]. Estos materiales son conocidos como *SubWavelength Gratings* (SWG).

Esta tesis se centra en las dos últimas zonas de trabajo: Bragg y sublongitud de onda. El régimen de Bragg ha sido utilizado para diseñar un sensor de índice de refracción de alta sensibilidad y bajo límite de detección, así como un filtro multibanda de amplitudes reconfigurables. La zona SWG, se ha utilizado para diseñar un acoplador de interferencia multimodal (MMI, *MultiMode Interference*) insensible a la polarización y un expansor de haz ultra corto.

B.2 Contribuciones y resultados

En la Fig. B.2 se resumen las aportaciones de esta tesis y sus resultados.

Filtro Bragg de banda estrecha como sensor de índice de refracción

Los circuitos fotónicos basados en silicio son una alternativa prometedora para el desarrollo de sensores integrados para pruebas médicas de cabecera, tests de seguridad alimentaria y monitorización ambiental, derivando en última instancia en los llamados laboratorios en chip (*lab on a chip*) [72, 73]. Además, gracias al mecanismo de sensado por campo evanescente, es posible obtener sensores de altas prestaciones sin afectar a la muestra bajo test en comparación, por ejemplo, con pruebas que utilizan marcadores [81].

(Sec. 2.1.2)

Acoplador MMI insensible a la polarización

Modelado, diseño y simulación

[63] C. Pérez-Armenta et al., *Phot. Res.* **10** (4) A57–A65 (2022)

- Primera vez en SOI 220 nm
- Modelado anisótropo para ambas polarizaciones
- Rango espectral: 1.26–1.42 µm
  - Pérdidas de exceso < 1 dB
  - Desbalanceo < 1 dB
  - Error de fase $< 5°$

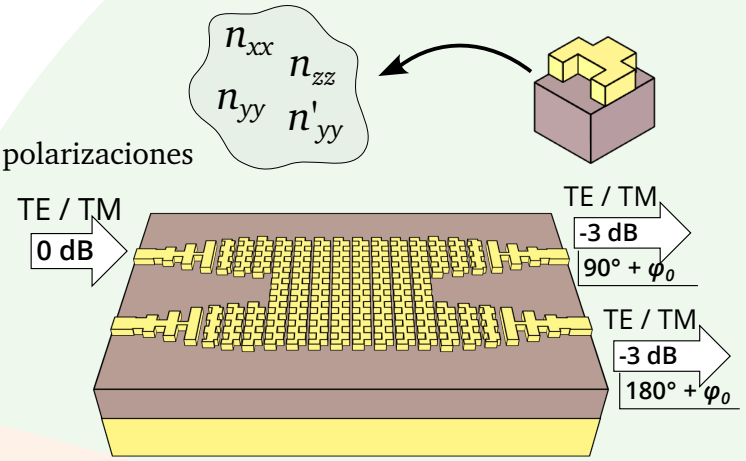

Validación experimental

[64] C. Pérez-Armenta et al., *Opt. & Laser Tech.* **164** 109493 (2023)

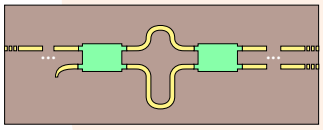

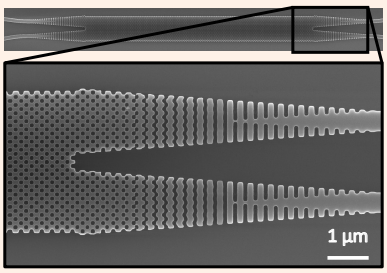

- Rango espectral: 1.49–1.58 µm (setup de medida)
- Área ocupada: 3.5 µm × 47.25 µm
- Figuras de mérito:
  - Pérdidas dependientes de la polarización < 1 dB
  - 0.7 dB $<$ Pérdidas de exceso < 1 dB
  - Desbalanceo < 1 dB de 1.5 a 1.56 µm
  - Error de fase $< 5°$

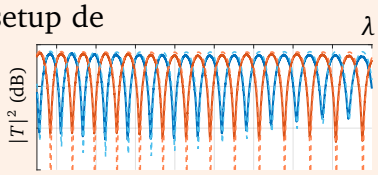

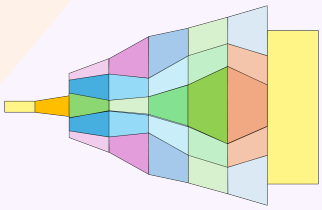

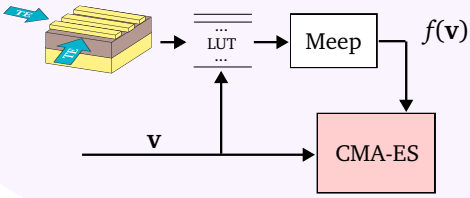

- Modelo anisótropo 2D de estructuras SWG
- Optimización usando el algoritmo CMA-ES

Figura B.2 Resumen de las contribuciones de esta tesis.

Sensor Bragg de banda estrecha

(Sec. 2.1.1)

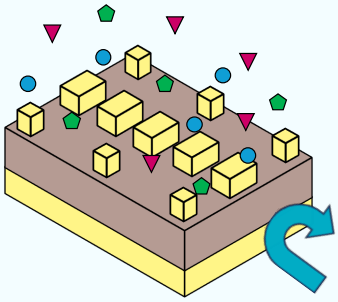

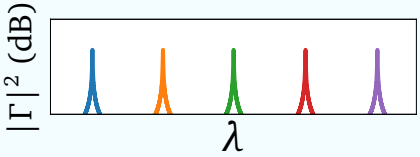

[92] C. Pérez-Armenta et al., *Opt. Expr.* **28** (25) 37971–37985 (2020)

- Guías SWG: alta sensibilidad
- Bloques laterales: bajo iLoD
- Modelo CMT con pérdidas
- Banda O: mejor LoD
- Bandgap diseñado: ~ 30 pm
- Sensibilidad del dispositivo: **507 nm/RIU**
- LoD intrínseco: $\mathbf{5.1 \cdot 10^{-5}}$ **RIU**

Superestructura Bragg controlada por temperatura

(Sec. 2.1.3)

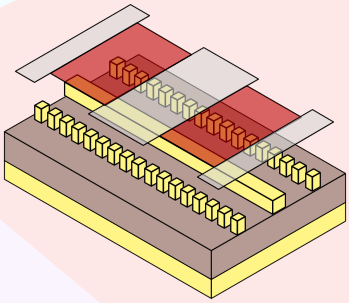

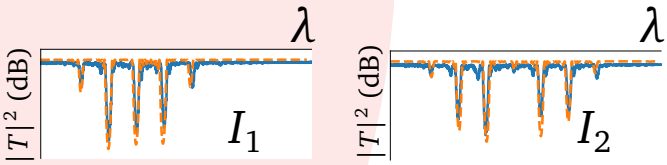

[98] C. Pérez-Armenta et al., *Opt. Expr.* **31** (13) 22225–22232 (2023)

- Topología Bragg con bloques laterales
- Bandgap diseñado: 1 nm
- Espaciado entre bandas diseñado: 5 nm
- Buena concordancia simulación-experimento

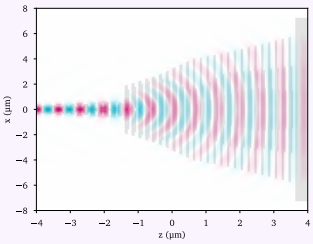

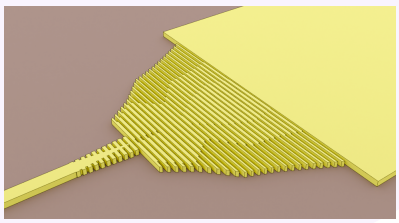

Diseño inverso asistido por guías SWG

(Capítulo 3)

- Despliegue en el superordenador de la Universidad de Málaga
- Se ha diseñado un expansor de haz de 500 nm a 12 μm de ancho de 7 μm de largo con pérdidas de inserción de 0.5 dB en un ancho de banda de >100 nm.

De cara al diseño de sensores ópticos integrados, las dos figuras de mérito clave son la sensibilidad, la tasa de cambio de la magnitud medida respecto a cambios en la sustancia de interés (analito), y el límite de detección, el mínimo cambio medible en el analito. Por ello, se ha hecho uso de una nueva topología de filtro Bragg [20, 69] mostrada en la Fig. B.3. Por un lado, la guía central SWG de esta topología posee gran sensibilidad [84] y por otro, los bloques laterales permiten crear bandas de rechazo o *bandgaps* muy estrechos pero con un tamaño mínimo de estructura fabricable, lo cual se complica utilizando otras técnicas como corrugaciones.

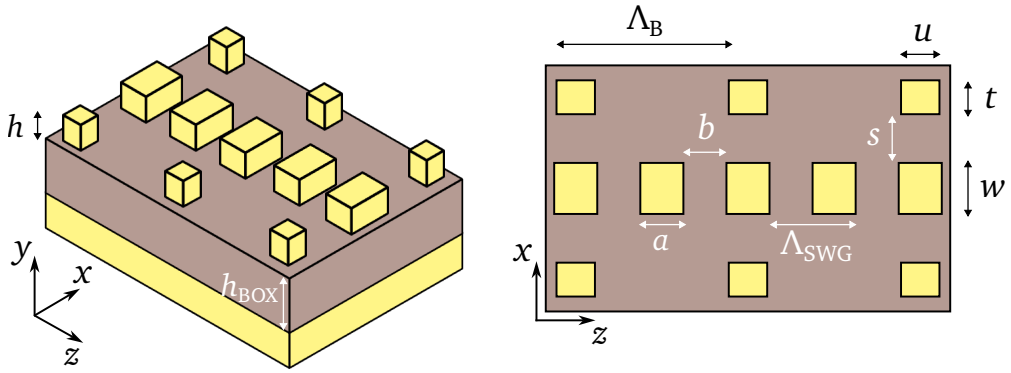

Figura B.3 Geometría del filtro Bragg utilizado como sensor en [92]. Sobre una guía SWG de periodo Λ_{SWG} y ciclo de trabajo DC $= a/\Lambda_{SWG}$ se crea un *bandgap* estrecho añadiendo periodicamente bloques laterales de tamaño $t \times u$ y periodo Λ_B.

En este estudio se hace uso de la Teoría de Modos Acoplados (CMT, *Coupled Mode Theory*) para el modelado y diseño del filtro, incluyendo el efecto de las pérdidas de propagación del modo fundamental de la guía. Analizando las expresiones deducidas, se identifica un compromiso entre el ancho de banda, pérdidas y nivel de señal, lo que ha conducido al método de diseño de este trabajo.

El diseño se ha realizado para la polarización TE (Transversal Eléctrica), para la cual es posible alcanzar sensibilidades mayores, y para banda O (1260–1360 nm) donde las pérdidas del agua son menores. Siguiendo el método de diseño propuesto en el trabajo, se consiguen una sensibilidad del dispositivo de 507 nm/RIU y un límite de detección de $5.1 \cdot 10^{-5}$ RIU. Estos resultados han sido publicados en el artículo "*Narrowband Bragg filters based on subwavelength grating waveguides for silicon photonic sensing*" [92].

Acopladores MMI insensibles a la polarización.

A pesar de las ventajas que posee la plataforma SOI, esta también exhibe una alta birrefringencia, especialmente para espesores de la capa de guiado de 220 nm, valor ampliamente usado en fábricas. Esto plantea desafíos, especialmente en escenarios en los que se reciben señales con estados de polarización indeterminados o en los que se

emplea multiplexación por división en polarización. Es deseable, por tanto, disponer de dispositivos ópticos integrados independientes de la polarización.

El segundo hito de esta tesis ha consistido en el diseño y caracterización de acopladores MMI 2 × 2 insensibles a la polarización. Para ello se ha hecho uso de un metamaterial periódico de aspecto enladrillado, propuesto por primera vez en [31], en el núcleo multimodo del acoplador, como se aprecia en la Fig. B.4. Esta topología de guía SWG se denomina *bricked* SWG. El modelo presentado en [31] mostró que los componentes del tensor de permitividad eléctrica que afectan a la polarización TE pueden ser diseñados facilmente ajustando la geometría de la guía bricked SWG, mientras que la componente que afecta a los modos TM permanece prácticamente inalterada. Este hallazgo sugería que, para una cierta combinación de los parámetros geométricos de la guía, era posible igualar el comportamiento del dispositivo para las dos polarizaciones.

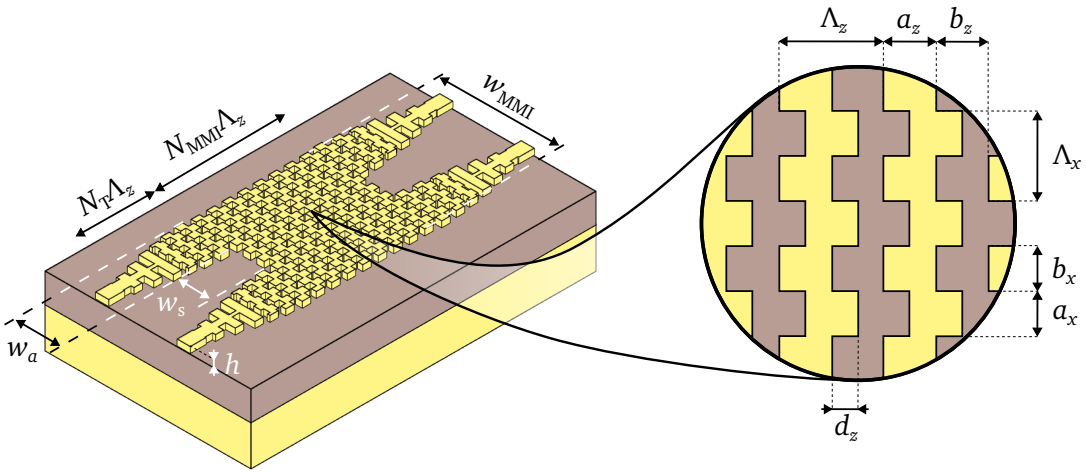

Figura B.4 Geometría del acoplador MMI implementado en [63, 64]. Un metamaterial de aspecto enladrillado se usa como núcleo de la guía multimodo. Las tiras de silicio de una guía SWG convencional de periodo Λ_z y ciclo de trabajo $DC_z = a_z/\Lambda_z$ se dividen periódicamente en la dirección transversal con periodo Λ_x y ciclo de trabajo $DC_x = a_x/\Lambda_x$. Posteriormente, los bloques resultantes de tamaño $a_x \times a_z$ se desplazan en la dirección de propagacion una distancia d_z.

En un primer diseño, se ha conseguido un MMI 2 × 2 insensible a la polarización para banda O, de forma que verificase la capacidad de la guía bricked SWG para relajar las restricciones de tamaños mínimos. El MMI diseñado posee, en simulación, pérdidas de exceso y desbalanceo menores a 1 dB y errores de fase menores que 5° en el rango de longitudes de onda entre 1.26 y 1.42 µm. Los detalles del modelado y diseño de este dispositivo se discuten en la publicación "*Polarization-independent multimode interference coupler with anisotropy-engineered bricked metamaterial*" [63].

Debido a limitaciones en el instrumental de laboratorio en el momento de la fabri-

cación, concrétamente en el rango espectral de la fuente láser sintonizable, el acoplador MMI fue rediseñado para banda C (1530–1565 nm). Utilizando el dispositivo como divisor y combinador de un interferómetro de Mach-Zehnder, se han extraído las figuras de mérito de cada una de las variaciones introducidas en el chip. Para el mejor de los dispositivos fabricados, se han obtenido pérdidas de exceso inferiores a 1 dB, pérdidas dependientes de la polarización menores a 0.25 dB y errores de fase por debajo de los 5° en el ancho de banda de 1495 a 1580 nm. El desbalanceo resulta el parámetro más limitante, siendo inferior a 1 dB en un ancho de banda de 60 nm. Este trabajo supone la primera demostración experimental de un MMI insensible a la polarización en la plataforma SOI de 220 nm de espesor. Estos resultados, junto con más información sobre la caracterización del dispositivo, han sido publicados en el artículo "*Polarization insensitive metamaterial engineered multimode interference coupler in a 220 nm silicon-on-insulator platform*" [64].

Generación y control de amplitud de bandas laterales en filtros Bragg

La reconfigurabilidad de elementos de filtrado en fotónica integrada es una característica deseable en aplicaciones de tiempo real. En SOI, es posible crear filtros Bragg sintonizables utilizando efectos electroópticos [93], materiales de cambio de fase [94] y efectos termoópticos [95]. Por otro lado, el filtrado de múltiples bandas es necesario en sistemas que utilizan multiplexación por división en longitud de onda (WDM, *Wavelength Division Multiplexing*).

El siguiente hito de esta tesis ha consistido en el diseño, fabricación y caracterización de un filtro multibanda basado en una superestructura Bragg creada mediante el efecto termoóptico. Este trabajo se ha llevado a cabo en un proyecto de colaboración con el *National Research Council of Canada* y la Universidad de Carleton (Ottawa). La geometría del filtro se muestra en la Fig. B.5. Sobre un filtro Bragg de banda estrecha, similar al empleado en el sensor Bragg, se disponen de forma periódica tiras de calentador conectadas en serie. Al aplicar una corriente eléctrica, el perfil de temperatura genera en el espectro una serie de bandas de rechazo equiespaciadas, cuya amplitud es depende de la intensidad de dicha corriente.

Los chips fabricados fueron recibidos en el National Research Council of Canada, donde el candidato ha llevado a cabo la caracterización experimental durante una estancia de investigación. Las medidas de los dispositivos fabricados han mostrado buena concordancia con respecto a las simulaciones hechas en la fase de diseño. Puede encontrarse más información al respecto en otra de las publicaciones que avalan la tesis: "*Thermally induced sideband generation in silicon-on-insulator cladding modulated Bragg notch filters*" [98].

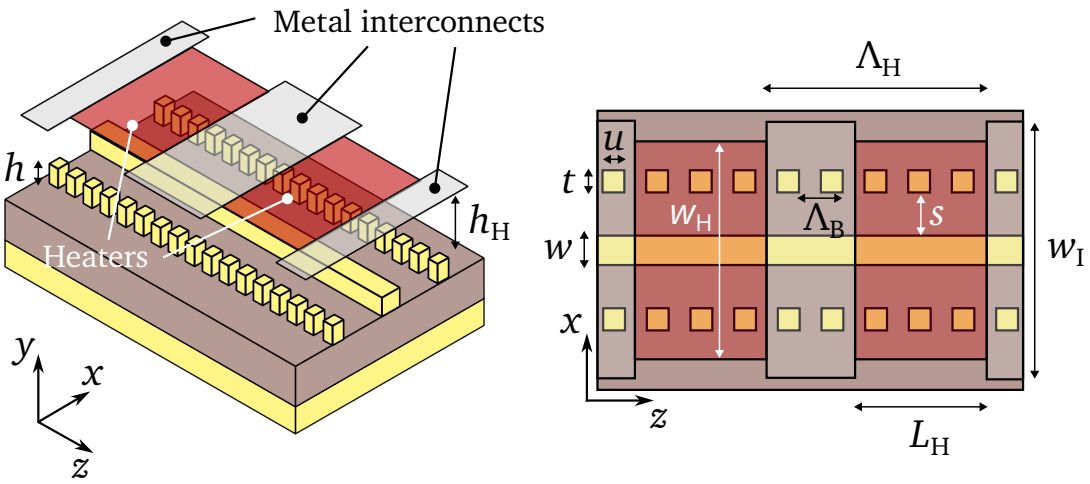

Figura B.5 Geometría del filtro reconfigurable demostrado en [98]. Está basado en un filtro Bragg sintetizado con bloques laterales. La cubierta de dióxido de silicio no se muestra por claridad. Sobre el filtro se disponen periódicamente tiras de calentador, con un periodo Λ_H y ciclo de trabajo $DC_H = L_H/\Lambda_H$. El filtro se ha diseñado para la longitud de onda de 1550 nm y la polarización TM (Transversal Magnética).

Diseño inverso de un expansor de haz ultracorto basado en SWGs

El diseño inverso en fotónica ha ganado una atención significativa en los últimos años debido a la creciente disponibilidad de infraestructuras de computación de alto rendimiento. Esto ha facilitado el diseño automático de dispositivos muy compactos y de altas prestaciones [108]. El diseñador proporciona a un algoritmo de optimización una función objetivo a optimizar, variables de diseño que parametrizan una estructura fotónica genérica, e inicialización y límites para estas variables. A medida que la función objetivo se maximiza o minimiza, el comportamiento del dispositivo se aproxima a la respuesta objetivo. El proceso finaliza con una geometría de dispositivo sintetizada que satisface los objetivos fijados al principio.

Es muy importante elegir un algoritmo de optimización adecuado al problema tratado. Los métodos basados en el gradiente son adecuados cuando se conoce una buena solución inicial. Bajo ciertas condiciones, se garantiza su convergencia, aunque son susceptibles de converger a un óptimo local en lugar de a uno global. Además en problemas de caja negra, donde el gradiente es desconocido y debe ser estimado, el tiempo de optimización resulta prohibitivo ya que las simulaciones electromagnéticas necesarias son muy costosas en tiempo. Una solución es el método del adjunto [111–113], aunque limita la forma en la que se puede parametrizar la estructura y puede requerir un procesado adicional para obtener una estructura fabricable [114].

Por otro lado, los algoritmos de optimización global pueden operar sin necesidad de conocer el gradiente. Aunque su convergencia pueda ser más lenta y no esté garantizada,

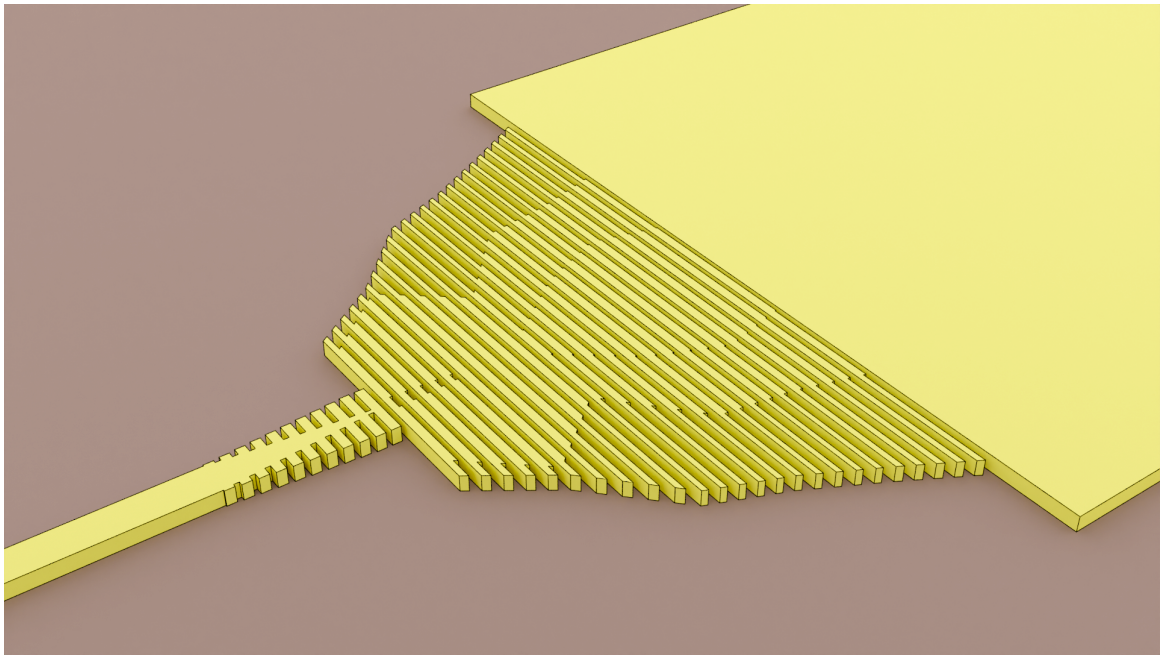

Figura B.6 Diseño final del expansor de haz basado en secciones SWG optimizadas.

su naturaleza exploratoria los hace menos propensos a quedar atrapados en óptimos locales. La Estrategia de Evolución basada en la Adaptación de la Matriz de Covarianza (CMA-ES, *Covariance Matrix Adaptation–Evolution Strategy*) es una alternativa interesante dentro de los algoritmos globales [123]. Solo es necesario definir un tamaño de población y candidato(s) iniciales, y ha demostrado buen desempeño en problemas electromagnéticos [47, 124–127].

En el último trabajo de esta tesis, se ha diseñado y fabricado un expansor de haz ultracorto para la plataforma SOI de 220 nm y polarización TE. Para ello se ha empleado un nuevo método de diseño inverso que utiliza metamateriales SWG y que está dividido en dos etapas: una en la que los SWG son modelados como materiales anisótropos 2D, permitiendo una primera optimización rápida; y una segunda en la que se optimiza la estructura 3D completa partiendo de una buena candidata inicial. Se ha utilizado el algoritmo CMA-ES y la evaluación en paralelo de la población de cada generación se ha llevado a cabo en el superordenador de la Universidad de Málaga *Picasso*.

El diseño final se muestra en la Fig. B.6. Adapta el modo fundamental de una guía de 500 nm de ancho al de una de 12 µm, en una longitud de tan solo 7 µm de largo con pérdidas inferiores a 1 dB en un ancho de banda de 300 nm en simulación. Esto lo hace uno de los dispositivos más cortos y con mejores prestaciones de entre los encontrados en el estado del arte. Su caracterización experimental se está llevando a cabo actualmente, aunque unos resultados experimentales preliminares muestran que algunos de los prototipos fabricados presentan pérdidas en torno a 0.5 dB en todo el ancho de banda de medición como predecían las simulaciones.

Una vez se haya completado la caracterización experimental, los resultados de este trabajo serán publicados en una revista científica de alto impacto.

B.3 Conclusiones y líneas futuras

B.3.1 Conclusiones

El diseño de dispositivos fotónicos haciendo uso de estructuras periódicas se ha convertido en una herramienta esencial y de alto potencial en la fotónica de silicio, específicamente en la plataforma SOI. Las guías SWG permiten mejorar las prestaciones de los dispositivos fotónicos, así como crear nuevas funcionalidades sin necesidad de recurrir a procesos de fabricación más complejos que incrementan los costes de fabricación. Además, los filtros de Bragg débiles se presentan como una solución atractiva para implementar filtros de banda estrecha con aplicaciones en comunicaciones y sensado.

En esta tesis se han realizado avances significativos tanto en el campo de los metamateriales SWG como en el de los filtros de Bragg. Se han introducido herramientas mejoradas de modelado y simulación. Se han desarrollado nuevas topologías SWG y métodos de diseño que se han aplicado a los siguientes dispositivos: *(i)* acopladores MMI insensibles a la polarización, *(ii)* un filtro Bragg como sensor de índice de refracción, *(iii)* un filtro de Bragg reconfigurable y *(iv)* un expansor de haz en guía ultracorto y de banda ultraancha. Se han realizado simulaciones electromagnéticas rigurosas para todos los dispositivos, y la mayoría han sido sometidos a caracterización experimental. Los resultados de estas contribuciones se han difundido a través de publicaciones en revistas de alto impacto revisadas por pares y conferencias nacionales e internacionales.

Como resultado del trabajo de investigación llevado a cabo en esta tesis, se han derivado las siguientes conclusiones.

La importancia del modelado y la disponibilidad de herramientas de simulación eficientes

La simulación de estructuras periódicas puede requerir de muchos recursos computacionales, especialmente al usar métodos FDTD 3D *full-vectorial*. El modelo CMT permite cálculos semi-analíticos de la respuesta en longitud de onda de un filtro Bragg, asistidos por el cálculo de los parámetros clave del filtro (fuerza del grating, índice de refracción e índice de grupo). Con esto se consiguen simulaciones muy rápidas y rigurosas en comparación con algoritmos como FDTD, cuyo tiempo de simulación sería inviable para estructuras largas.

La utilización de modelos 2D en la etapa de diseño preliminar de los acopladores MMI insensibles a la polarización y el expansor de haz ha demostrado ser crucial para alcanzar

rápidamente una aproximación inicial que reduce el tiempo total de simulación en 3D. En el caso del MMI independiente de la polarización, el modelo 2D también proporciona conocimiento físico sobre la formación de imágenes en el medio anisótropo. El modelo facilita la comprensión de cómo la geometría afecta el comportamiento del MMI y ayuda a encontrar combinaciones de parámetros candidatos para el régimen independiente de la polarización. En el método de diseño inverso presentado en el capítulo 3, los SWG han sido modelados exitosamente como materiales anisótropos homogéneos, lo que facilita la definición de la forma del dispositivo y es susceptible de ser generalizado a otras estructuras SWG, como las estructuras bricked SWG, y de ser utilizado en dispositivos más complejos.

Se puede lograr insensibilidad a la polarización utilizando topologías avanzadas de SWG

Los SWG han demostrado en los últimos años ser una excelente forma de controlar las propiedades ópticas de los dispositivos fotónicos integrados. En esta tesis, se ha investigado la nueva topología de bricked SWG para lograr la independencia de la polarización. Se han diseñado y caracterizado experimentalmente MMIs 2×2 para la plataforma SOI de 220 nm de espesor. La metodología desarrollada en estos trabajos puede ser fácilmente generalizada a MMIs con un mayor número de puertos, abriendo el camino a dispositivos fotónicos de silicio insensibles a la polarización que son irrealizables utilizando técnicas convencionales.

La nueva topología de filtros Bragg permite desarrollar sensores resonantes estado del arte

Se ha diseñado un sensor de índice de refracción de altas prestaciones. La topología de filtro Bragg utilizada posee una alta sensibilidad proporcionada por la guía SWG y consigue un mejor límite de detección al reducir el ancho de banda sin comprometer el tamaño mínimo de estructura. Además, la metodología de diseño desarrollada en este trabajo tiene en cuenta las pérdidas de propagación a lo largo del filtro, estableciendo un límite inferior para el ancho de banda del filtro. Se muestra que al reducir la longitud de onda de operación a 1310 nm en lugar de 1550 nm, el límite de detección intrínseco del dispositivo puede mejorar un orden de magnitud.

Filtros reconfigurables basados en superestructuras Bragg para la plataforma SOI

Se ha llevado a cabo con éxito una prueba de concepto de superestructuras Bragg. Esto implica el diseño y la caracterización de un filtro de Bragg modulado por temperatura para la plataforma SOI, demostrando el ajuste de la amplitud de bandas laterales. Los hallazgos de este trabajo crean perspectivas prometedoras para la multiplexación por división de longitud de onda y la compensación de dispersión en la fotónica de silicio.

Los SWG proporcionan nuevas posibilidades para el diseño inverso

En el trabajo descrito en el capítulo 3, se ha desarrollado una nueva técnica de diseño inverso que combina la optimización global y los metamateriales SWG. Los SWG añaden más grados de libertad, ya que se puede sintetizar un conjunto continuo de materiales, no restringiendo al algoritmo a solo ajustar la forma del dispositivo. Además, los dispositivos obtenidos pueden beneficiarse de las propiedades anisótropas de los SWG para mejorar el rendimiento del dispositivo. Este ha sido el caso del expansor de haz diseñado en esta tesis, exhibiendo adaptación de banda ancha en una distancia muy corta.

B.3.2 Líneas futuras

Los resultados de esta tesis sientan las bases para varias potenciales líneas de investigación. A continuación se presenta una lista de posibles direcciónes futuras.

Diseño y demostración experimental de dispositivos insensibles a la polarización

Además de los acopladores MMI, se podría diseñar una amplia gama de dispositivos fotónicos utilizando la topología bricked SWG u otras, buscando la insensibilidad la polarización. Esto incluye dispositivos como acopladores superficiales, filtros, cruces o divisores más complejos.

Demostración experimental del sensor Bragg

La caracterización experimental del sensor Bragg propuesto no ha sido llevada a cabo. En un trabajo reciente del laboratorio de fotónica de la Universidad de Málaga, los filtros Bragg fabricados presentaron discrepancias con el espectro objetivo [145]. Se propuso un modelo estocástico para simular errores de fabricación incluyéndolos en un término de error de fase acumulada en el filtro Bragg. Por lo tanto, la tolerancia del sensor a los errores de fase debe ser estudiada antes de ser fabricado.

Filtros reconfigurables con espectro arbitrario

El espectro del filtro reconfigurable diseñado en esta tesis es relativamente simple, consistiendo solo en un conjunto de picos en reflexión. Además, las amplitudes de los diferentes picos no son libremente ajustables. Diseñando una disposición de calentadores más compleja, se podrían sintetizar filtros fotónicos avanzados solo reconfigurando el perfil de temperatura.

Demostración experimental y generalización de la metodología de diseño inverso

La caracterización experimental del expansor de haz está actualmente en proceso. En el momento de escritura de esta tesis, se ha fabricado un chip de prueba y se ha recibido en

las instalaciones del grupo de investigación. Algunas medidas preliminares prometedoras se han incluido en esta tesis. Además, siguiendo el plan de trabajo del proyecto de investigación METAPHOR en el que se enmarca este trabajo, la metodología propuesta se extenderá a (a) otros tipos de dispositivos, como divisores y rotadores de polarización, acopladores de fibra y multiplexores de modo; y (b) otras topologías SWG.

Appendix C

Curriculum Vitae

Carlos Pérez Armenta earned the BSc. and MSc. in Telecommunication Engineering from the University of Málaga in 2018 and 2020, respectively. In 2020 he received a national grant from the Spanish Ministry of Science that funded his Ph.D. on the development of advanced periodic photonic devices, supervised by Prof. Dr. Gonzalo Wangüemert Pérez and Prof. Dr. Alejandro Ortega Moñux. The work developed in this PhD thesis was mostly done in the Photonics & RF Research Lab at the University of Malaga but in close collaboration with the National Research Council of Canada (NRC). A complete list of his publications is given below.

Research articles in international journals

1. C. Pérez-Armenta, K. K. MacKay, A. Hadij-ElHouati, A. Ortega-Moñux, I. Molina-Fernández, J. G. Wangüemert-Pérez, J. H. Schmid, P. Cheben, and W. N. Ye, "Thermally induced sideband generation in silicon-on-insulator cladding modulated bragg notch filters," *Opt. Express*, vol. 31, no. 13, pp. 22 225–22 232, Jun. 2023. DOI: 10.1364/OE.488108
2. C. Pérez-Armenta, A. Ortega-Moñux, J. M. Luque-González, R. Halir, J. Schmid, P. Cheben, I. Molina-Fernández, and J. G. Wangüemert-Pérez, "Polarization insensitive metamaterial engineered multimode interference coupler in a 220 nm silicon-on-insulator platform," *Optics & Laser Technology*, vol. 164, p. 109 493, Apr. 2023. DOI: 10.1016/j.optlastec.2023.109493
3. C. Pérez-Armenta, A. Ortega-Moñux, J. M. Luque-González, R. Halir, P. J. Reyes-Iglesias, J. Schmid, P. Cheben, Í. Molina-Fernández, and J. G. Wangüemert-Pérez, "Polarization-independent multimode interference coupler with anisotropy-engineered bricked metamaterial," *Photon. Res.*, vol. 10, no. 4, A57–A65, Apr. 2022. DOI:

10.1364/PRJ.446932

4. C. Pérez-Armenta, A. Ortega-Moñux, J. Čtyroký, P. Cheben, J. H. Schmid, R. Halir, Í. Molina-Fernández, and J. G. Wangüemert-Pérez, "Narrowband bragg filters based on subwavelength grating waveguides for silicon photonic sensing," *Opt. Express*, vol. 28, no. 25, pp. 37 971–37 985, Dec. 2020. DOI: 10.1364/OE.404364

International conference proceedings

1. C. Pérez-Armenta, A. Ortega-Moñux, J. M. Luque-González, R. Halir, P. Reyes-Iglesias, J. H. Schmid, P. Cheben, Í. Molina-Fernández, and J. G. Wangüemert-Pérez, "Polarization independent 2×2 multimode interference coupler with bricked subwavelength metamaterial," in *European Optical Society Annual Meeting (EOSAM 2022)*, Porto, Portugal, Dec. 2022
2. C. Pérez-Armenta, A. Ortega-Moñux, J. M. Luque-González, R. Halir, P. Reyes-Iglesias, J. H. Schmid, P. Cheben, Í. Molina-Fernández, and J. G. Wangüemert-Pérez, "Polarization-insensitive multimode interference coupler based on bricked subwavelength gratings," in *Photonics North 2022*, Niagara Falls, Canada, 24-26 May 2022
3. C. Pérez-Armenta, J. Čtyroký, P. Cheben, J. H. Schmid, A. Ortega-Moñux, R. Halir, Í. Molina-Fernández, and J. G. Wangüemert-Pérez, "A design methodology for resonant sensors based on subwavelength grating waveguides at 1.31 μm," in *OSA Optical Sensors and Sensing Congress*, Virtual Conference, Washington, DC, United States, 22-26 June 2020

National conference proceedings

1. C. Pérez-Armenta, A. Ortega-Moñux, J. M. Luque-González, R. Halir, J. Schmid, P. Cheben, I. Molina-Fernández, and J. G. Wangüemert-Pérez, "Demostración experimental de un acoplador de interferencia multimodal insensible a la polarización basado en un metamaterial sublongitud de onda," in *XIII Reunión Española de Optoelectrónica (OPTOEL 23)*, Sevilla, Spain, 14–16 June 2023
2. C. Pérez-Armenta, A. Ortega-Moñux, J. M. Luque-González, R. Halir, J. H. Schmid, P. Cheben, Í. Molina-Fernández, and J. G. Wangüemert-Pérez, "Dispositivos de interferencia multimodal 2×2 de banda ultraancha basados en estructuras periódicas sub-longitud de onda para las bandas o-e-s-c," in *XII Reunión Española de Optoelectrónica (OPTOEL 2021)*, Virtual Conference, Spain, 30 June - 2 July 2021
3. C. Pérez-Armenta, J. Čtyroký, A. Ortega-Moñux, P. Cheben, J. H. Schmid, R. Halir, Í. Molina-Fernández, and J. G. Wangüemert-Pérez, "Design of an ultra-narrowband subwavelength grating-based bragg filter for silicon photonics sensing in o-band,"

in *XXXV Simposio Nacional de la Unión Científica Internacional de Radio (URSI)*, Virtual Conference, Málaga, Spain, Feb. 2020

4. C. Pérez-Armenta, Í. Molina-Fernández, P. Cheben, J. Čtyroký, and J. G. Wangüemert-Pérez, "Ultra-narrowband subwavelength based bragg filter for silicon photonics biosensing," in *XXXIV Simposio Nacional de la Unión Científica Internacional de Radio (URSI)*, Sevilla, Spain, Apr. 2019

Awards

- Innova Scientific Best student paper award at XIII Reunión Española de Optoelectrónica (OPTOEL 23), 2023.
- ERICSSON award for the Best MSc Thesis in innovation for a Resposible Connected Society. Given by the Colegio Oficial de Ingenieros de Telecomunicación, 2021.
- Best MSc Thesis. Given by the Escuela Técnica superior de Ingeniería de Telecomunicación de la Universidad de Málaga, 2021.
- Best student record (MSc in Telecommunication Engineering). Given by the Escuela Técnica superior de Ingeniería de Telecomunicación de la Universidad de Málaga, 2021.
- Best student record (BSc in Telecommunication Engineering). Given by the Escuela Técnica superior de Ingeniería de Telecomunicación de la Universidad de Málaga, 2019.

Notorious participation in invited/keynote conferences (first three authors)

1. J. M. Luque-González, C. Pérez-Armenta, M. Barona-Ruiz, A. Fernández-Hinestrosa, J. G. Wangüemert-Pérez, J. Schmid, P. Cheben, R. Halir, Í. Molina-Fernández, and A. Ortega-Moñux, "Towards polarization-agnostic silicon photonic devices through swg metamaterial engineering," in *Photonics North*, Montreal, Canadá, Dec. 2023
2. J. G. Wangüemert-Pérez, C. Pérez-Armenta, P. Ginel-Moreno, J. M. Luque-González, A. H.-E. Houati, A. Sánchez-Postigo, J. de Oliva Rubio, A. Ortega-Moñux, R. Halir, J. H. Schmid, P. Cheben, and Í. Molina-Fernández, "Recent progress in subwavelength grating metamaterial engineered silicon photonic devices," in *Proc. SPIE PC12575, Integrated Optics: Design, Devices, Systems and Applications VII*, 31 May 2023, PC125750A
3. J. G. Wangüemert-Pérez, C. Pérez-Armenta, P. Ginel-Moreno, J. M. Luque-González, A. Hadij-ElHouati, A. Sánchez-Postigo, J. de-Oliva-Rubio, A. Ortega-Moñux, R. Halir, J. H. Schmid, P. Cheben, and Í. Molina-Fernández, "Bricked and evanescently-coupled topologies: Expanding the portfolio of subwavelength metamaterial silicon photonic devices," in *SPIE Photonics West*, San Francisco, USA, 28 Jan–02 Feb 2023

4. J. G. Wangüemert-Pérez, J. M. Luque-González, C. Pérez-Armenta, R. Halir, J. H. Schmid, M. Dado, J. Litvik, P. Cheben, I. Molina-Fernández, and A. Ortega-Moñux, "Bricked patterning: A new concept to enhance the capabilities of subwavelength grating waveguides," in *IEEE Group IV Photonics Conference*, Virtual Conference, Málaga, Spain, Jul. 2021

Bibliography

[1] S. E. Miller, "Integrated optics: An introduction," *Bell System Technical Journal*, vol. 48, no. 7, pp. 2059–2069, 1969. DOI: 10.1002/j.1538-7305.1969.tb01165.x.

[2] X. Liu, "Enabling optical network technologies for 5G and beyond," *Journal of Lightwave Technology*, vol. 40, no. 2, pp. 358–367, 2022. DOI: 10.1109/JLT.2021.3099726.

[3] J. Renaudier, A. Napoli, M. Ionescu, C. Calò, G. Fiol, V. Mikhailov, W. Forysiak, N. Fontaine, F. Poletti, and P. Poggiolini, "Devices and fibers for ultrawideband optical communications," *Proceedings of the IEEE*, vol. 110, no. 11, pp. 1742–1759, 2022. DOI: 10.1109/JPROC.2022.3203215.

[4] J. C. Ramirez, D. Grajales García, J. Maldonado, and A. Fernández-Gavela, "Current trends in photonic biosensors: Advances towards multiplexed integration," *Chemosensors*, vol. 10, no. 10, 2022. DOI: 10.3390/chemosensors10100398.

[5] J. C. Adcock, J. Bao, Y. Chi, X. Chen, D. Bacco, Q. Gong, L. K. Oxenløwe, J. Wang, and Y. Ding, "Advances in silicon quantum photonics," *IEEE Journal of Selected Topics in Quantum Electronics*, vol. 27, no. 2, pp. 1–24, 2021. DOI: 10.1109/JSTQE.2020.3025737.

[6] N. Li, C. P. Ho, J. Xue, L. W. Lim, G. Chen, Y. H. Fu, and L. Y. T. Lee, "A progress review on solid-state lidar and nanophotonics-based lidar sensors," *Laser & Photonics Reviews*, vol. 16, no. 11, p. 2 100 511, 2022. DOI: 10.1002/lpor.202100511.

[7] D. Zhu, L. Shao, M. Yu, R. Cheng, B. Desiatov, C. J. Xin, Y. Hu, J. Holzgrafe, S. Ghosh, A. Shams-Ansari, E. Puma, N. Sinclair, C. Reimer, M. Zhang, and M. Lončar, "Integrated photonics on thin-film lithium niobate," *Adv. Opt. Photon.*, vol. 13, no. 2, pp. 242–352, Jun. 2021. DOI: 10.1364/AOP.411024.

[8] G. C. Righini and A. Chiappini, "Glass optical waveguides: a review of fabrication techniques," *Optical Engineering*, vol. 53, no. 7, p. 071 819, 2014. DOI: 10.1117/1.OE.53.7.071819.

[9] K. Vyas, D. H. G. Espinosa, D. Hutama, S. K. Jain, R. Mahjoub, E. Mobini, K. M. Awan, J. Lundeen, and K. Dolgaleva, "Group III-V semiconductors as promising

nonlinear integrated photonic platforms," *Advances in Physics: X*, vol. 7, no. 1, p. 2 097 020, 2022. DOI: 10.1080/23746149.2022.2097020.

[10] Y. Intelligence. "Silicon photonics 2023." (), [Online]. Available: https://www.yolegroup.com/product/report/silicon-photonics-2023/.

[11] GlobalFoundries. "Globalfoundries announces next generation in silicon photonics solutions and collaborates with industry leaders to advance a new era of more in the data center | globalfoundries." (2024), [Online]. Available: https://gf.com/gf-press-release/globalfoundries-announces-next-generation-silicon-photonics-solutions-and/.

[12] C. Ting-Fang. "Tsmc bets on silicon photonics to enable more powerful chatgpt | financial times." (2024), [Online]. Available: https://www.ft.com/content/4e37f5b1-1364-4e35-a7bd-decb190e1bd3.

[13] A. Rahim, T. Spuesens, R. Baets, and W. Bogaerts, "Open-access silicon photonics: Current status and emerging initiatives," *Proceedings of the IEEE*, vol. 106, no. 12, pp. 2313–2330, 2018. DOI: 10.1109/JPROC.2018.2878686.

[14] S. Shekhar, W. Bogaerts, L. Chrostowski, J. E. Bowers, M. Hochberg, R. Soref, and B. J. Shastri, "Roadmapping the next generation of silicon photonics," *Nature Communications*, vol. 15, Jan. 2024. DOI: 10.1038/s41467-024-44750-0.

[15] A. H. Atabak, S. Moazeni, F. Pavanello, H. Gevorgyan, J. Notaros, L. Alloatti, M. T. Wade, C. Sun, S. A. Kruger, H. Meng, K. A. Qubaisi, I. Wang, B. Zhang, A. Khilo, C. V. Baiocco, M. A. Popovič, V. M. Stojanović, and R. J. Ram, "Integrating photonics with silicon nanoelectronics for the next generation of systems on a chip," *Nature*, vol. 556, pp. 349–354, Jun. 2018. DOI: 10.1038/s41586-018-0028-z.

[16] Applied Nanotools. "Nanosoi design center | applied nanotools inc." (2024), [Online]. Available: https://www.appliednt.com/nanosoi/sys/resources/specs/.

[17] S. Y. Siew, B. Li, F. Gao, H. Y. Zheng, W. Zhang, P. Guo, S. W. Xie, A. Song, B. Dong, L. W. Luo, C. Li, X. Luo, and G.-Q. Lo, "Review of Silicon Photonics Technology and Platform Development," *Journal of Lightwave Technology*, vol. 39, no. 13, pp. 4374–4389, 2021. DOI: 10.1109/JLT.2021.3066203.

[18] T. Tsuchizawa, K. Yamada, H. Fukuda, T. Watanabe, J.-i. Takahashi, M. Takahashi, T. Shoji, E. Tamechika, S. Itabashi, and H. Morita, "Microphotonics devices based on silicon microfabrication technology," *IEEE Journal of Selected Topics in Quantum Electronics*, vol. 11, no. 1, pp. 232–240, 2005. DOI: 10.1109/JSTQE.2004.841479.

[19] R. Halir, P. J. Bock, P. Cheben, A. Ortega-Moñux, C. Alonso-Ramos, J. H. Schmid, J. Lapointe, D.-X. Xu, J. G. Wangüemert-Pérez, Í. Molina-Fernández, and S. Janz, "Waveguide sub-wavelength structures: A review of principles and applications,"

Laser & Photonics Reviews, vol. 9, no. 1, pp. 25–49, 2015. DOI: 10.1002/lpor.201400083.

[20] P. Cheben, R. Halir, J. H. Schmid, H. A. Atwater, and D. R. Smith, "Subwavelength integrated photonics," *Nature*, vol. 560, no. 7720, pp. 565–572, Aug. 2018, ISSN: 0028-0836. DOI: 10.1038/s41586-018-0421-7.

[21] A. Sánchez-Postigo, R. Halir, J. G. Wangüemert-Pérez, A. Ortega-Moñux, S. Wang, M. Vachon, J. H. Schmid, D.-X. Xu, P. Cheben, and Í. Molina-Fernández, "Breaking the coupling efficiency-bandwidth trade-off in surface grating couplers using zero-order radiation," *Laser & Photonics Reviews*, vol. 15, no. 6, p. 2 000 542, 2021. DOI: 10.1002/lpor.202000542.

[22] P. Ginel-Moreno, A. Hadij-ElHouati, A. Sánchez-Postigo, J. G. Wangüemert-Pérez, Í. Molina-Fernández, J. H. Schmid, P. Cheben, and A. Ortega-Moñux, "On-chip metamaterial antenna array with distributed bragg deflector for generation of collimated steerable beams," *Laser & Photonics Reviews*, vol. 16, no. 9, p. 2 200 164, 2022. DOI: 10.1002/lpor.202200164.

[23] K. O. Hill, Y. Fujii, D. C. Johnson, and B. S. Kawasaki, "Photosensitivity in optical fiber waveguides: Application to reflection filter fabrication," *Applied Physics Letters*, vol. 32, no. 10, pp. 647–649, May 1978. DOI: 10.1063/1.89881.

[24] R. Kashyap, *Fiber Bragg Gratings*. Academic Press, 1999.

[25] K. Hill and G. Meltz, "Fiber bragg grating technology fundamentals and overview," *Journal of Lightwave Technology*, vol. 15, no. 8, pp. 1263–1276, 1997. DOI: 10.1109/50.618320.

[26] P. Cheben, D.-X. Xu, S. Janz, and A. Densmore, "Subwavelength waveguide grating for mode conversion and light coupling in integrated optics," *Opt. Express*, vol. 14, no. 11, pp. 4695–4702, May 2006. DOI: 10.1364/OE.14.004695.

[27] S.-H. Yang, M. L. Cooper, P. R. Bandaru, and S. Mookherjea, "Giant birefringence in multi-slotted silicon nanophotonic waveguides," *Opt. Express*, vol. 16, no. 11, pp. 8306–8316, May 2008. DOI: 10.1364/OE.16.008306.

[28] J. M. Luque-González, A. Herrero-Bermello, A. Ortega-Moñux, Í. Molina-Fernández, A. V. Velasco, P. Cheben, J. H. Schmid, S. Wang, and R. Halir, "Tilted subwavelength gratings: Controlling anisotropy in metamaterial nanophotonic waveguides," *Opt. Lett.*, vol. 43, no. 19, pp. 4691–4694, Oct. 2018. DOI: 10.1364/OL.43.004691.

[29] C.-J. Chung, X. Xu, G. Wang, Z. Pan, and R. T. Chen, "On-chip optical true time delay lines featuring one-dimensional fishbone photonic crystal waveguide," *Applied Physics Letters*, vol. 112, no. 7, p. 071 104, Feb. 2018. DOI: 10.1063/1.5006188.

[30] E. Luan, H. Yun, L. Laplatine, Y. Dattner, D. M. Ratner, K. C. Cheung, and L. Chrostowski, "Enhanced Sensitivity of Subwavelength Multibox Waveguide Microring Resonator Label-Free Biosensors," *IEEE Journal of Selected Topics in*

Quantum Electronics, vol. 25, no. 3, p. 1, 2019. DOI: 10.1109/JSTQE.2018.2821842.

[31] J. M. Luque-González, A. Ortega-Moñux, R. Halir, J. H. Schmid, P. Cheben, Í. Molina-Fernández, and J. G. Wangüemert-Pérez, "Bricked Subwavelength Gratings: A Tailorable On-Chip Metamaterial Topology," *Laser & Photonics Reviews*, vol. 15, no. 6, p. 2 000 478, 2021. DOI: https://doi.org/10.1002/lpor.202000478.

[32] J. M. Luque-González, A. Sánchez-Postigo, A. Hadij-ElHouati, A. Ortega-Moñux, J. G. Wangüemert-Pérez, J. H. Schmid, P. Cheben, Í. Molina-Fernández, and R. Halir, "A review of silicon subwavelength gratings: Building break-through devices with anisotropic metamaterials," *Nanophotonics*, vol. 10, no. 11, pp. 2765–2797, 2021. DOI: 10.1515/nanoph-2021-0110.

[33] P. Cheben, J. H. Schmid, R. Halir, J. M. Luque-González, J. G. Wangüemert-Pérez, D. Melati, and C. Alonso-Ramos, "Recent advances in metamaterial integrated photonics," *Adv. Opt. Photon.*, vol. 15, no. 4, pp. 1033–1105, Dec. 2023. DOI: 10.1364/AOP.495828.

[34] P. Cheben, S. Janz, D.-X. Xu, B. Lamontagne, A. Delage, and S. Tanev, "A broadband waveguide grating coupler with a subwavelength grating mirror," *IEEE Photonics Technology Letters*, vol. 18, no. 1, pp. 13–15, 2006. DOI: 10.1109/LPT.2005.860037.

[35] P. Cheben, J. H. Schmid, S. Wang, D.-X. Xu, M. Vachon, S. Janz, J. Lapointe, Y. Painchaud, and M.-J. Picard, "Broadband polarization independent nanophotonic coupler for silicon waveguides with ultra-high efficiency," *Opt. Express*, vol. 23, no. 17, pp. 22 553–22 563, Aug. 2015. DOI: 10.1364/OE.23.022553.

[36] D. Benedikovic, C. Alonso-Ramos, S. Guerber, X. L. Roux, P. Cheben, C. Dupré, B. Szelag, D. Fowler, É. Cassan, D. Marris-Morini, C. Baudot, F. Boeuf, and L. Vivien, "Sub-decibel silicon grating couplers based on l-shaped waveguides and engineered subwavelength metamaterials," *Opt. Express*, vol. 27, no. 18, pp. 26 239–26 250, Sep. 2019. DOI: 10.1364/OE.27.026239.

[37] Z. Wang, X. Xu, D. Fan, Y. Wang, and R. T. Chen, "High quality factor subwavelength grating waveguide micro-ring resonator based on trapezoidal silicon pillars," *Opt. Lett.*, vol. 41, no. 14, pp. 3375–3378, Jul. 2016. DOI: 10.1364/OL.41.003375.

[38] R. Fernández de Cabo, J. Vilas, P. Cheben, A. V. Velasco, and D. González-Andrade, "Experimental characterization of an ultra-broadband dual-mode symmetric y–junction based on metamaterial waveguides," *Optics & Laser Technology*, vol. 157, p. 108 742, 2023, ISSN: 0030-3992. DOI: 10.1016/j.optlastec.2022.108742.

[39] D. González-Andrade, I. Olivares, R. Fernández de Cabo, J. Vilas, A. Dias, and A. V. Velasco, "Broadband three-mode converter and multiplexer based on cascaded

symmetric y-junctions and subwavelength engineered mmi and phase shifters," *Optics & Laser Technology*, vol. 164, p. 109 513, 2023, ISSN: 0030-3992. DOI: 10.1016/j.optlastec.2023.109513.

[40] H. Xu, D. Dai, and Y. Shi, "Ultra-broadband and ultra-compact on-chip silicon polarization beam splitter by using hetero-anisotropic metamaterials," *Laser & Photonics Reviews*, vol. 13, no. 4, p. 1 800 349, 2019. DOI: 10.1002/lpor.201800349.

[41] M. Ma, A. H. K. Park, Y. Wang, H. Shoman, F. Zhang, N. A. F. Jaeger, and L. Chrostowski, "Sub-wavelength grating-assisted polarization splitter-rotators for silicon-on-insulator platforms," *Opt. Express*, vol. 27, no. 13, pp. 17 581–17 591, Jun. 2019. DOI: 10.1364/OE.27.017581.

[42] L. Torrijos-Morán, D. Pérez-Galacho, and D. Pérez-López, "Silicon programmable photonic circuits based on periodic bimodal waveguides," *Laser & Photonics Reviews*, vol. 18, no. 1, p. 2 300 505, 2024. DOI: 10.1002/lpor.202300505.

[43] R. Halir, P. Cheben, J. M. Luque-González, J. D. Sarmiento-Merenguel, J. H. Schmid, J. G. Wangüemert-Pérez, D.-X. Xu, S. Wang, A. Ortega-Moñux, and Í. Molina-Fernández, "Ultra-broadband nanophotonic beamsplitter using an anisotropic sub-wavelength metamaterial," *Laser & Photonics Reviews*, vol. 10, no. 6, pp. 1039–1046, 2016. DOI: https://doi.org/10.1002/lpor.201600213.

[44] A. Herrero-Bermello, J. M. Luque-González, A. V. Velasco, A. Ortega-Moñux, P. Cheben, and R. Halir, "Design of a broadband polarization splitter based on anisotropy-engineered tilted subwavelength gratings," *IEEE Photonics Journal*, vol. 11, no. 3, pp. 1–8, 2019. DOI: 10.1109/JPHOT.2019.2912335.

[45] W. Zhong and J. Xiao, "Ultracompact polarization-insensitive power splitter using subwavelength-grating-based MMI couplers on an SOI platform," *Appl. Opt.*, vol. 59, no. 7, pp. 1991–1997, Mar. 2020. DOI: 10.1364/AO.382097.

[46] A. Herrero-Bermello, J. M. Luque-González, R. Halir, P. Cheben, A. Ortega-Moñux, I. Molina-Fernández, and A. V. Velasco, "Zero-Birefringence Silicon Waveguides Based on Tilted Subwavelength Metamaterials," *IEEE Photonics Journal*, vol. 11, no. 5, p. 2 700 308, 2019. DOI: 10.1109/JPHOT.2019.2942973.

[47] J. Guo, L. Yu, H. Xiang, Y. Zhao, C. Liu, and D. Dai, "Realization of advanced passive silicon photonic devices with subwavelength grating structures developed by efficient inverse design," *Advanced Photonics Nexus*, vol. 2, no. 2, p. 026 005, 2023. DOI: 10.1117/1.APN.2.2.026005.

[48] D. Dai, L. Liu, S. Gao, D.-X. Xu, and S. He, "Polarization management for silicon photonic integrated circuits," *Laser & Photonics Reviews*, vol. 7, no. 3, pp. 303–328, 2013. DOI: 10.1002/lpor.201200023.

[49] S. T. Lim, C. E. Png, E. A. Ong, and Y. L. Ang, "Single mode, polarization-independent submicron silicon waveguides based on geometrical adjustments,"

Opt. Express, vol. 15, no. 18, pp. 11 061–11 072, Sep. 2007. DOI: 10.1364/OE.15.011061.

[50] T. Barwicz, M. R. Watts, M. A. Popović, P. T. Rakich, L. Socci, F. X. Kärtner, E. P. Ippen, and H. I. Smith, "Polarization-transparent microphotonic devices in the strong confinement limit," *Nature Photonics*, vol. 1, no. 1, pp. 57–60, Jan. 2007. DOI: 10.1038/nphoton.2006.41.

[51] X. Chen, W. Liu, Y. Zhang, and Y. Shi, "Polarization-insensitive broadband 2 × 2 3 dB power splitter based on silicon-bent directional couplers," *Opt. Lett.*, vol. 42, no. 19, pp. 3738–3740, Oct. 2017. DOI: 10.1364/OL.42.003738.

[52] Y. Wang, L. Xu, H. Yun, M. Ma, A. Kumar, E. El-Fiky, R. Li, N. Abadía, L. Chrostowski, N. A. F. Jaeger, and D. V. Plant, "Polarization-Independent Mode-Evolution-Based Coupler for the Silicon-on-Insulator Platform," *IEEE Photonics Journal*, vol. 10, no. 3, p. 4 900 410, 2018. DOI: 10.1109/JPHOT.2018.2835767.

[53] H. Li, W. Chen, P. Wang, S. Dai, Y. Liu, Q. Fu, J. Li, Y. Li, T. Dai, H. Yu, and J. Yang, "Compact and low-loss 1 × 3 polarization-insensitive optical power splitter using cascaded tapered silicon waveguides," *Opt. Lett.*, vol. 45, no. 19, pp. 5596–5599, Oct. 2020. DOI: 10.1364/OL.401036.

[54] D. González-Andrade, C. Lafforgue, E. Durán-Valdeiglesias, X. Le Roux, M. Berciano, E. Cassan, D. Marris-Morini, A. V. Velasco, P. Cheben, L. Vivien, and C. Alonso-Ramos, "Polarization- and wavelength-agnostic nanophotonic beam splitter," *Scientific Reports*, vol. 9, no. 1, p. 3604, Dec. 2019, ISSN: 2045-2322. DOI: 10.1038/s41598-019-40497-7.

[55] H. Yun, L. Chrostowski, and N. A. F. Jaeger, "Narrow-band, polarization-independent, transmission filter in a silicon-on-insulator strip waveguide," *Opt. Lett.*, vol. 44, no. 4, pp. 847–850, Feb. 2019. DOI: 10.1364/OL.44.000847.

[56] L. Soldano and E. Pennings, "Optical multi-mode interference devices based on self-imaging: Principles and applications," *Journal of Lightwave Technology*, vol. 13, no. 4, pp. 615–627, 1995. DOI: 10.1109/50.372474.

[57] H. Guan, Y. Ma, R. Shi, X. Zhu, R. Younce, Y. Chen, J. Roman, N. Ophir, Y. Liu, R. Ding, T. Baehr-Jones, K. Bergman, and M. Hochberg, "Compact and low loss 90°; optical hybrid on a silicon-on-insulator platform," *Opt. Express*, vol. 25, no. 23, pp. 28 957–28 968, Nov. 2017. DOI: 10.1364/OE.25.028957.

[58] D. Dai and S. He, "Optimization of Ultracompact Polarization-Insensitive Multimode Interference Couplers Based on Si Nanowire Waveguides," *IEEE Photonics Technology Letters*, vol. 18, no. 19, pp. 2017–2019, 2006. DOI: 10.1109/LPT.2006.882227.

[59] H. Xie, J. Zheng, P. Xu, J. Yao, J. Whitehead, and A. Majumdar, "Ultra-Compact Subwavelength-Grating-Assisted Polarization-Independent Directional Coupler," *IEEE Photonics Technology Letters*, vol. 31, no. 18, pp. 1538–1541, 2019. DOI: 10.1109/LPT.2019.2937890.

[60] N. Yang and J. Xiao, "A compact silicon-based polarization-independent power splitter using a three-guide directional coupler with subwavelength gratings," *Optics Communications*, vol. 459, p. 125 095, 2020, ISSN: 0030–4018. DOI: 10.1016/j.optcom.2019.125095.

[61] X. Jiang and D. Dai, "Compact, Broadband, and Polarization-insensitive 3 dB power splitter on silicon," in *2018 Asia Communications and Photonics Conference (ACP)*, 2018. DOI: 10.1109/ACP.2018.8595913.

[62] T. Hao, A. Sánchez-Postigo, P. Cheben, A. Ortega-Moñux, and W. N. Ye, "Dual-band polarization-independent subwavelength grating coupler for wavelength demultiplexing," *IEEE Photonics Technology Letters*, vol. 32, no. 18, pp. 1163–1166, 2020. DOI: 10.1109/LPT.2020.3014640.

[63] C. Pérez-Armenta, A. Ortega-Moñux, J. M. Luque-González, R. Halir, P. J. Reyes-Iglesias, J. Schmid, P. Cheben, Í. Molina-Fernández, and J. G. Wangüemert-Pérez, "Polarization-independent multimode interference coupler with anisotropy-engineered bricked metamaterial," *Photon. Res.*, vol. 10, no. 4, A57–A65, Apr. 2022. DOI: 10.1364/PRJ.446932.

[64] C. Pérez-Armenta, A. Ortega-Moñux, J. M. Luque-González, R. Halir, J. Schmid, P. Cheben, I. Molina-Fernández, and J. G. Wangüemert-Pérez, "Polarization insensitive metamaterial engineered multimode interference coupler in a 220 nm silicon-on-insulator platform," *Optics & Laser Technology*, vol. 164, p. 109 493, Apr. 2023. DOI: 10.1016/j.optlastec.2023.109493.

[65] T. Murphy, J. Hastings, and H. Smith, "Fabrication and characterization of narrow-band bragg-reflection filters in silicon-on-insulator ridge waveguides," *Journal of Lightwave Technology*, vol. 19, no. 12, pp. 1938–1942, 2001. DOI: 10.1109/50.971688.

[66] X. Wang, "Silicon Photonic Waveguide Bragg Gratings," Ph.D. dissertation, University of British Columbia, 2013.

[67] X. Wang, W. Shi, R. Vafaei, N. A. F. Jaeger, and L. Chrostowski, "Uniform and sampled bragg gratings in soi strip waveguides with sidewall corrugations," *IEEE Photonics Technology Letters*, vol. 23, no. 5, pp. 290–292, 2011. DOI: 10.1109/LPT.2010.2103305.

[68] D. T. H. Tan, K. Ikeda, and Y. Fainman, "Cladding-modulated bragg gratings in silicon waveguides," *Opt. Lett.*, vol. 34, no. 9, pp. 1357–1359, May 2009. DOI: 10.1364/OL.34.001357.

[69] J. Čtyroký, J. G. Wangüemert-Pérez, P. Kwiecien, I. Richter, J. Litvik, J. H. Schmid, Í. Molina-Fernández, A. Ortega-Moñux, M. Dado, and P. Cheben, "Design of narrowband Bragg spectral filters in subwavelength grating metamaterial waveguides," *Opt. Express*, vol. 26, no. 1, pp. 179–194, 2018. DOI: 10.1364/OE.26.000179.

[70] P. Cheben, J. Čtyroký, J. H. Schmid, S. Wang, J. Lapointe, J. G. Wangüemert-Pérez, Í. Molina-Fernández, A. Ortega-Moñux, R. Halir, D. Melati, D. Xu, S. Janz, and M. Dado, "Bragg filter bandwidth engineering in subwavelength grating metamaterial waveguides," *Opt. Lett.*, vol. 44, no. 4, pp. 1043–1046, Feb. 2019. DOI: 10.1364/OL.44.001043.

[71] D. Pereira-Martín, J. M. Luque-González, J. G. Wangüemert-Pérez, A. Hadij-ElHouati, Í. Molina-Fernández, P. Cheben, J. H. Schmid, S. Wang, W. N. Ye, J. Čtyroký, and A. Ortega-Moñux, "Complex spectral filters in silicon waveguides based on cladding-modulated bragg gratings," *Opt. Express*, vol. 29, no. 11, pp. 15 867–15 881, May 2021. DOI: 10.1364/OE.420696.

[72] E. Luan, H. Shoman, D. M. Ratner, K. C. Cheung, and L. Chrostowski, "Silicon photonic biosensors using label-free detection," *Sensors*, vol. 18, no. 10, 2018. DOI: 10.3390/s18103519.

[73] M. C. Estevez, M. Alvarez, and L. M. Lechuga, "Integrated optical devices for lab-on-a-chip biosensing applications," *Laser & Photonics Reviews*, vol. 6, no. 4, pp. 463–487, 2012.

[74] Genalyte, Inc. "Maverick - Genalyte." (2024), [Online]. Available: https://www.genalyte.com/home/maverick/.

[75] Bioherent, S.L. "Bioherent." (2024), [Online]. Available: https://bioherent.com/.

[76] R. G. Heidemann, R. P. H. Kooyman, and J. Greve, "Development of an optical waveguide interferometric immunosensor," *Sensors and Actuators B: Chemical*, vol. 4, no. 3-4, pp. 297–299, 1991. DOI: 10.1016/0925-4005(91)80126-5.

[77] R. G. Heidemann, R. P. H. Kooyman, and J. Greve, "Performance of a highly sensitive optical waveguide mach-zehnder interferometer immunosensor," *Sensors and Actuators B: Chemical*, vol. 10, no. 3, pp. 209–217, 1993. DOI: 10.1016/0925-4005(93)87008-D.

[78] K. E. Zinoviev, A. B. Gonzalez-Guerrero, C. Dominguez, and L. M. Lechuga, "Integrated bimodal waveguide interferometric biosensor for label-free analysis," *Journal of Lightwave Technology*, vol. 29, no. 13, pp. 1926–1930, 2011. DOI: 10.1109/JLT.2011.2150734.

[79] R. Halir, L. Vivien, X. Le Roux, D.-X. Xu, and P. Cheben, "Direct and sensitive phase readout for integrated waveguide sensors," *IEEE Photonics Journal*, vol. 5, no. 4, p. 6 800 906, 2013. DOI: 10.1109/JPHOT.2013.2276747.

[80] J. Leuermann, V. Stamenkovic, P. Ramirez-Priego, A. Sánchez-Postigo, A. Fernández-Gavela, C. A. Chapman, R. C. Bailey, L. M. Lechuga, E. Perez-Inestrosa, D. Collado, R. Halir, and Í. Molina-Fernández, "Coherent silicon photonic interferometric biosensor with an inexpensive laser source for sensitive label-free immunoassays," *Opt. Lett.*, vol. 45, no. 24, pp. 6595–6598, Dec. 2020. DOI: 10.1364/OL.411635.

[81] K. D. Vos, "Label-free Silicon Photonics Biosensor Platform with Microring Resonators," Ph.D. dissertation, Universiteit Gent, 2010.

[82] S. Janz, D.-X. Xu, M. Vachon, N. Sabourin, P. Cheben, H. McIntosh, H. Ding, S. Wang, J. H. Schmid, A. Delâge, J. Lapointe, A. Densmore, R. Ma, W. Sinclair, S. M. Logan, R. MacKenzie, Q. Y. Liu, D. Zhang, G. Lopinski, O. Mozenson, M. Gilmour, and H. Tabor, "Photonic wire biosensor microarray chip and instrumentation with application to serotyping of Escherichia coliisolates," *Opt. Express*, vol. 21, no. 4, pp. 4623–4637, Feb. 2013.

[83] T. Claes, J. G. Molera, K. D. Vos, E. Schacht, R. Baets, and P. Bienstman, "Label-Free Biosensing With a Slot-Waveguide-Based Ring Resonator in Silicon on Insulator," *IEEE Photonics Journal*, vol. 1, no. 3, pp. 197–204, Sep. 2009. DOI: 10.1109/JPHOT.2009.2031596.

[84] J. G. Wangüemert-Pérez, P. Cheben, A. Ortega-Moñux, C. Alonso-Ramos, D. Pérez-Galacho, R. Halir, Í. Molina-Fernández, D.-X. Xu, and J. H. Schmid, "Evanescent field waveguide sensing with subwavelength grating structures in silicon-on-insulator," *Opt. Lett.*, vol. 39, no. 15, pp. 4442–4445, 2014. DOI: 10.1364/OL.39.004442.

[85] V. Donzella, A. Sherwali, J. Flueckiger, S. M. Grist, S. T. Fard, and L. Chrostowski, "Design and fabrication of SOI micro-ring resonators based on sub-wavelength grating waveguides," *Opt. Express*, vol. 23, no. 4, pp. 4791–4803, Feb. 2015.

[86] J. Flueckiger, S. Schmidt, V. Donzella, A. Sherwali, D. M. Ratner, L. Chrostowski, and K. C. Cheung, "Sub-wavelength grating for enhanced ring resonator biosensor," *Opt. Express*, vol. 24, no. 14, pp. 15 672–15 686, Jul. 2016.

[87] H. Yan, L. Huang, X. Xu, S. Chakravarty, N. Tang, H. Tian, and R. T. Chen, "Unique surface sensing property and enhanced sensitivity in microring resonator biosensors based on subwavelength grating waveguides," *Optics Express*, vol. 24, no. 26, p. 29 724, 2016. DOI: 10.1364/oe.24.029724.

[88] L. Huang, H. Yan, X. Xu, S. Chakravarty, N. Tang, H. Tian, and R. T. Chen, "Improving the detection limit for on-chip photonic sensors based on subwavelength grating racetrack resonators," *Optics Express*, vol. 25, no. 9, p. 10 527, May 2017. DOI: 10.1364/oe.25.010527.

[89] E. Luan, H. Yun, L. Laplatine, Y. Dattner, D. M. Ratner, K. C. Cheung, and L. Chrostowski, "Enhanced Sensitivity of Subwavelength Multibox Waveguide Microring Resonator Label-Free Biosensors," *IEEE Journal of Selected Topics in Quantum Electronics*, vol. 25, no. 3, p. 1, 2019. DOI: 10.1109/JSTQE.2018.2821842.

[90] E. Luan, H. Yun, M. Ma, D. M. Ratner, K. C. Cheung, and L. Chrostowski, "Label-free biosensing with a multi-box sub-wavelength phase-shifted Bragg grating waveguide," *Biomed. Opt. Express*, vol. 10, no. 9, pp. 4825–4838, Sep. 2019. DOI: 10.1364/BOE.10.004825.

[91] L. Torrijos-Morán, A. Griol, and J. García-Rupérez, "Experimental study of subwavelength grating bimodal waveguides as ultrasensitive interferometric sensors," *Opt. Lett.*, vol. 44, no. 19, pp. 4702–4705, Oct. 2019. DOI: 10.1364/OL.44.004702.

[92] C. Pérez-Armenta, A. Ortega-Moñux, J. Čtyroký, P. Cheben, J. H. Schmid, R. Halir, Í. Molina-Fernández, and J. G. Wangüemert-Pérez, "Narrowband bragg filters based on subwavelength grating waveguides for silicon photonic sensing," *Opt. Express*, vol. 28, no. 25, pp. 37 971–37 985, Dec. 2020. DOI: 10.1364/OE.404364.

[93] W. Zhang and J. Yao, "A fully reconfigurable waveguide Bragg grating for programmable photonic signal processing," *Nature Communications*, vol. 9, no. 1, p. 1396, Apr. 2018. DOI: 10.1038/s41467-018-03738-3.

[94] S. H. Badri and S. G. Farkoush, "Subwavelength grating waveguide filter based on cladding modulation with a phase-change material grating," *Appl. Opt.*, vol. 60, no. 10, pp. 2803–2810, Apr. 2021. DOI: 10.1364/AO.419587.

[95] M. Khalil, H. Sun, E. Berikaa, D. V. Plant, and L. R. Chen, "Electrically reconfigurable waveguide bragg grating filters," *Opt. Express*, vol. 30, no. 22, pp. 39 643–39 651, Oct. 2022. DOI: 10.1364/OE.473018.

[96] A. Ahuja, P. Steinvurzel, B. Eggleton, and J. Rogers, "Tunable single phase-shifted and superstructure gratings using microfabricated on-fiber thin film heaters," *Optics Communications*, vol. 184, no. 1, pp. 119–125, 2000, ISSN: 0030-4018. DOI: 10.1016/S0030-4018(00)00923-8.

[97] Z. Wang and L. R. Chen, "A Thermally Tunable Superstructure Grating Filter in Silicon Photonics," in *2018 IEEE Photonics Conference (IPC)*, Reston, VA: IEEE, Sep. 2018, pp. 1–2. DOI: 10.1109/IPCon.2018.8527163.

[98] C. Pérez-Armenta, K. K. MacKay, A. Hadij-ElHouati, A. Ortega-Moñux, I. Molina-Fernández, J. G. Wangüemert-Pérez, J. H. Schmid, P. Cheben, and W. N. Ye, "Thermally induced sideband generation in silicon-on-insulator cladding modulated bragg notch filters," *Opt. Express*, vol. 31, no. 13, pp. 22 225–22 232, Jun. 2023. DOI: 10.1364/OE.488108.

[99] W. Bogaerts and L. Chrostowski, "Silicon photonics circuit design: Methods, tools and challenges," *Laser & Photonics Reviews*, vol. 12, no. 4, p. 1 700 237, 2018. DOI: https://doi.org/10.1002/lpor.201700237.

[100] S. Molesky, Z. Lin, A. Y. Piggott, W. Jin, J. Vucković, and A. W. Rodriguez, "Inverse design in nanophotonics," *Nature Photonics*, vol. 12, no. 11, pp. 659–670, Nov. 2018. DOI: 10.1038/s41566-018-0246-9.

[101] T. Zhu, Y. Hu, P. Gatkine, S. Veilleux, J. Bland-Hawthorn, and M. Dagenais, "Arbitrary on-chip optical filter using complex waveguide bragg gratings," *Applied Physics Letters*, vol. 108, no. 10, p. 101 104, Mar. 2016, ISSN: 0003-6951. DOI: 10.1063/1.4943551.

[102] S. G. Johnson and J. D. Joannopoulos, "Block-iterative frequency-domain methods for Maxwell's equations in a planewave basis," *Opt. Express*, vol. 8, no. 3, pp. 173–190, Jan. 2001. DOI: 10.1364/OE.8.000173.

[103] MPB developers. "Manual - mpb documentation." (2024), [Online]. Available: https://mpb.readthedocs.io/en/latest/.

[104] A. F. Oskooi, D. Roundy, M. Ibanescu, P. Bermel, J. Joannopoulos, and S. G. Johnson, "Meep: A flexible free-software package for electromagnetic simulations by the FDTD method," *Computer Physics Communications*, vol. 181, no. 3, pp. 687–702, 2010, ISSN: 0010-4655. DOI: 10.1016/j.cpc.2009.11.008.

[105] Meep developers. "Meep documentation." (2024), [Online]. Available: https://meep.readthedocs.io/en/latest/.

[106] R. Broeke, X. Leijtens, K. Ławniczuk, K. Rylander, and V. Moskalenko. "Homepage – nazca design." (2024), [Online]. Available: https://nazca-design.org/.

[107] The Git community. "Git." (2024), [Online]. Available: https://git-scm.com.

[108] S. D. Campbell, D. Sell, R. P. Jenkins, E. B. Whiting, J. A. Fan, and D. H. Werner, "Review of numerical optimization techniques for meta-device design [Invited]," *Opt. Mater. Express*, vol. 9, no. 4, pp. 1842–1863, Apr. 2019. DOI: 10.1364/OME.9.001842.

[109] J. Nocedal and S. J. Wright, *Numerical Optimization*. Springer, 2006.

[110] K. Svanberg, "A class of globally convergent optimization methods based on conservative convex separable approximations," *SIAM Journal on Optimization*, vol. 12, no. 2, pp. 555–573, 2002. DOI: 10.1137/S1052623499362822.

[111] J. Jensen and O. Sigmund, "Topology optimization for nano-photonics," *Laser & Photonics Reviews*, vol. 5, no. 2, pp. 308–321, 2011. DOI: 10.1002/lpor.201000014.

[112] C. M. Lalau-Keraly, S. Bhargava, O. D. Miller, and E. Yablonovitch, "Adjoint shape optimization applied to electromagnetic design," *Opt. Express*, vol. 21, no. 18, pp. 21 693–21 701, Sep. 2013. DOI: 10.1364/OE.21.021693.

[113] A. Y. Piggott, J. Lu, K. G. Lagoudakis, J. Petykiewicz, T. M. Babinec, and J. Vučković, "Inverse design and demonstration of a compact and broadband on-chip wavelength demultiplexer," *Nature Photonics*, vol. 9, no. 6, pp. 374–377, Jun. 2015, ISSN: 1749-4885, 1749-4893. DOI: 10.1038/nphoton.2015.69.

[114] A. M. Hammond, A. Oskooi, M. Chen, Z. Lin, S. G. Johnson, and S. E. Ralph, "High-performance hybrid time/frequency-domain topology optimization for large-scale photonics inverse design," *Opt. Express*, vol. 30, no. 3, pp. 4467–4491, Jan. 2022. DOI: 10.1364/OE.442074.

[115] D. E. Goldberg, *Genetic Algorithms*. Addison-Wesley, 1989.

[116] S. Jafar-Zanjani, S. Inampudi, and H. Mosallaei, "Adaptive Genetic Algorithm for Optical Metasurfaces Design," *Scientific Reports*, vol. 8, no. 1, p. 11 040, Jul. 2018. DOI: 10.1038/s41598-018-29275-z. (visited on 03/21/2024).

[117] S. Khajavi, D. Melati, P. Cheben, J. H. Schmid, C. A. A. Ramos, and W. N. Ye, "Highly efficient ultra-broad beam silicon nanophotonic antenna based on near-field phase engineering," *Scientific Reports*, vol. 12, no. 1, p. 18 808, Nov. 2022, ISSN: 2045-2322. DOI: 10.1038/s41598-022-23460-x.

[118] N. Jin and Y. Rahmat-Samii, "Advances in particle swarm optimization for antenna designs: Real-number, binary, single-objective and multiobjective implementations," *IEEE Transactions on Antennas and Propagation*, vol. 55, no. 3, pp. 556–567, 2007. DOI: 10.1109/TAP.2007.891552.

[119] Q. Lu, W. Wei, X. Yan, B. Shen, Y. Luo, X. Zhang, and X. Ren, "Particle swarm optimized ultra-compact polarization beam splitter on silicon-on-insulator," *Photonics and Nanostructures - Fundamentals and Applications*, vol. 32, pp. 19–23, 2018, ISSN: 1569-4410. DOI: 10.1016/j.photonics.2018.08.006.

[120] W. Chen, B. Zhang, P. Wang, S. Dai, W. Liang, H. Li, Q. Fu, J. Li, Y. Li, T. Dai, H. Yu, and J. Yang, "Ultra-compact and low-loss silicon polarization beam splitter using a particle-swarm-optimized counter-tapered coupler," *Opt. Express*, vol. 28, no. 21, pp. 30 701–30 709, Oct. 2020. DOI: 10.1364/OE.408432.

[121] R. Shiratori, M. Nakata, K. Hayashi, and T. Baba, "Particle swarm optimization of silicon photonic crystal waveguide transition," *Opt. Lett.*, vol. 46, no. 8, pp. 1904–1907, Apr. 2021. DOI: 10.1364/OL.422551.

[122] J. Kim, J.-Y. Kim, J. Yoon, H. Yoon, H.-H. Park, and H. Kurt, "Experimental demonstration of inverse-designed silicon integrated photonic power splitters," *Nanophotonics*, vol. 11, no. 20, pp. 4581–4590, 2022. DOI: 10.1515/nanoph-2022-0443.

[123] N. Hansen, S. D. Müller, and P. Koumoutsakos, "Reducing the time complexity of the derandomized evolution strategy with covariance matrix adaptation (cma-es)," *Evolutionary Computation*, vol. 11, no. 1, pp. 1–18, Mar. 2003. DOI: 10.1162/106365603321828970.

[124] Y. Miyatake, N. Sekine, K. Toprasertpong, S. Takagi, and M. Takenaka, "Computational design of efficient grating couplers using artificial intelligence," *Japanese Journal of Applied Physics*, vol. 59, no. SG, SGGE09, Mar. 2020. DOI: 10.7567/1347-4065/ab641c.

[125] K. Takahashi and T. Baba, "Optimization of a photonic crystal nanocavity using covariance matrix adaptation evolution strategy," *IEEE Photonics Journal*, vol. 14, no. 3, 2022. DOI: 10.1109/JPHOT.2022.3168543.

[126] Y. Miyatake, K. Toprasertpong, S. Takagi, and M. Takenaka, "Design of compact and low-loss s-bends by cma-es," *Opt. Express*, vol. 31, no. 26, pp. 43 850–43 863, Dec. 2023. DOI: 10.1364/OE.504866.

[127] L. Yu, J. Guo, H. Xiang, C. Liu, Y. Zhao, and D. Dai, "High-performance 2 × 2 bent directional couplers designed with an efficient semi-inverse design method,"

Journal of Lightwave Technology, vol. 42, no. 2, pp. 740–747, 2024. DOI: 10.1109/JLT.2023.3315214.

[128] J. Park, S. Kim, D. W. Nam, H. Chung, C. Y. Park, and M. S. Jang, "Free-form optimization of nanophotonic devices: From classical methods to deep learning," *Nanophotonics*, vol. 11, no. 9, pp. 1809–1845, May 2022, ISSN: 2192-8614. DOI: 10.1515/nanoph-2021-0713.

[129] H. Xu, Y. Qin, G. Hu, and H. K. Tsang, "Million-q integrated fabry-perot cavity using ultralow-loss multimode retroreflectors," *Photon. Res.*, vol. 10, no. 11, pp. 2549–2559, Nov. 2022. DOI: 10.1364/PRJ.470644.

[130] H. Xu, D. Dai, and Y. Shi, "Ultra-broadband on-chip multimode power splitter with an arbitrary splitting ratio," *OSA Continuum*, vol. 3, no. 5, pp. 1212–1221, May 2020. DOI: 10.1364/OSAC.396024.

[131] W. Zhao, X. Yi, Y. Peng, L. Zhang, H. Chen, and D. Dai, "Silicon multimode waveguide crossing based on anisotropic subwavelength gratings," *Laser & Photonics Reviews*, vol. 16, no. 6, p. 2 100 623, 2022. DOI: 10.1002/lpor.202100623.

[132] J. M. Luque-González, R. Halir, J. G. Wangüemert-Pérez, J. de-Oliva-Rubio, J. H. Schmid, P. Cheben, Í. Molina-Fernández, and A. Ortega-Moñux, "An ultracompact grin-lens-based spot size converter using subwavelength grating metamaterials," *Laser & Photonics Reviews*, vol. 13, no. 11, p. 1 900 172, 2019. DOI: 10.1002/lpor.201900172.

[133] Y. Zhang, Y. He, H. Wang, L. Sun, and Y. Su, "Ultra-broadband mode size converter using on-chip metamaterial-based luneburg lens," *ACS Photonics*, vol. 8, no. 1, pp. 202–208, 2021. DOI: 10.1021/acsphotonics.0c01269.

[134] H. Xu, Y. Qin, G. Hu, and H. K. Tsang, "Compact integrated mode-size converter using a broadband ultralow-loss parabolic-mirror collimator," *Opt. Lett.*, vol. 48, no. 2, pp. 327–330, Jan. 2023. DOI: 10.1364/OL.478446.

[135] J. Zou, Y. Yu, M. Ye, L. Liu, S. Deng, X. Xu, and X. Zhang, "Short and efficient mode-size converter designed by segmented-stepwise method," *Opt. Lett.*, vol. 39, no. 21, pp. 6273–6276, Nov. 2014. DOI: 10.1364/OL.39.006273.

[136] L. Cheng, S. Mao, Z. Chen, Y. Wang, C. Zhao, and H. Y. Fu, "Ultra-compact dual-mode mode-size converter for silicon photonic few-mode fiber interfaces," *Opt. Express*, vol. 29, no. 21, pp. 33 728–33 740, Oct. 2021. DOI: 10.1364/OE.438839.

[137] W. Ma, M. Hou, R. Luo, B. Xiong, N. Liu, G. Liu, and T. Chu, "Topologically-optimized on-chip metamaterials for ultra-short-range light focusing and mode-size conversion," *Nanophotonics*, vol. 12, no. 6, pp. 1189–1197, 2023. DOI: 10.1515/nanoph-2023-0036.

[138] C.-L. Chen, *Foundation for guided-wave optics*. Wiley, 2007.

[139] Y. Satomura, M. Matsuhara, and N. Kumagai, "Analysis of electromagnetic-wave modes in anisotropic slab waveguide," *IEEE Transactions on Microwave Theory and Techniques*, vol. 22, no. 2, pp. 86–92, 1974. DOI: 10.1109/TMTT.1974.1128177.

[140] N. Hansen, *The cma evolution strategy: A tutorial*, 2023. DOI: 10.48550/arXiv.1604.00772. eprint: 1604.00772.

[141] SCBI–UMA. "Supercomputing and bioinnovation center." (2024), [Online]. Available: https://www.scbi.uma.es/site/scbi.

[142] M. A. Jette and T. Wickberg, "Architecture of the slurm workload manager," in *Job Scheduling Strategies for Parallel Processing*, D. Klusáček, J. Corbalán, and G. P. Rodrigo, Eds., Cham: Springer Nature Switzerland, 2023, pp. 3–23, ISBN: 978-3-031-43943-8.

[143] J. Rapin and O. Teytaud, *Nevergrad - A gradient-free optimization platform*, https://GitHub.com/FacebookResearch/Nevergrad, 2018.

[144] R. Halir, Í. Molina-Fernández, J. Wangüemert-Pérez, A. Ortega-Moñux, J. de-Oliva-Rubio, and P. Cheben, "Characterization of integrated photonic devices with minimum phase technique," *Opt. Express*, vol. 17, no. 10, pp. 8349–8361, May 2009. DOI: 10.1364/OE.17.008349.

[145] D. Pereira-Martín, "Filtros bragg de respuesta espectral arbitraria para fotónica integrada de silicio," Ph.D. dissertation, Universidad de Málaga, 2022.

[146] C. Pérez-Armenta, A. Ortega-Moñux, J. M. Luque-González, R. Halir, P. Reyes-Iglesias, J. H. Schmid, P. Cheben, Í. Molina-Fernández, and J. G. Wangüemert-Pérez, "Polarization independent 2×2 multimode interference coupler with bricked subwavelength metamaterial," in *European Optical Society Annual Meeting (EOSAM 2022)*, Porto, Portugal, Dec. 2022.

[147] C. Pérez-Armenta, A. Ortega-Moñux, J. M. Luque-González, R. Halir, P. Reyes-Iglesias, J. H. Schmid, P. Cheben, Í. Molina-Fernández, and J. G. Wangüemert-Pérez, "Polarization-insensitive multimode interference coupler based on bricked subwavelength gratings," in *Photonics North 2022*, Niagara Falls, Canada, 24-26 May 2022.

[148] C. Pérez-Armenta, J. Čtyroký, P. Cheben, J. H. Schmid, A. Ortega-Moñux, R. Halir, Í. Molina-Fernández, and J. G. Wangüemert-Pérez, "A design methodology for resonant sensors based on subwavelength grating waveguides at 1.31 μm," in *OSA Optical Sensors and Sensing Congress*, Virtual Conference, Washington, DC, United States, 22-26 June 2020.

[149] C. Pérez-Armenta, A. Ortega-Moñux, J. M. Luque-González, R. Halir, J. Schmid, P. Cheben, I. Molina-Fernández, and J. G. Wangüemert-Pérez, "Demostración experimental de un acoplador de interferencia multimodal insensible a la polarización basado en un metamaterial sublongitud de onda," in *XIII Reunión Española de Optoelectrónica (OPTOEL 23)*, Sevilla, Spain, 14–16 June 2023.

[150] C. Pérez-Armenta, A. Ortega-Moñux, J. M. Luque-González, R. Halir, J. H. Schmid, P. Cheben, Í. Molina-Fernández, and J. G. Wangüemert-Pérez, "Dispositivos de interferencia multimodal 2×2 de banda ultraancha basados en estructuras periódicas sub-longitud de onda para las bandas o-e-s-c," in *XII Reunión Española de Optoelectrónica (OPTOEL 2021)*, Virtual Conference, Spain, 30 June - 2 July 2021.

[151] C. Pérez-Armenta, J. Čtyroký, A. Ortega-Moñux, P. Cheben, J. H. Schmid, R. Halir, Í. Molina-Fernández, and J. G. Wangüemert-Pérez, "Design of an ultra-narrowband subwavelength grating-based bragg filter for silicon photonics sensing in o-band," in *XXXV Simposio Nacional de la Unión Científica Internacional de Radio (URSI)*, Virtual Conference, Málaga, Spain, Feb. 2020.

[152] C. Pérez-Armenta, Í. Molina-Fernández, P. Cheben, J. Čtyroký, and J. G. Wangüemert-Pérez, "Ultra-narrowband subwavelength based bragg filter for silicon photonics biosensing," in *XXXIV Simposio Nacional de la Unión Científica Internacional de Radio (URSI)*, Sevilla, Spain, Apr. 2019.

[153] J. M. Luque-González, C. Pérez-Armenta, M. Barona-Ruiz, A. Fernández-Hinestrosa, J. G. Wangüemert-Pérez, J. Schmid, P. Cheben, R. Halir, Í. Molina-Fernández, and A. Ortega-Moñux, "Towards polarization-agnostic silicon photonic devices through swg metamaterial engineering," in *Photonics North*, Montreal, Canadá, Dec. 2023.

[154] J. G. Wangüemert-Pérez, C. Pérez-Armenta, P. Ginel-Moreno, J. M. Luque-González, A. H.-E. Houati, A. Sánchez-Postigo, J. de Oliva Rubio, A. Ortega-Moñux, R. Halir, J. H. Schmid, P. Cheben, and Í. Molina-Fernández, "Recent progress in subwavelength grating metamaterial engineered silicon photonic devices," in *Proc. SPIE PC12575, Integrated Optics: Design, Devices, Systems and Applications VII*, 31 May 2023, PC125750A.

[155] J. G. Wangüemert-Pérez, C. Pérez-Armenta, P. Ginel-Moreno, J. M. Luque-González, A. Hadij-ElHouati, A. Sánchez-Postigo, J. de-Oliva-Rubio, A. Ortega-Moñux, R. Halir, J. H. Schmid, P. Cheben, and Í. Molina-Fernández, "Bricked and evanescently-coupled topologies: Expanding the portfolio of subwavelength metamaterial silicon photonic devices," in *SPIE Photonics West*, San Francisco, USA, 28 Jan–02 Feb 2023.

[156] J. G. Wangüemert-Pérez, J. M. Luque-González, C. Pérez-Armenta, R. Halir, J. H. Schmid, M. Dado, J. Litvik, P. Cheben, I. Molina-Fernández, and A. Ortega-Moñux, "Bricked patterning: A new concept to enhance the capabilities of subwavelength grating waveguides," in *IEEE Group IV Photonics Conference*, Virtual Conference, Málaga, Spain, Jul. 2021.